THE UNIVERSITY OF QUEENSLAND

AUSTRALIA

The CVD growth and the characterization of $Mo_xW_{1-x}Te_2$

Shijian Liu

Bachelor of Engineering

A thesis submitted for the degree of Master of Philosophy at

The University of Queensland in 2018

School of Mechanical and Mining Engineering

Abstract

In today's modern information era, with the fast developing of the electronic devices, the operation speed and the information spreading speed of the electronic devices are faster and faster, while the size of the electron components is smaller and smaller. An ineluctable problem is that the heat emission of the electron components is increasing with the smaller size, which has shown up and hinders the development of the electronic devices. Recently, a newly proposed material, the Topological Weyl semimetal, is expected to realize no-consumption electronic transportation due to the specific topological structure, which may solve the heat emission problem in the electronic devices in the future.

So far, the transition metal dichalcogenides (TMDs) $MoTe_2$ and WTe_2 have been predicted and proved to be the candidate of topological Weyl semimetals due to the strong topological structure and high feasibility in the synthesis. Furthermore, the alloying $Mo_xW_{1-x}Te_2$ is reported to combine the advantages of both $MoTe_2$ and WTe_2, which makes it a better candidate than binary system. So far, the nanostructure engineering is rather absent in $Mo_xW_{1-x}Te_2$. To apply $Mo_xW_{1-x}Te_2$ in the practical electronic devices, the study of the nanoengineering is in an emergency. Chemical vapour deposition (CVD) is a large-scale nanostructure growth method. Therefore, in this thesis, the growth of ternary $Mo_xW_{1-x}Te_2$ nanomaterials with a fast and simple CVD method is explored. The aiming is realized in the following steps:

- Realizing the CVD growth of the binary $MoTe_2$ nanomaterials. The CVD growth of binary $MoTe_2$ and WTe_2 nanomaterials has been studied widely. Here, we grew $MoTe_2$ nanostructures with a facile and catalyst-free CVD process. The morphology of $MoTe_2$ was found to be both rectangular and hexagonal, which is consistent with its 1T' polytype and 2H polytype, respectively. The thermal stability of $MoTe_2$ was found to be low, as the concentration of Te was found to be lower than Mo after annealing at 350 ^oC.
- Realizing the alloying of Mo, W and Te into ternary $Mo_xW_{1-x}Te_2$ nanomaterials. Based on the facile and catalyst-free CVD growth of $MoTe_2$ nanomaterials, the W precursors was added into the process. The W was found to alloy with Mo and Te successfully under certain condition, which will be described in detail in Chapter 3 and 4. The morphology of $Mo_xW_{1-x}Te_2$ nanomaterials were in rectangular belt, similar with the

morphology of 1T'-$MoTe_2$. The growth direction was found to be [100] and the surface facet was {002}. The chemical composition was determined to be $Mo_{0.9}W_{0.1}Te_2$.

- Understanding the growth mechanism. By tunning the experimental parameters, including the types of the precursors, the carrier gas, the growth time and growth temperature, the understanding of the growth was went deep. The growth mechanism was proposed to be vapour-solid (VS) mechanism after analysis. This work opens a new window to synthesize the nano-size $Mo_xW_{1-x}Te_2$ and provides the opportunity to study the nanostructure engineering of $Mo_xW_{1-x}Te_2$. Furthermore, this work pave the way for future nanostructure study of other ternary system in TMDs.

This thesis is written in five parts, including the induction (Chapter 1), literature review (Chapter 2), methodology (Chapter 3), results and discussions (Chapter 4), and conclusion (Chapter 5). Literature review mainly focuses on the research status and the choke points of MTe_2 (M=Mo, W). Besides, the crystal structures, intriguing properties and reported growth methods of $MoTe_2$ and WTe_2 have been summarized in this chapter. The methodology part is my own designed research plan based on the literature review including the synthesis method and characterization methods. Based on the experimental results, the morphology, structure, composition and growth mechanism of the CVD-grown $Mo_xW_{1-x}Te_2$ nanomaterials as well as the impact of the growth parameters are discussed in Chapter 4. Chapter 5 summarizes this thesis and gives the research direction in the future.

Declaration by author

This thesis is composed of my original work, and contains no material previously published or written by another person except where due reference has been made in the text. I have clearly stated the contribution by others to jointly-authored works that I have included in my thesis.

I have clearly stated the contribution of others to my thesis as a whole, including statistical assistance, survey design, data analysis, significant technical procedures, professional editorial advice, financial support and any other original research work used or reported in my thesis. The content of my thesis is the result of work I have carried out since the commencement of my higher degree by research candidature and does not include a substantial part of work that has been submitted to qualify for the award of any other degree or diploma in any university or other tertiary institution. I have clearly stated which parts of my thesis, if any, have been submitted to qualify for another award.

I acknowledge that an electronic copy of my thesis must be lodged with the University Library and, subject to the policy and procedures of The University of Queensland, the thesis be made available for research and study in accordance with the Copyright Act 1968 unless a period of embargo has been approved by the Dean of the Graduate School.

I acknowledge that copyright of all material contained in my thesis resides with the copyright holder(s) of that material. Where appropriate I have obtained copyright permission from the copyright holder to reproduce material in this thesis and have sought permission from co-authors for any jointly authored works included in the thesis.

Publications during candidature

“No publications”

Contributions by others to the thesis

Prof. Jin Zou and Associated Prof. Zhigang Chen have contributed to propose the research direction and thesis revision.

Dr. Yichao Zou has contributed to the instruction of the experimental operation.

Dr. Yichao Zou, Mr. Xiaolei Shi, Mr. Weidi Liu, Miss Yuzhe Yang, Mr. Qizhen Li and Mr. Guofang Liang have contributed to the SEM and TEM characterization.

Statement of parts of the thesis submitted to qualify for the award of another degree

“None”

Research Involving Human or Animal Subjects

“No animal or human subjects were involved in this research”

Acknowledgements

At first, I would like to express my genuine gratitude to my research supervisors, Prof. Jin Zou and Associated Prof. Zhigang Chen for their encouragement, guidance and patience in every respect of my MPhil research.

Also, I would like to thank my workmates in the group, Dr. Yichao Zou, Mr. Xiaolei Shi, Mr. Qizhen Li, Mr. Weidi Liu, Dr. Min Hong, Dr. Chen Zhou, Dr. Lei Yang, Dr. Mun Teng (Abby) Soo, Miss. Yuzhe Yang, Mr. Qiang Sun, Mr. Han Gao, Mr. Yuan Wang, Mr. Youichirou Kawami, Mr. Junjie Li, Mr. Liqing Huang, Mr. Raza Moshwan, Mr. Ting Liu, Mr. Shengduo Xu and Mr. Van Nguyen. Thank you very much for your great help and support in my research and life in Brisbane.

Meanwhile, I gratefully thank the Centre for Microscopy and Microanalysis (CMM) at UQ, which provided a great opportunity to do my research. Besides, I would like to thank Dr. Hui Diao who helped me to do the focused ion beam (FIB), and Mrs Ying Yu who helped me to do the Raman characterization.

Finally, I would like to give my great thanks to my parents and my wife in China, who always give me strength and endless careness when I felt upset and loss. It's them who give me the motivation to move forward in my research and life.

Financial support

I would like to thank my parents, from my bottom of my heart, for the financial support which gives me an opportunity to study in UQ.

Keywords

CVD, $MoTe_2$, WTe_2, $Mo_xW_{1-x}Te_2$, nanostructure, XRD, Raman, SEM, TEM

Australian and New Zealand Standard Research Classifications (ANZSRC)

ANZSRC code: 100712, Nanoscale Characterization, 40%

ANZSRC code: 100716, Nanofabrication, Growth and Self-Assembly 40%

ANZSRC code: 091203, Compound Semiconductors, 20%

Fields of Research (FoR) Classification

FoR code: 0912, Materials Engineering, 50%

FoR code: 1007, Nanotechnology, 50%

Table of Contents

List of Figures

Figure 4.18 (a) and (b) are the over-view and high-magnification SEM image of the $Mo_xW_{1-x}Te_2$ nanobelts grown in 60 min.

Figure 4.19 (a) and (b) are the over-view and high-magnification SEM image of the $Mo_xW_{1-x}Te_2$ nanobelts grown in 10 min.

List of Tables

List of Abbreviations used in the thesis

TWS	topological Weyl semimetal
TMDs	transition metal dichalcogenides
CVD	chemical vapour deposition
CVT	chemical vapour transportation
XRD	X-ray diffraction
SEM	scanning electron microscopy
TEM	transmission electron microscopy
HRTEM	high-resolution transmission electron microscopy
EDS	energy dispersion X-ray spectroscopy
SAED	selected area electron diffraction
BF	bright field
ARPES	angle resolved photoemission spectroscopy
VS	vapour-solid growth
VSL	vapour-solid-liquid growth
MR	magnetoresistance
NMR	negative magnetoresistance
WAL	weak antilocalization effect
T	temperature
AHM	ammonium heptamolybdate

Chapter 1
Introduction

1.1 Background

With the first-time discovery of TaAs to be a Topological Weyl Semimetal (TWS) in 2015, more and more researchers have involved in this new area because of its great potential applications in the next generation of transportation devices and superconductors, or even topological quantum computers in the future. There are three main characteristics for TWS: magnetic 'monopole', Fermi arc and chiral anomaly.

- First is the magnetic 'monopole'. When mentioning about topological materials, topological invariant is essential as different topological number refer to different topological phase. Topological invariant is defined as: $\int_S \Omega(k) \cdot dS = 2\pi Z$, where Ω(k) is the Berry curvature and S is the closed curved surface. For three-dimensional metal, the S is the Fermi surface. When Z=0, it is trivial normal metal. When $Z \neq 0$, it is nontrivial topological metal. In fact, the Berry curvature can be expressed as a notation of a vector, which can be viewed as a magnetic field in *k* space (this is related to some theoretical physics and mathematics, which will not be interpreted here). Furthermore, according to the Gauss theorem, for a closed surface, the integral of a magnetic flux is zero as the divergence of magnetic field is zero. Therefore, in a topological metal, the $Z \neq 0$, which means the divergence of magnetic field, is not zero. Moreover, these facts indicate that its behaviour is similar to the magnetic 'monopole'. With these magnetic 'monopoles', the Weyl semimetal is expected to have anomalous Hall effect and even makes the quantum anomalous Hall effect or quantum spin Hall effect come true.
- Second is the Fermi arc. For topological materials, the most interesting part is the surface state because topology is meaningless if the material system is infinite. For example, for topological insulator, the conduction band and the valence band are connected so that the surface state of topological insulator can be conductive. Moreover, this is why the topological insulator attracts peoples' eyes. As for topological semimetal, it also has a unique surface state, which is called the Fermi arc. In fact, the Fermi arc is a kind of Fermi surface. Differing from the traditional

concept that the Fermi surface is a connected curve, the Fermi surface in a single particle of topological Weyl semimetal is an open line, called Fermi arc. It actually can be viewed as that a closed Fermi surface is cut by the Weyl nodes in the bulk so that one Fermi arc is at the upper surface and the other one is at the lower surface. So for the electrons cyclotron resonance, electrons will move through the bulk and across the Weyl node from upper surface to the lower surface and then across another Weyl node back to the upper surface. Therefore, under this circumstance the frequency of the cyclotron resonance is not only related to the Fermi surface but also related to the thickness of the material. The Fermi arc is usually used as the hallmark of TWS that to prove whether a material is TWS or not, use the Angle Resolved Photoemission Spectroscopy (ARPES) to obtain its electronic structure to find out whether there is the Fermi arc or not.

- Third is the chiral anomaly. According to the “no-go” theorem, in a Weyl semimetal the Weyl points always appear in pairs with opposite chirality.[1] Therefore, chiral anomaly is to break the conservation of the two Weyl fermions with opposite chirality and transform one Weyl fermion to the other one with opposite chirality with the total number conservation. Under intense magnetic field, there will be a difference of chemical potential between the two neighbouring Weyl nodes with opposite chirality. This will lead to the transportation of electrons between two Weyl nodes where an extra current is arisen. This is the reason to explain the negative magnetoresistance of TWS that the resistivity is decreasing with the increasing magnetic field in the measurement. Therefore, the superconductivity may be arisen due to the high magnetic field instead of extremely low temperature, which may be a pathway to promote the practical application of superconductivity.

During the past two years, the family of TWSs has been expanded constantly in which the transition metal dichalcogenides (TMDs) $MoTe_2$ and WTe_2 are the most popular. Because they are the best candidates to realize the application of TWS, which not only has a layered structure greatly facilitating the fabrication of devices but also has a relatively stable topological structure that is beneficial for the experimental study. However, the disadvantages of $MoTe_2$ and WTe_2 are obvious, which will restrict their further development and application. For $MoTe_2$, the most disadvantage is the semimetallic phase is unstable at room temperature, which will definitely lower its practicability. As for WTe_2, although the semimetallic phase is stable at room temperature without the other phase transition, it is less topologically stable than $MoTe_2$,[2,3] which means its topological properties are not as

good as $MoTe_2$. Besides, the reactivity of W is relatively low which makes pure WTe_2 difficult to synthesize. In order to overcome the shortcomings of $MoTe_2$ and WTe_2, it is reported in 2017 that doping W into $MoTe_2$ by chemical vapour transport (CVT) leads a phase transition to semimetallic phase and thus stabilizes the semimetallic phase under room temperature.[4] This new findings have combined the advantages of both $MoTe_2$ and WTe_2 and opened a new window for researchers to study these two materials. However, the synthesis process is rather complex as they first used solid state reaction to synthesize the polycrystalline $Mo_xW_{1-x}Te_2$ for one day and then used CVT to grow single crystalline $Mo_xW_{1-x}Te_2$ for one week. Therefore, developing a fast and convenient but also productive synthesis method is in an emergency.

Chemical vapour deposition (CVD) is a commonly used method for the synthesis of semiconductor nanomaterials. Extensive studies have shown that the binary $MoTe_2$ and WTe_2 nanomaterials can be synthesized via CVD with a simple and fast synthesis process.[5-18] In general, two kinds of CVD methods, including two-step CVD and one-step CVD, are used. For the two-step CVD, Mo (W) precursor is deposited onto the substrate prior to the growth.[5-16] Te precursor further reacts with Mo (W) precursor on the substrate after evaporation, transportation, and deposition. For one-step CVD, Mo (W) and Te precursors are both evaporated during the heating, transported by carrier gas, deposited on the substrate, and reacting with each other finally.[17,18] Both two-step and one-step CVD are of short growth time down to 5 min.[7,9] Therefore, the objectives of this MPhil thesis is to synthesize $Mo_xW_{1-x}Te_2$ nanomaterials with a fast and simple CVD process.

1.2 Objectives

The objective of the thesis is to grow $Mo_xW_{1-x}Te_2$ nanomaterials using CVD method and to understand their growth mechanism through detailed structural and compositional characterization. The specific objectives are as follows:

1. The preliminary study on the synthesis of binary $MoTe_2$ and WTe_2 first and understanding their morphology, structural and compositional characteristics;
2. Growth of high-quality $Mo_xW_{1-x}Te_2$ nanomaterials using CVD method and understanding the relationship between the growth parameters and the morphology, structural and compositional characteristics of the $Mo_xW_{1-x}Te_2$ nanomaterials.

3. Understanding the growth mechanism by observing the morphology and structural characterizations.

1.3 Thesis outline

In this thesis, $Mo_xW_{1-x}Te_2$ nanostructures were synthesized by CVD method. The morphology, structural and compositional characterizations of the as-synthesized nanostructures are studied by XRD, Raman spectroscopy, SEM and TEM. The outline of the thesis are listed below:

Chapter 1 gives a comprehensive introduction of this MPhil thesis, including the background and the objectives.

Chapter 2 is the literature review showing the current research status of the $MoTe_2$, WTe_2 and $Mo_xW_{1-x}Te_2$, including their crystal structure, physical properties and growth methods.

Chapter 3 is the methodology showing the synthesis methods and characterization methods conducted in this thesis.

Chapter 4 is our observations and analysis in the $Mo_xW_{1-x}Te_2$ nanomaterials synthesized by CVD method. It mainly discusses about the growth of $Mo_xW_{1-x}Te_2$ nanomaterials and revealing the morphology, structure, composition, growth direction and growth mechanism. Besides, the impact of the H_2 atmosphere, growth time and the source material in CVD process are also discussed.

Chapter 5 gives a summary of this MPhil research work and the research direction in the future.

Chapter 2
Literature Review

2.1 Structure characterization

To understand this ternary system $Mo_xW_{1-x}Te_2$, the basic structure of $MoTe_2$ and WTe_2 should be understood first. In general, TMDs can crystallize into two common phases, trigonal prism (2H polytype) and octahedral (1T polytype).[19-22] $MoTe_2$ and WTe_2 are two exceptions. For $MoTe_2$, 2H phase is still stable while 1T phase is unstable. Instead, it will crystallize into a distorted octahedral phase, which is named as 1T'. As for WTe_2, its stable phase at room temperature is orthorhombic T_d phase, which is also existed in $MoTe_2$ when temperature goes below ~ 240 K. In common, both $MoTe_2$ and WTe_2 have the typical layered structure with the "…A-B-A-B…" stacking sequence. Each layer includes three sub-layered atoms, where the upper and lower sub-layer are the Te atoms while the middle sub-layer is the Mo or W atoms. Each Mo atom is connected with six Te atoms while each Te atom is connected with three Mo atoms. The neighbouring two layers are connected by Van der Waal bonds.

2.1.1 $MoTe_2$

For $MoTe_2$, it can normally crystallize into hexagonal (2H/α), monoclinic (1T'/β) and orthorhombic (T_d/γ) phase (Table 2.1). The phase-transition temperature of 2H and 1T' is at about ~ 880 ^oC as shown in Figure 2.1. For the T_d-$MoTe_2$, as it is a newly found phase during the search of topological materials, it has not been shown in the Mo-Te phase diagram. The T_d-$MoTe_2$ is actually transited from 1T'-$MoTe_2$ at ~ 240 K, which has been verified recently.

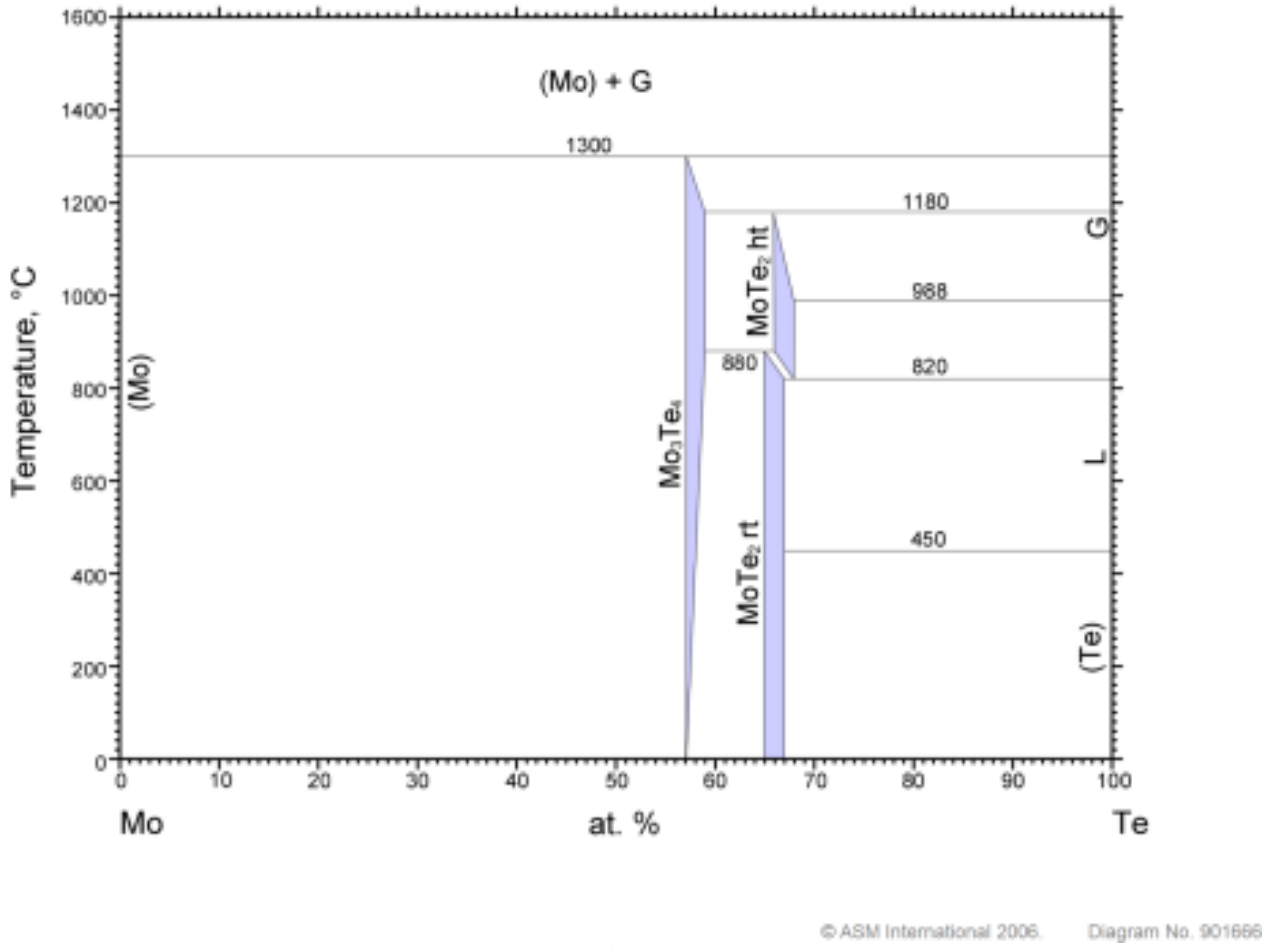

Figure 2.1 Binary phase diagram of Mo-Te.[23]

2.1.1.1 2H-$MoTe_2$

Same as all the 2H phase of TMDs, 2H-$MoTe_2$ is semiconducting with ~ 0.9 eV indirect band gap and stable at room temperature. It is a hexagonal phase(Space group, *$P6_3/mmc$*) with the lattice parameters of *a*=3.519 Å and *c*=13.964 Å (Table 2.1).[24,25] Its standard XRD can be referred to No.72-0117. As for Raman spectrum, the characteristic peak of 2H-$MoTe_2$ is at E^1_{2g}=230-235 cm^{-1} while other common peaks are at E_{1g}=116c-119 m^{-1}, A_{1g}=170-174 cm^{-1} and B^1_{2g}=288c-291 m^{-1} (Figure 2.2).[4,10,15,17,26-29] Besides, for the bulk and monolayer thin film of 2H phase, an additional peak B^1_{2g} at ~289 cm^{-1} will be shown up.[10,15,26,28,29] In CVD synthesis, 2H phase can form into thin films (Figure 2.3 (a) and 2.3 (b)) or flakes with triangle shape (Figure 2.3 (c)). The typical SAED pattern shows a hexagonal shape along [001] zone axis (Figure 2.3 (d)).

2.1.1.2 1T'-$MoTe_2$

Similar with octahedral 1T phase of other TMDs, the distorted octahedral 1T'-$MoTe_2$ is metallic and stable at high temperature (above 880 ^oC).[20] It is a monoclinic phase (Space group, $P2_1/m$) with the lattice parameters of a=6.330 Å, b=3.469 Å, c=13.86 Å and β=93^{o}55' (Table 2.1).[25] Its standard XRD pattern can be referred to No.71-2157. As for the Raman spectrum, the characteristic peak of 1T'-$MoTe_2$ is at B_g= 160-163 cm^{-1} while other common peaks are at A_u=107-112 cm^{-1}, A_g=126-128 cm^{-1} and A_g=256-258 cm^{-1} (Figure 2.2).[4,5,10,11,15,17,18,26-32] In addition, the A_g peak at ~ 258 cm^{-1} is expected to blue-shift to 269 cm^{-1} when the material is reducing from bulk to monolayer.[11] Therefore, the peak at 269 cm^{-1} could be regarded as a symbol of monolayer 1T'-$MoTe_2$. In CVD synthesis, 1T' phase can also form into thin films (Figure 2.3 (e) and 2.3 (f)) or flakes (Figure 2.3 (g)) but with different contrast or shape compared with 2H phase. The typical SAED pattern shows a rectangular shape (Figure 2.3 (h)).

2.1.1.3 T_d-$MoTe_2$

As for the T_d-$MoTe_2$, it is a Topological Weyl semimetal stable at low temperature (~ 240 K).[33] It is an orthorhombic phase (Space group, $Pmn2_1$) with the lattice parameters of a=6.33 Å, b=3.469 Å, c=13.83 Å. Since it is arisen from the slight sliding of the monoclinic lattice of 1T' phase, the lattice parameters are quite similar.[2] Distinct from the Raman spectrum of 1T'-$MoTe_2$, the appearance of the peak at ~ 12.6 $cm^{-1}$for θ=45 ^{o} or ~ 29.1 cm^{-1} for θ=0 ^{o} is the symbol of T_d-$MoTe_2$, as shown in Figure 2.2 (f) (θ is the angle between the polarization of the incident laser and the crystal a-axis).[32,34,35] As T_d-$MoTe_2$ is not stable under room temperature, the XRD pattern, the SEM and the TEM results of T_d-$MoTe_2$ is still absent up to now. Instead, the angle resolved photoemission spectroscopy (ARPES) is used to obtain its low-temperature electronic structure, the unique structure Fermi arc and Weyl node, which can be regarded as the evidences of the appearance of T_d-$MoTe_2$.[30,36,37]

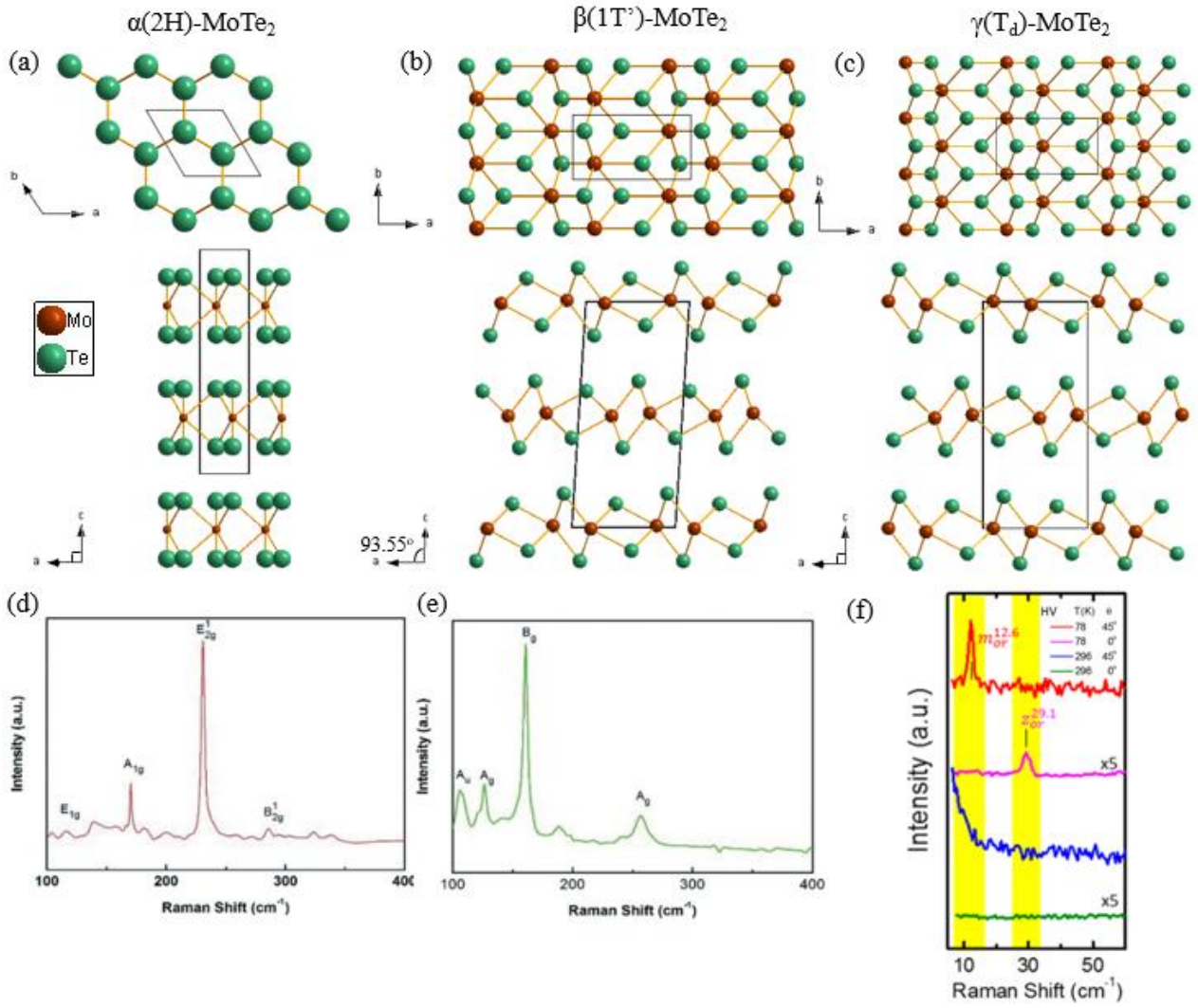

Figure 2.2 (a)-(c) Top-view and side-view crystal structures of 2H-, 1T'- and T_d-$MoTe_2$, respectively. (d)-(f) Typical Raman spectra of 2H-, 1T'- and T_d-$MoTe_2$ respectively showing characteristic peaks of each phase.[27,29,32]

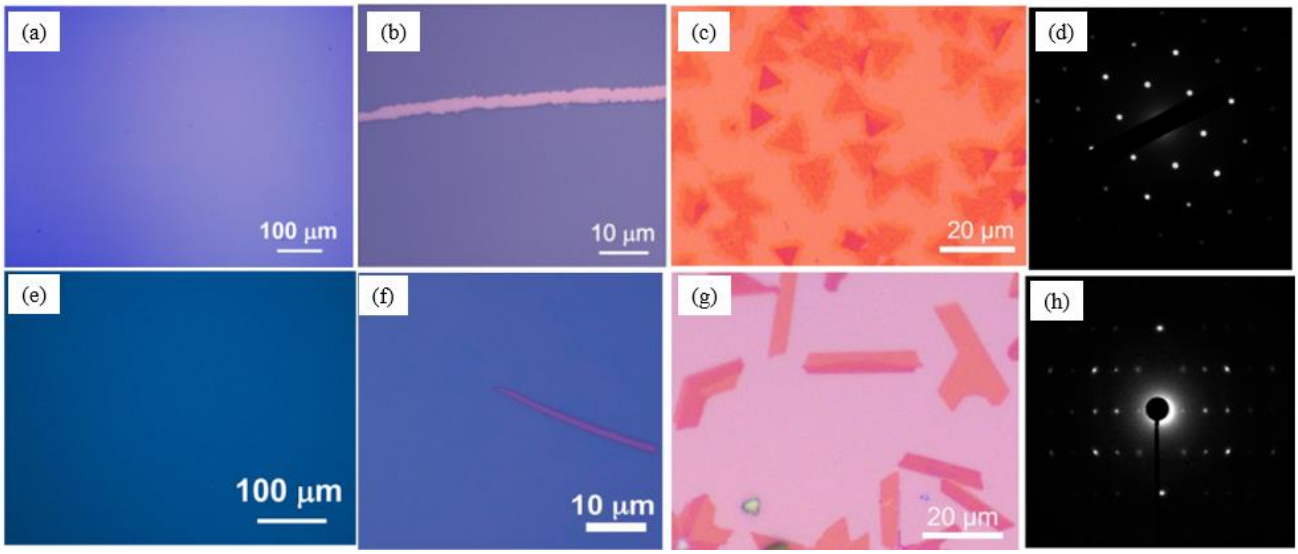

Figure 2.3 (a) and (b) Optical images of 2H-$MoTe_2$ thin films. The pink area is the scratch line showing the 300 nm SiO_2/Si substrate. (c) Tptical image of 2H-$MoTe_2$ flakes with triangle shape. (d) SAED pattern of 2H-$MoTe_2$ showing a hexagonal reciprocal lattice. (e) and (f) Optical image of 1T'-$MoTe_2$ thin films. The pink area is the scratch line showing the 300nm SiO_2/Si substrate. (g) Optical image of 1T'-$MoTe_2$ flakes with triangle shape. (h) SAED pattern of 1T'-$MoTe_2$ showing a hexagonal rectangular lattice. [10,27,31]

2.1.2 WTe_2

2.1.2.1 T_d-WTe_2

Unlike all the other TMDs, WTe_2 has no 2H or 1T phase at room temperature but only orthorhombic T_d phase (Figure 2.4 (b)). Similar with T_d-$MoTe_2$, the T_d-WTe_2 is another newly found Topological Weyl semimetal. The space group is *Pnm2₁* with the lattice parameters of *a*=6.282 Å, *b*=3.496 Å, *c*=14.07 Å (Table 2.1).[38] The standard XRD pattern can be referred to No.72-2156. As for the Raman spectrum, the characteristic peaks of T_d-WTe_2 are at A^5_1=162-165 cm^{-1} and A^2_1=205-212 cm^{-1} while the other peaks are at A^6_1=139.1 cm^{-1}, A^8_1=130-136 cm^{-1}, A^9_1=118-119 cm^{-1} and A^4_2=109-112 cm^{-1}.[4,6,16,18,39-44] Besides, it is concluded that with the decreasing layers, the A^8_1 and A^2_1 peaks will blue-shift while the A^4_2 and A^5_1 peaks will red-shift (Figure 2.4 (c)).[43] What's more, A^4_2 peak will disappear in monolayer.[43] In CVD synthesis, the T_d-WTe_2 can also form into uniform thin films (Figure 2.5 (b)) and flakes with rectangular or star-like shape (Figure 2.5 (a)). The SAED pattern of T_d-WTe_2 shows a rectangular reciprocal lattice (Figure 2.5 (c)).

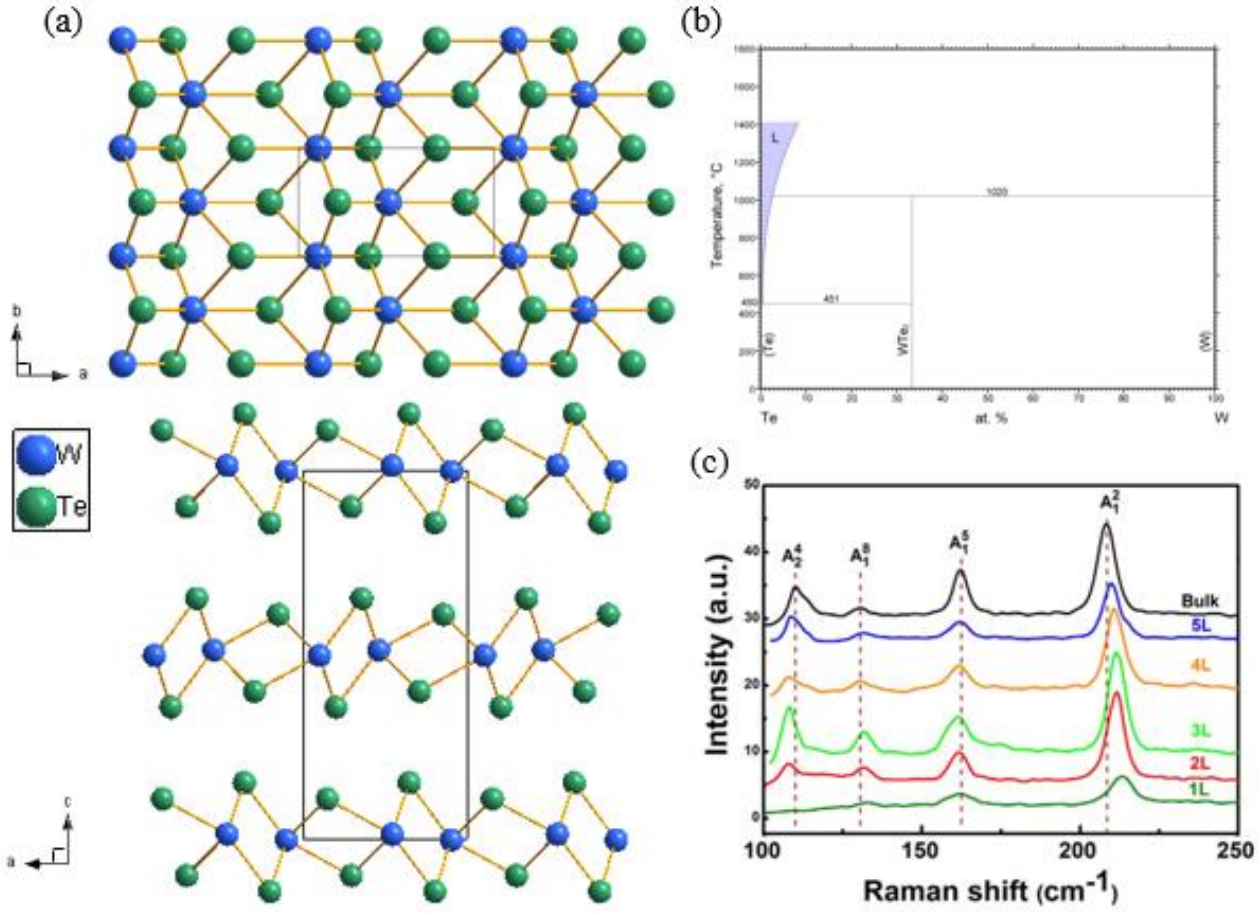

Figure 2.4 (a)-(c) Top-view and side-view crystal structures, binary phase diagram, typical Raman spectrum of T_d-WTe_2, respectively.[3,43,45]

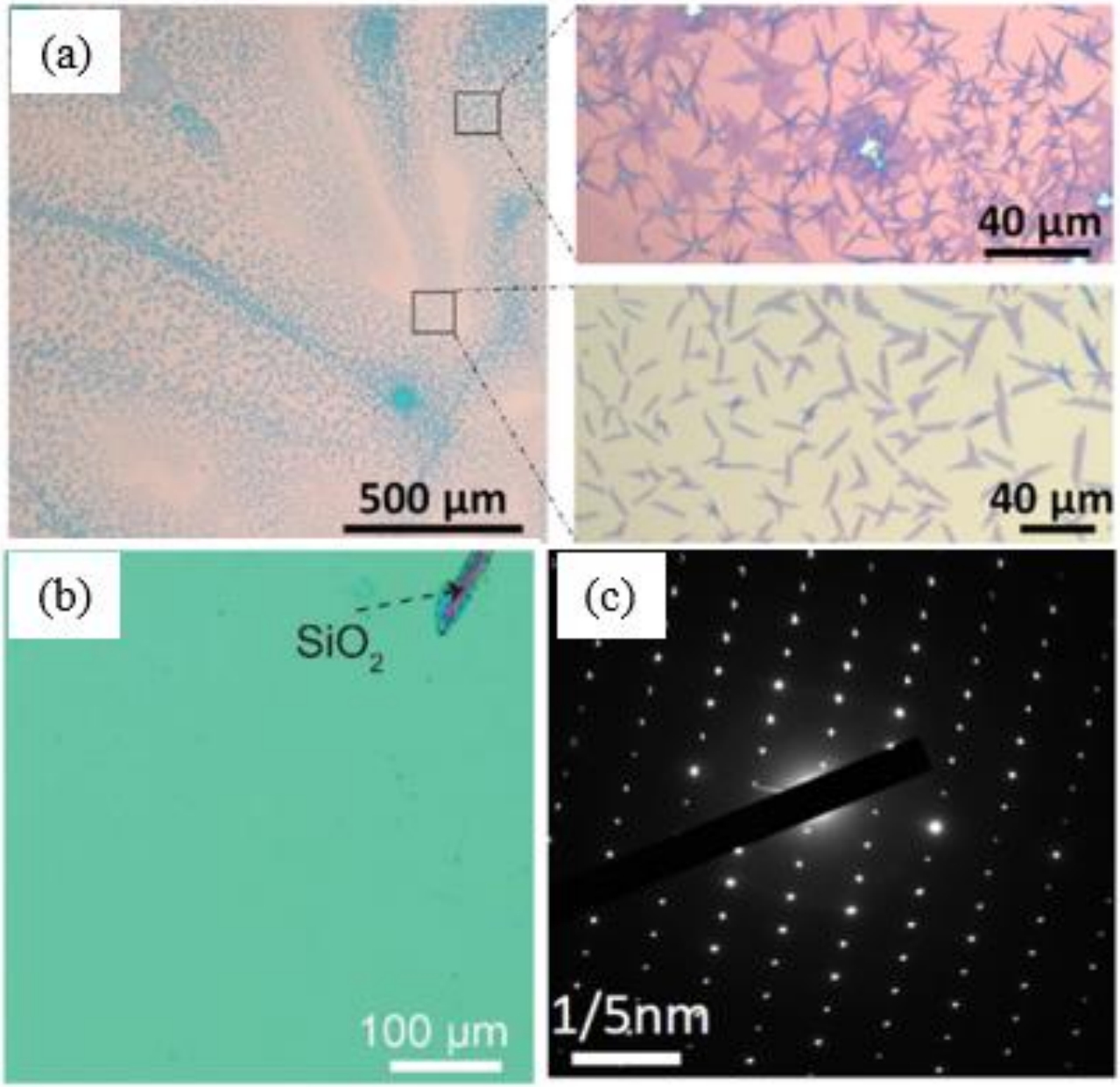

Figure 2.5 (a) Optical image of T_d-WTe_2 flakes. (b) Optical image of T_d-WTe_2 thin films. The pink area is a scratch line showing the SiO_2/Si substrate. (c) Typical SAED pattern of T_d-WTe_2 showing a rectangular shape.[6,18,46]

Table 2.1 Summarization of the crystal structure information of α, β, γ phase.

Phase	Crystal Structure	Lattice Parameters	JCPDS	Ref.
2H-$MoTe_2$	Hexagonal, *$P6_3/mmc$*	*a*=3.519 Å , *c*=13.964 Å	No. 72-0117	[25]
1T'-$MoTe_2$	Monoclinic, *P21/m* (11)	*a*=6.330 Å, *b*=3.469 Å, *c*=13.86 Å, *β*=93°55'	No. 71-2157	[25]
T_d-$MoTe_2$	Orthorhombic, *Pmn21* (31)	*a*=6.33 Å, *b*=3.469 Å, *c*=13.83 Å	-	[25]
T_d-WTe_2 (higher temperature)	Orthorhombic, *Pnm21* (31)	*a*=6.282 Å, *b*=3.496 Å, *c*=14.07 Å	No. 71-2156	[38]
T_d-WTe_2 (113 K)	Orthorhombic, *Pnm21* (31)	*a*=3.477 Å, *b*=6.249 Å, *c*=14.018 Å	No. 81-1908	[3,47]

2.1.3 $Mo_xW_{1-x}Te_2$

$Mo_xW_{1-x}Te_2$ can be viewed as part of the Mo atoms are replaced by W atoms. For $Mo_xW_{1-x}Te_2$, the phase transition is just like the combination of $MoTe_2$ and WTe_2. The possible phase of $Mo_xW_{1-x}Te_2$ includes 2H-$MoTe_2$, 1T'-$MoTe_2$ and T_d-WTe_2 under room temperature. Furthermore, it has been widely reported that the phase transition in $Mo_xW_{1-x}Te_2$ is related to the content of W, which is mainly characterized by Raman spectroscopy. With increasing W content, the phase transition is from 2H-$MoTe_2$ to 1T'-$MoTe_2$ and to T_d-WTe_2 finally. However, there is still not a clear conclusion about the phase transition boundary yet. Different papers have different conclusions. In Yang-yang Lv's work, [48] it is reported that for $x \leq 0.09$, $Mo_xW_{1-x}Te_2$ is 2H phase while when $0.10 \leq x \leq 0.30$, $Mo_xW_{1-x}Te_2$ transfer to 1T' phase without mixed phase coexisting. Increasing the content of W to 0.85, $Mo_xW_{1-x}Te_2$ transit from 1T' to T_d phase (The 1T'+ T_d mixed phase shows up in x=0.5 and 0.7). Another work done by Yang-yang Lv's group,[49] the results are a little bit different. For x=0.15 and 0.32, they are identified as the 1T' and T_d mixed phase coexistence. While in D. Rhodes's work,[4] their results show that no 1T' phase existing in $Mo_xW_{1-x}Te_2$. When $0 \leq x \leq 0.08$, $Mo_xW_{1-x}Te_2$ is still 2H phase while from 0.09 to 1, $Mo_xW_{1-x}Te_2$ are all T_d phase. In Sean M Oliver's work, they found that when $x \leq 0.09$, $Mo_xW_{1-x}Te_2$ is 2H phase. From 0.12 to 0.47, 1T' and T_d phase are coexisting. Finally, 1T' phase transit to T_d phase at x=0.63. Furthermore, they also claim that quenching their samples (after the heating of the synthesis process) can cause different

results for x=0~0.09. For x=0~0.04, $Mo_xW_{1-x}Te_2$ change from 2H phase to 1T' phase by using quenching while both 1T' and Td phase exist in $Mo_{0.91}W_{0.09}Te_2$. Similar to the characteristic Raman peaks at A_{1g} (~ 173 cm^{-1}) and E_{2g} (~ 233 cm^{-1}) of 2H-$MoTe_2$, A_g (~ 260 cm^{-1}) of 1T'-$MoTe_2$ and A_1 (~ 210 cm^{-1}) of T_d-WTe_2, it is newly found that a peak at ~ 178 cm^{-1} could be uniquely belong to the $Mo_xW_{1-x}Te_2$ alloy, which is worthy to use for reference.[50]

Table 2.2 Summarization of the relationship between the content of W and the phase transition.

$Mo_xW_{1-x}Te_2$	2H	2H+ 1T'	1T'	1T'+ T_d	T_d	Ref
x=	0, 0.05, 0.06, 0.07, 0.08, 0.09	-	0.1, 0.15, 0.3	0.5, 0.7	0.85, 0.9, 0.95, 1	48
	0, 0.04	-	0.1	0.15, 0.32, 0.57, 0.70	0.88, 1	49
	0, 0.03, 0.06, 0.08	-	-	-	0.09, 0.1, 0.11, 0.12, 0.21, 0.23, 0.27, 1	4
	0, 0.01, 0.02, 0.04, 0.09	-	0, 0.01, 0.02, 0.04	0.09, 0.12, 0.29, 0.33, 0.47	0.63, 0.71, 1	50

2.2 Physical properties

2.2.1 Magnetoresistance

Magnetoresistance (MR) effect is the change of electronic resistance when the magnetic field changes. Nowadays, the size of the electronic storage device is smaller and smaller while the storage is larger and larger. This is due to the giant magnetoresistance effect. In $MoTe_2$, it is reported that the positive MR can reach 16000 % at 1.8 K in 14 T (Figure 2.6).[26] While in W-Te system, it is even reported that T_d-WTe_2 has a giant MR up to 452700 % at 4.5 K in 14.7 T (Figure 2.7 (a)) and even 13000000 % at 0.53 K in 60 T without any signs of saturation both at the direction of electronic current parallel to *a*-axis and magnetic field parallel to *c*-axis (Figure 2.7 (b)).[46] Such findings in $MoTe_2$ and WTe_2 may lead to a huge

improving in magnetic storage application. On the other hand, negative magnetoresistance (NMR), which is expected to have the potential to realize room-temperature superconductivity, is also found in T_d-WTe_2. When I//H//*a*, NMR reaches a maximum value of 30 % at 2 K in 9 T and disappears above 10 K (Figure 2.7 (c)).[46,51] Similarly, when I//H//*b* NMR reaches a maximum value of 40% at 2 K in 9 T and disappears at about 30 K (Figure 2.7 (d)).[46,51]

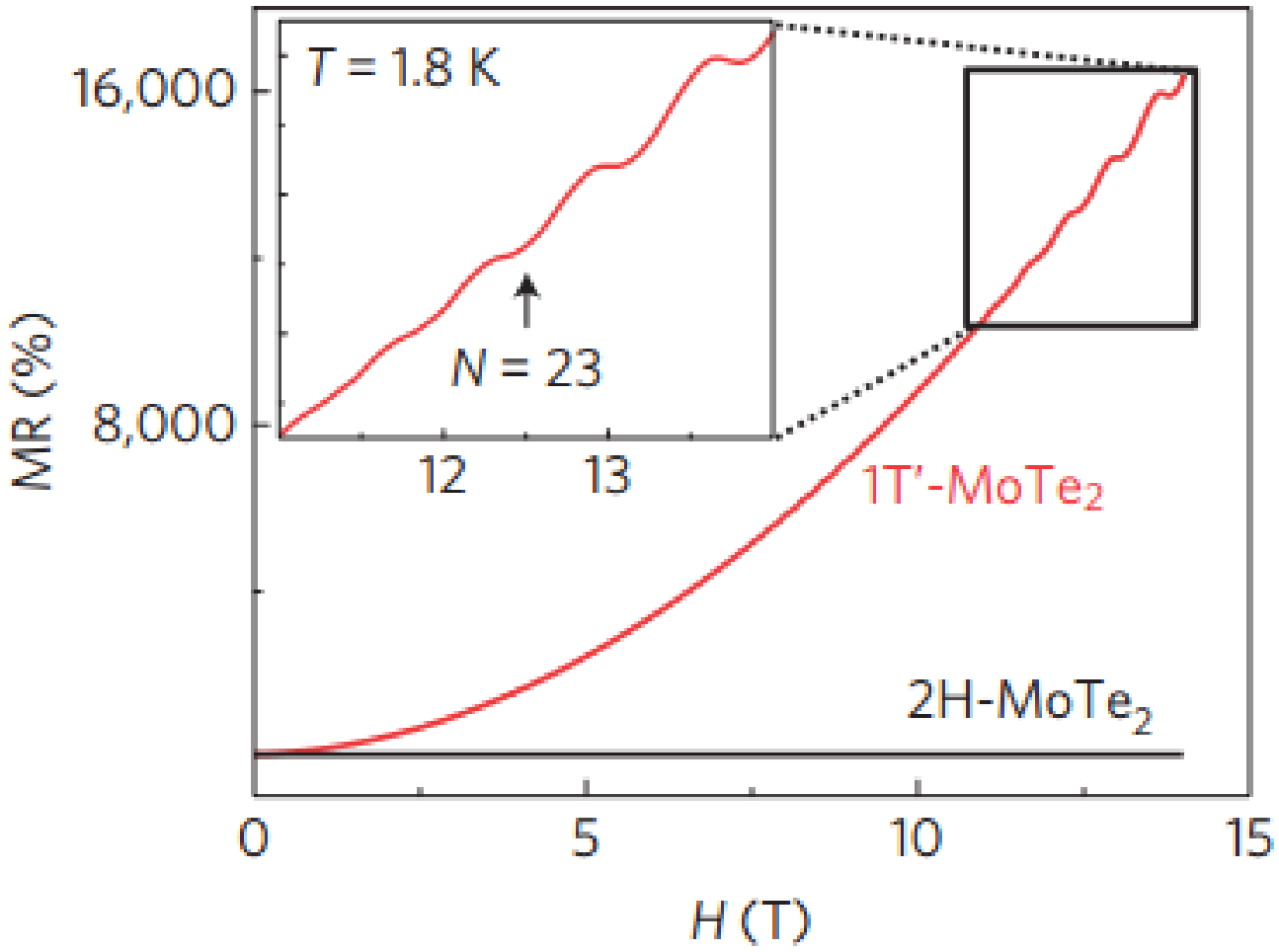

Figure 2.6 Magnetic field dependent MR of $MoTe_2$ at 1.8 K. The inset is the SdH oscollation.[26]

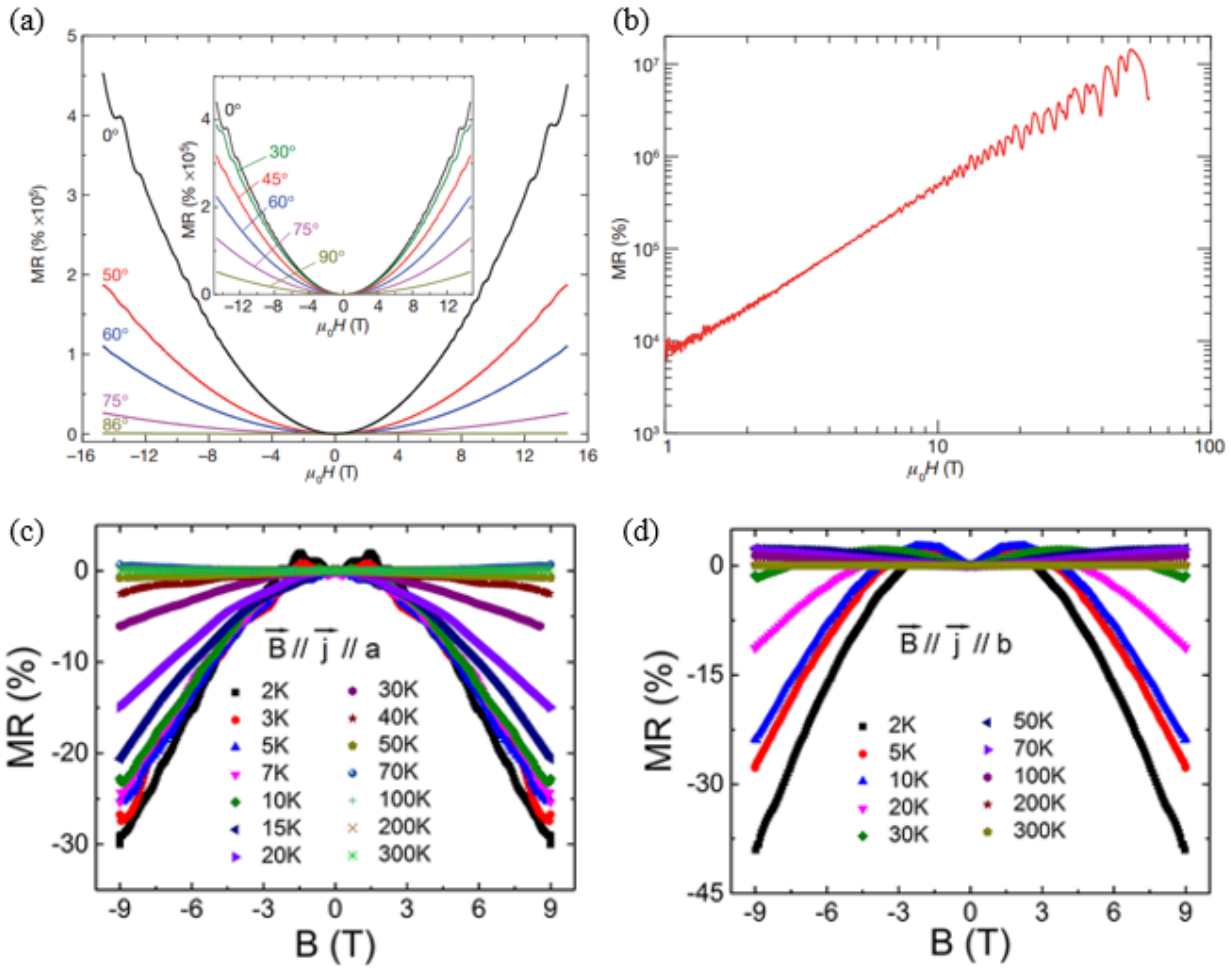

Figure 2.7 (a) Magnetic field dependent MR of T_d-WTe_2 under different angle at 2 K when I//*a* (The angle is between H and *c*-axis). Inset is the same with I//*b*. (b) Magnetic field dependent MR of T_d-WTe_2 at 0.53 K (I//*a*, H//*c*). (c) and (d) Magnetic field dependence MR under various temperature with the direction of J//B//*a* and J//B//*b*, respectively. I and J are the electronic current while H and B are the magnetic field.[46,51]

2.2.2 Superconductivity

Superconductivity is always a hot area in the study of electronic transportation as it may reduce the energy consumption during transportation. Recently, pressure-induced superconductivity was found in both 1T'-$MoTe_2$ and T_d-WTe_2.[52,53] Under ambient pressure, both 1T'-$MoTe_2$ and T_d-WTe_2 have metallic behaviour that the resistivity is reducing with the decreasing of temperature. For 1T'-$MoTe_2$, it is obvious to find that the resistivity can reach to zero when applying external pressure (Figure 2.8 (a) and 2.8 (b)). The maximum transition temperature (T_c) can reach 8.2 K at 11.7 GPa.[52] As for T_d-WTe_2, the resistivity cannot reach

to zero when external pressure is below 10.5 GPa. Beyond 10.5 GPa external pressure, the zero resistance shows up. The maximum T_c can reach 6.5 K at 13.0 GPa.[53]

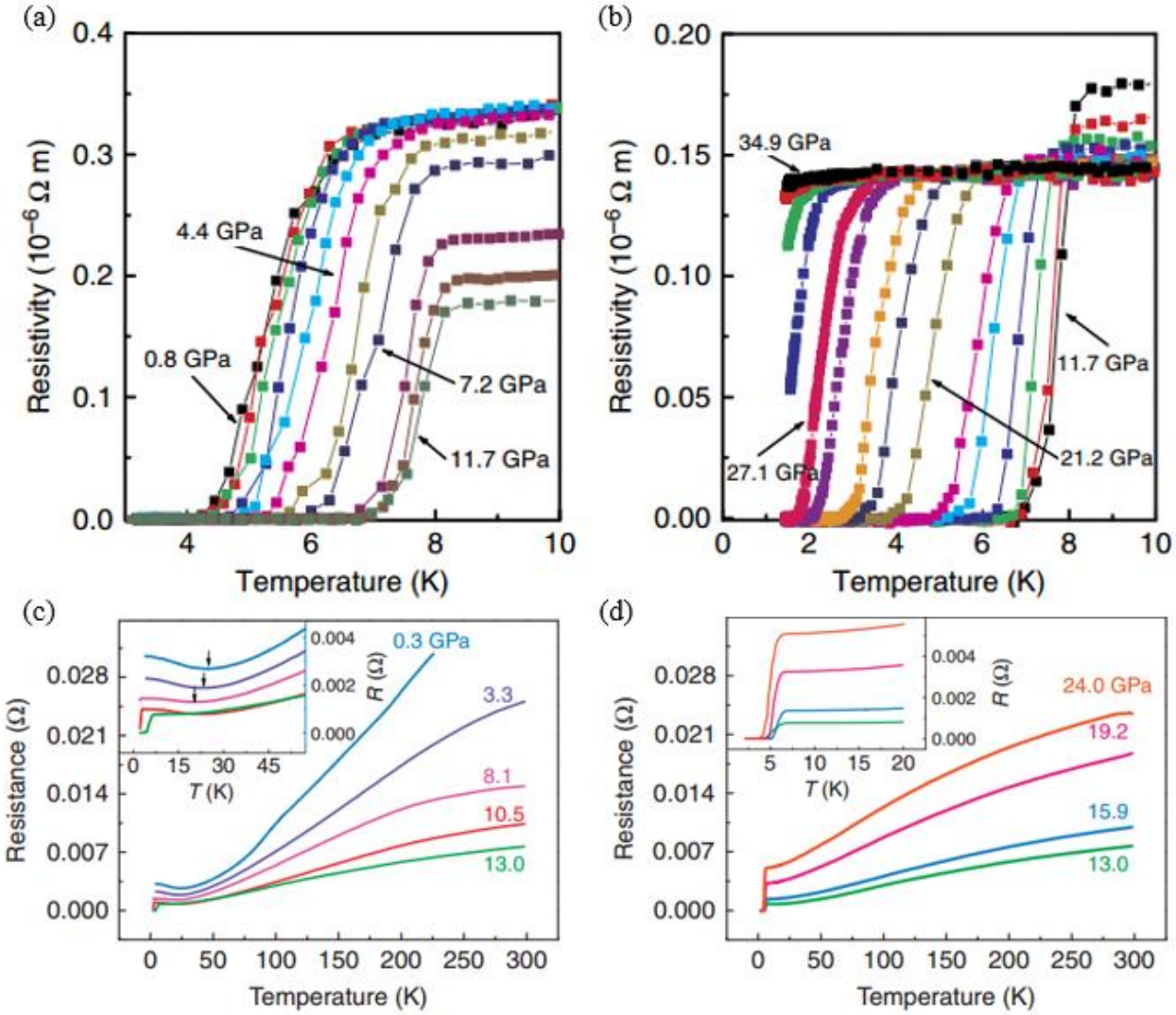

Figure 2.8 (a) and (b) Temperature dependent electronic resistivity of 1T'-$MoTe_2$ under different pressure.[52] (c) and (d) Temperature dependent electronic resistivity of T_d-WTe_2 under different pressure.[53]

2.2.3 Weak Antilocalization Effect (WAL)

Weak antilocalization (WAL) effect is originated from the Anderson Localization, which can induce a destructive quantum interference so that the backscattering of the electrons could be suppressed during the motion of the electrons at low temperature showing a high conductivity and low resistivity. An external magnetic field can break the quantum interference leading a cusp-like conductance quantum (e^2/h) with positive sign, which is

symmetric of the zero magnetic field.[54] Figure 2.9 shows the cusp-like WAL signal which has been reported in $MoTe_2$ (Figure 2.9 (a) and (b)) and WTe_2 (Figure 2.9 (c) and (d)), indicating the presence of the strong spin-orbit coupling (SOC) effect.[11,55] Specifically in $MoTe_2$ system, the cusp-like WAL signal is found when the magnetic field is perpendicular to the plane of the material while the signal is disappear when the magnetic field is tilted 90°, suggesting the two-dimensional nature of the WAL effect. In conclusion, the emergence of the WAL effect is essential condition for the study of topological quantum properties.

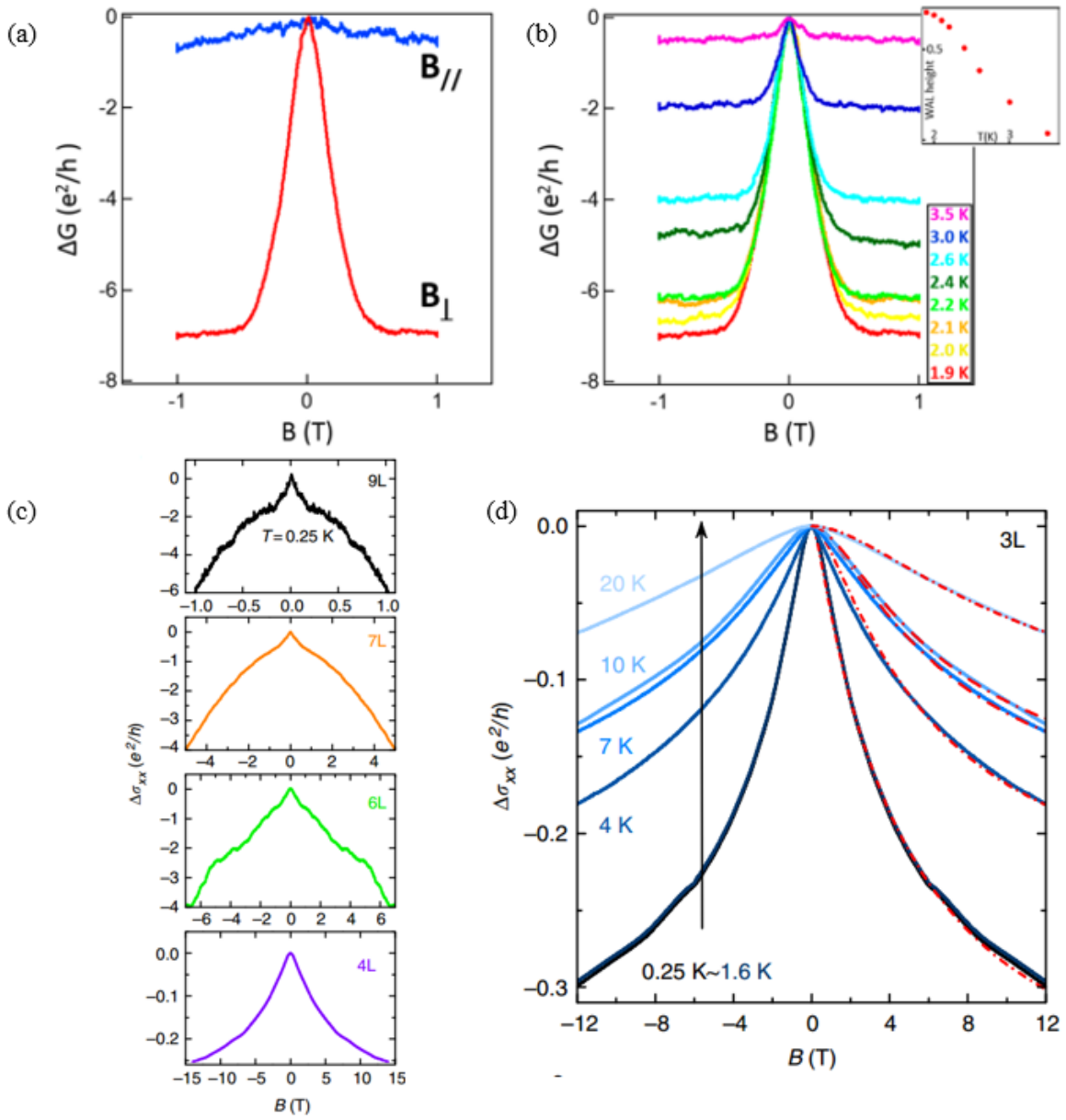

Figure 2.9 (a) and (b) The WAL cusp-like signal detected in $MoTe_2$. (c) and (d) The WAL cusp-like signal detected in WTe_2.[11,55]

2.3 Growth methods

2.3.1 The Chemical Vapor Deposition (CVD)

CVD is a typical kind of vapour-phase grow method. It mainly utilizes the vapour pressure of chemicals. Through increasing the temperature to enhance the chemicals' vapour pressure, the gas-phase chemicals are transferred by the carrier gas and the reaction would take place at certain temperature area. With the findings of interesting physical properties of $MoTe_2$ and WTe_2, the nanostructure engineering by CVD of these two materials are conducted widely. Generally speaking, the reported CVD methods can be classified into two types. One is coating the source material onto the substrate prior to the growth, which is called two-step method here and the other one use the source independently instead of coating, which is called one-step method.

For the two-step CVD method, it is a widely used method. Considering the high melting point of Mo and W element, the reaction may be difficult or slow if just put Mo and Te elements at the heating zone. Therefore, depositing Mo/W source onto the substrate first can solve this problem effectively. Besides, it will simplified the growth mechanism due to the combination of substrate and Mo/W source and the deposited Mo/W source acts like a catalyst on the substrate to facilitate the growth. The Te precursors will be vaporized first, transferred to the substrate and then the reaction took place on the substrate (Figure 2.10 (a)).

Different from the two-step CVD in which the Mo source material is coated onto the substrate prior to the growth, the Mo source material and the substrate are separated in one-step CVD making the experiment period much shorter as well as more economical than the two-step CVD. In one-step CVD process, both the transition metal precursors and the Te precursors are needed to be vaporized and then transported by the carrier gas to the substrate as shown in Figure 2.10 (b). The reaction could take place either during the vapour transportation or on the substrate. So far, only two published papers have reported to grow $MoTe_2$ and WTe_2 with one-step CVD method as listed in Table 2.3.

During the CVD process, several control factors need to be considered, such as the source material, the heating temperature, the growth time and the flow rate of the carrier gas. The summarization of the parameters of each factor is listed in Table 2.3. The detailed description of each parameters will be followed.

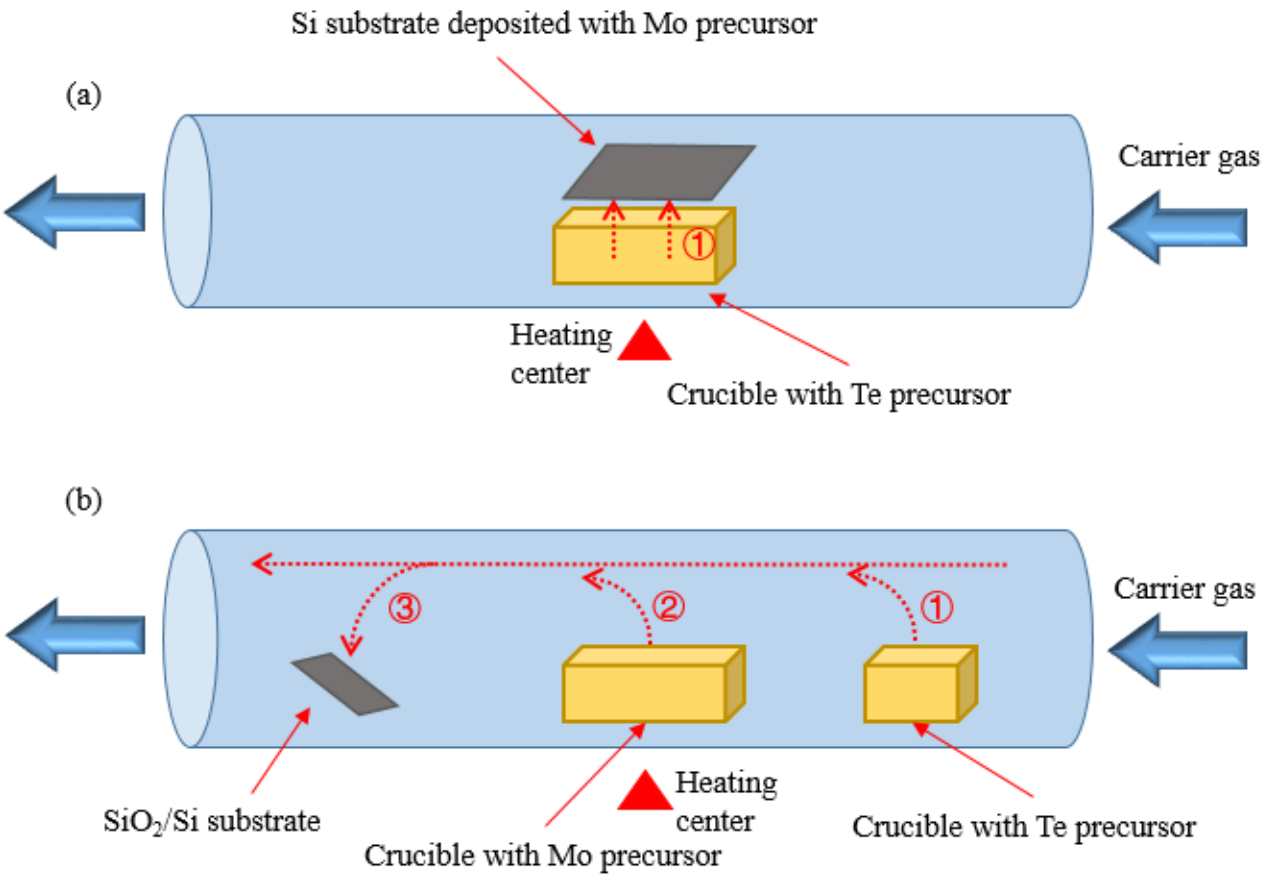

Figure 2.10 (a) and (b) Schematic experimental diagrams of two-step CVD and one-step CVD method, respectively.

Table 2.3 Summarization of the parameters of each factor in CVD method.

Product	Morphology	Mo/W precursor	SiO_2/Si substrate position	Coating method	Te precursor	Carrier gas (Flow rate)	T (t)	Ref
1T'-$MoTe_2$	Thin films	Mo film (~1 nm)	Center	EBD	Te powder	3 sccm Ar+ 4 sccm H_2	700 °C (1 h)	31
	Thin films	MoO_3 film			Te powder (0.18 g)			

1T'-$MoTe_2$	Thin films	Mo film (~1 nm)	Center	EBD	Te powder	3 sccm Ar+4 sccm H_2	700 °C (1 h)	10
2H-$MoTe_2$	Thin films	MoO_3 film (~1 nm)						
2H- and 1T'-$MoTe_2$	Films	MoO_3 film	Center	Not mentioned	Te powder (0.1 g)	3 sccm Ar+4 sccm H_2	650 °C (30 min)	29
	Films							
1T'-$MoTe_2$	Thin flakes	Ammonium heptamolybdate (AHM)	Downstream	Dip coating	Te (15 mg)	400 sccm N_2+ 25 sccm H_2	700 °C (5 min)	11
1T'-$MoTe_2$	Thin flakes	MoO_3		Thermal evaporation				
2H- and 1T'-$MoTe_2$	Film	MoO_3	Center	Thermal evaporation	Te (180 mg)	3 sccm Ar+4 sccm H_2	700 °C (1 h)	13
2H-and 1T'-$MoTe_2$	Thin films	MoO_3	Downstream	Thermal evaporation	Te powder (0.3 g)	4 sccm H_2+ 1, 3, 10, 20, 100 sccm N_2	650, 700, 750, 800 °C (2h)	15
1T'-$MoTe_2$	Thin flakes	Ammonium heptamolybdate	Downstream	Spin coating	Te pellet (0.3 g)	10sccm H_2	610 °C (30 min)	5
1T'-$MoTe_2$	Thin films	Mo thin film (~50 nm)	Downstream	EBD, magnetic	Te powder (2 g)	500 sccm Ar + 100 sccm H_2	650 °C (2 0 min)	27

2H-$MoTe_2$	Thin films			sputtering			650 ^oC (3 h)	
1T'-$MoTe_2$	Flakes	Ammonium heptamolybdate	Downstream	Dip coating	Te (15 mg)	400 sccm N_2+ 25 sccm H_2	700 ^oC (5 min)	7
2H-$MoTe_2$	Films	MoO_3 powders	Center	NA	Te powders	0.05 SCFH Ar + 0.05 SCFH H_2	650 ^oC, 15 min	17
1T'-$MoTe_2$	Films	MoO_3 powders	Center	NA	Te powders	0.05 SCFH Ar + 0.05 SCFH H_2	680 ^oC, 15min	17
1T'-$MoTe_2$	Thin films	MoO_3: $MoCl_5$: Te = 1:1:1(30 mg)	Downstream	NA	Te powders (0.5g)	200 sccm Ar + 15sccm H_2	780 ^oC (5-15min)	18
T_d-WTe_2	Thin flakes	WO_3 (~5 nm)	Downstream	Thermal evaporation	Te powder (25 mg)	350 sccm N_2 + 22 sccm H_2	650 ^oC (6 min)	39
	Thin flakes	Ammonia metatungstate		Spread with a brush				
T_d-WTe_2	Nanosheets	W (~1 nm)	Downstream	Magnetic sputtering	Te powder (50 mg)	70 sccm: Ar (90 %) + H_2 (10 %)	760 ^oC (1 0 min)	16
T_d-WTe_2	Thin films	W (~0.4, 1, 2, 4, 7, 10, 30 nm)	Center	Magnetic sputtering	Te powder (1-2 g)	80-150 sccm H_2	800 ^oC (50 min)	6

T_d-WTe_2	Thin films	WO_3: WCl_5: Te = 1:1:1 (30 mg)	Downstream	NA	Te powders (0.5 g)	200 sccm Ar + 15 sccm H_2	820°C (5-15 min)	[18]

- **Source material**

The source material can be separated into Mo/W source and Te source. For Mo/W source, there are two main choices. One is the simple substance (Mo/W elements) [10,16,27,31] and the other one is the oxide (MoO_3/WO_3) [5,7,11,13,15,29,39]. As for the Te source, usually people are using the Te powder as the precursor. In the work done by L. Zhou's group [31], they study and compare the results of the final phase of $MoTe_2$ grown by different precursor. They found that by using simple substance Mo elements, the 1T'-$MoTe_2$ with rough surface can be synthesized at 700 °C for 1h with 3 sccm Ar and 4 sccm H_2. Under the same condition, changing the precursor from Mo into MoO_3 can lead to a 1T'-$MoTe_2$ with more uniform surface, which is confirmed by both Raman spectra, AFM and TEM [31]. Further increasing the amount of Te precursors, the uniform-surface 1T'-$MoTe_2$ will transfer to 2H phase, which is confirmed by both Raman spectra and TEM [10]. Therefore, the final phase of $MoTe_2$ can be successfully controlled by the choice of Mo precursors and by the amount of Te precursors at 700 °C for 1 h with 3 sccm Ar and 4 sccm H_2 (Figure 2.11 (a)) [31]. In one-step CVD, Te precursors, Mo/W precursors and substrates are separated, usually put at upstream, centre and downstream, respectively (Figure 2.10 (b)). The biggest problem is that for transition metal simple substance, the melting point is relatively high which is not suitable for one-step CVD growth (Table 2.3). Therefore, the oxide and chloride with much lower melting point are used to provide the source. Furthermore, it is reported that mixing Te precursors with Mo/W precursors can lower the melting points of the chemicals.[56] However, it is reported that only particles will be obtained in the combination of MoO_3+ Te (Figure 2.11 (b)) and nothing can be obtained in the combination of WO_3+ Te (Figure 2.11 (e)). Besides, very thick particles will be obtained in the combination of $MoCl_5$+ Te (Figure 2.11 (c)) or WCl_6+ Te (Figure 2.11 (f)). Only when using the combination of MoO_3+ $MoCl_5$+ Te (Figure 2.11 (d)) or WO_3+ WCl_6+ Te (Figure 2.11 (g)), thin films can be obtained.[18]

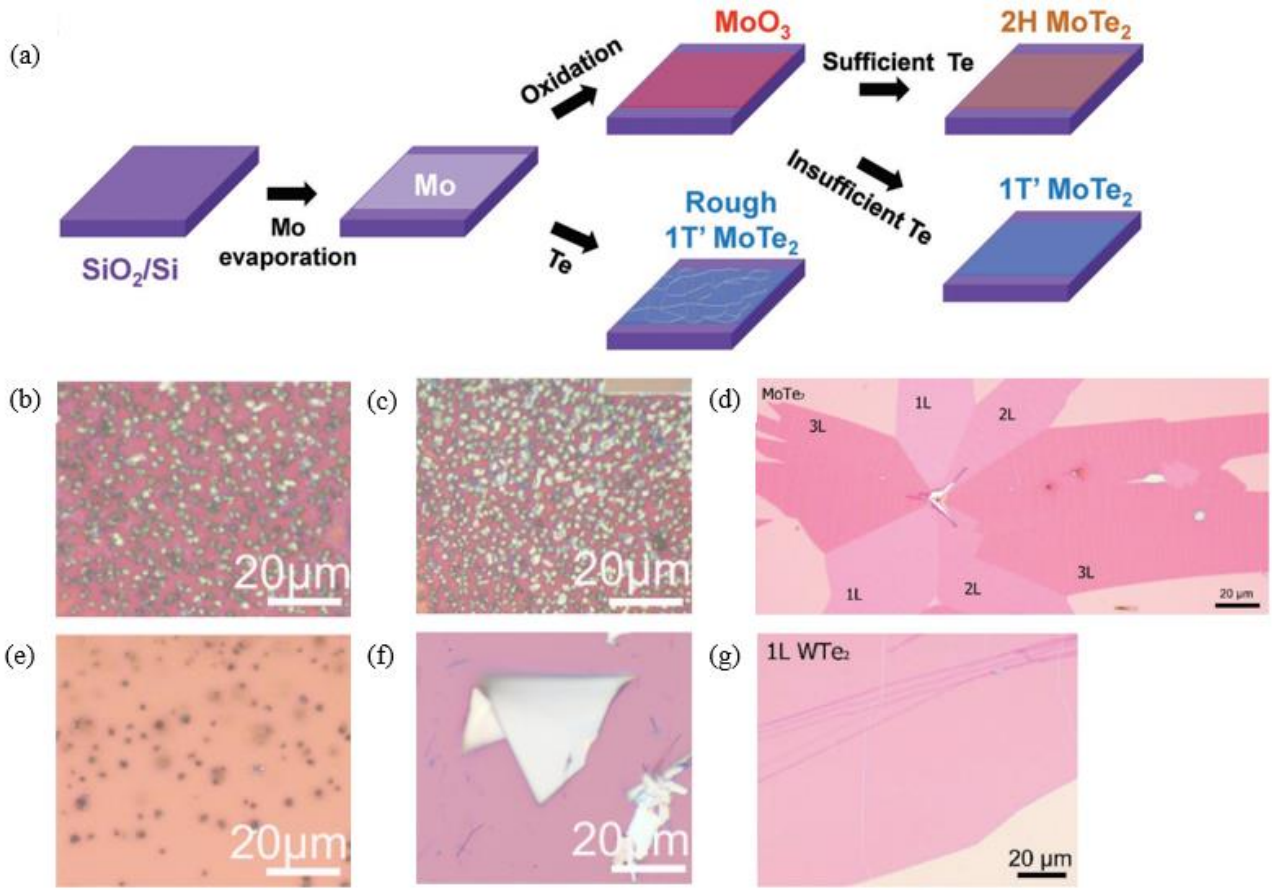

Figure 2.11 (a) Schematic diagram of the impact of the source materials on the phase of $MoTe_2$.[31] (b)-(d) Optical images of as-grown $MoTe_2$ with the precursors of MoO_3+ Te, $MoCl_5$+ Te and MoO_3+ $MoCl_5$+ Te. (e)-(g) Optical images of as-grown WTe_2 with the precursors of WO_3+ Te, WCl_6+ Te and WO_3+ WCl_6+ Te.[18]

Table 2.4 Summarization of the melting point and boiling point of some common Mo and W precursors.

Material	Mo	MoO_3	$MoCl_5$	W	WO_3	WCl_6	Te
Melting point (°C)	2623	795	194	3422	1473	275	450
Boiling point (°C)	4639	1155	268	5555	1700	346.7	988

❖ **Heating temperature**

In CVD process, the temperature includes vaporization temperature and growth temperature. As the melting point of Te is low and easy to achieve, the growth temperature and the vaporization temperature of transition metal are the keys. For two-step CVD method, as the transition metal are deposited onto the substrate, only the growth temperature should be considered. As for the one-step CVD method, the vaporization temperature of the transition metal should be considered first as they are of high melting point.

Among all the papers related to the synthesis of $MoTe_2$ by CVD, the synthesis temperature is mainly focus on the range of 650 ^oC to 760 ^oC (Table 2.3). In Li Yang's work,[15] they also studied the phase transition of $MoTe_2$ under different temperature as shown in Figure 2.12 (a) and 2.12 (b). It is noted that the substrate is put at downstream from the tube centre, which means the growth temperature is lower than the heating temperature. It is found that with increasing the temperature, the first stage is the transition from 1T' phase to 2H phase and the second stage is the transition from 2H phase to 1T' phase (The critical temperature is around 750 ^oC in this case), which is confirmed by the Raman spectrum and optical microscope.[15] Besides, the impact of the temperature is not as significant as the types of precursors. By controlled the temperature, the transition between 1T' phase and 2H phase cannot be realized. Only the transition between pure phase and hybrid mixed phases can be obtained.[15] As for WTe_2, the synthesis temperature is slightly higher than $MoTe_2$ as the higher melting point of W and W derivative, ranging from 650-820 ^oC. As the phase of WTe_2 is single, no phase transition issue in this case.

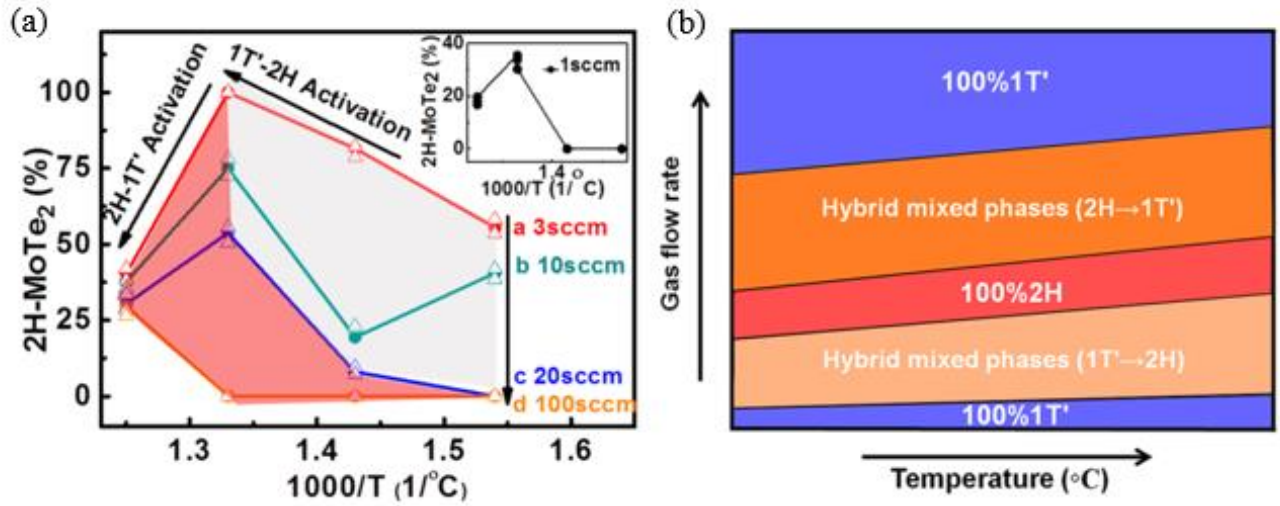

Figure 2.12 Relationship between growth temperature and the final phase of $MoTe_2$ under different gas flow rate.[15]

❖ **Flow rate of the carrier gas**

In the growth of $MoTe_2$ (WTe_2), the mixture gas of H_2 and N_2 (Ar) is the most commonly used carrier gas not only to prevent the precursors and products being oxidized but also to facilitate the reaction between Mo and Te precursors. Theoretically, the flow rate of the carrier gas will influence the tellurization speed on the substrate and thus affect the quality of final products. In Li Yang's work,[15] they studied the contribution of the flow rate of carrier gas to the final phase of $MoTe_2$ at 750 °C with MoO_3 as precursor. The whole flow rate of N_2 and H_2 is controlled by the flow rate of N_2 in this case. The trend of the phase transition with the increasing of the flow rate of N_2 is obvious in Figure 2.13. Through controlling the flow rate of N_2, the phase transition between pure 1T' phase and pure 2H phase can be realized successfully, which is characterized by the Raman spectrum of characteristic peaks of each phase.[15] Therefore, the tellurization speed controlled by the flow rate is crucial to the growth of $MoTe_2$.

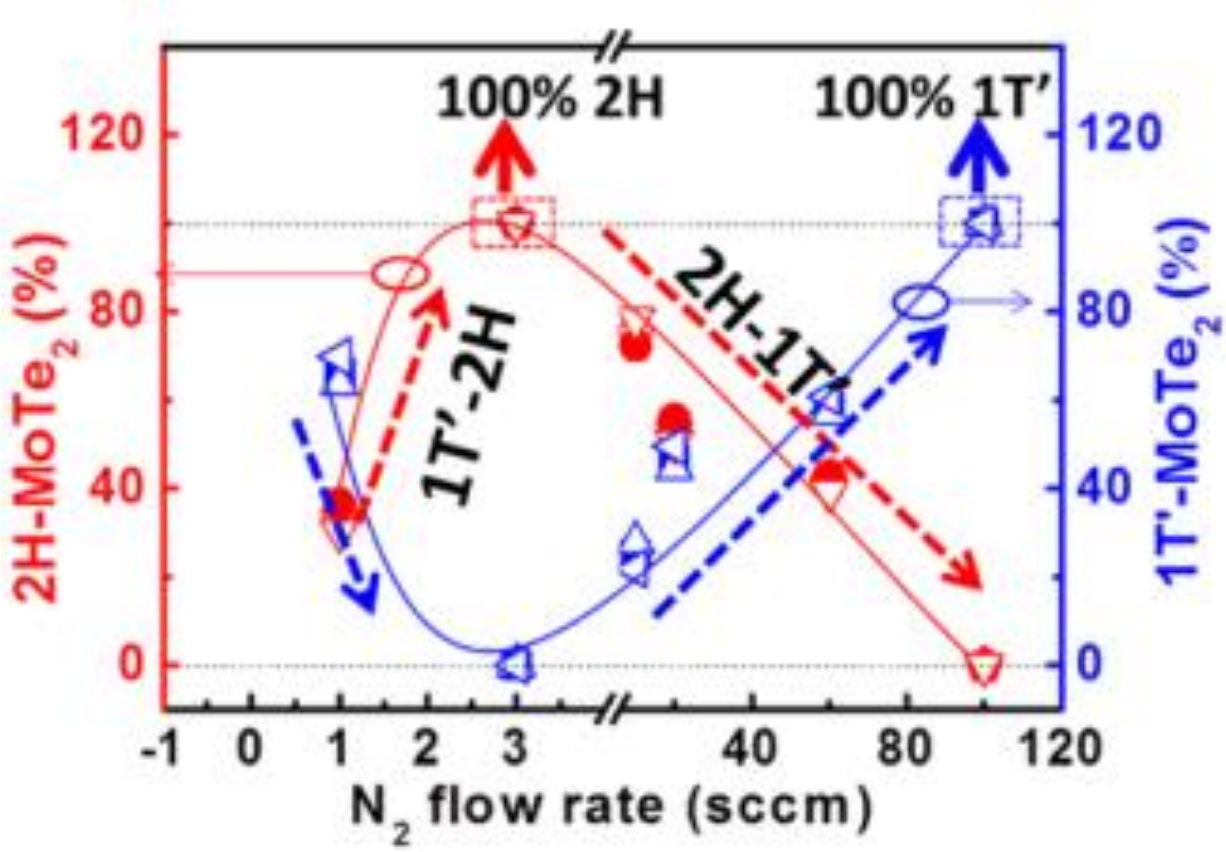

Figure 2.13 The N_2 flow rate dependent phase transformation between 1T' phase and 2H phase of $MoTe_2$.[15]

❖ **Growth time**

Growth time, as an important parameter of chemical reaction, is used to control the extent of the reaction. For $MoTe_2$, it is reported by Jin Cheol Park's group that different growth time leads to a different phase of $MoTe_2$ synthesized by CVD.[27] The whole growth process is carried out with Te powders and Mo element at 650 ^oC from 0 to 180 min with 500 sccm Ar + 100 sccm H_2. It is found that with the increasing of the growth time, the percentage of 1T'-$MoTe_2$ is decreasing from 100 % to 0 while 2H-$MoTe_2$ is increasing from 0 to 100 %, indicating the CVD growth is initiating from 1T' phase and transferring to 2H phase (Figure 2.14 (a)). These results are confirmed by XRD, Raman spectrum and TEM.[27] For WTe_2, it is reported by Jiazhou Dong's group that the thickness of the WTe_2 thin flakes is positive proportional to the growth time (Figure 2.14 (b)), which is confirmed by both the optical microscope and AFM.[18]

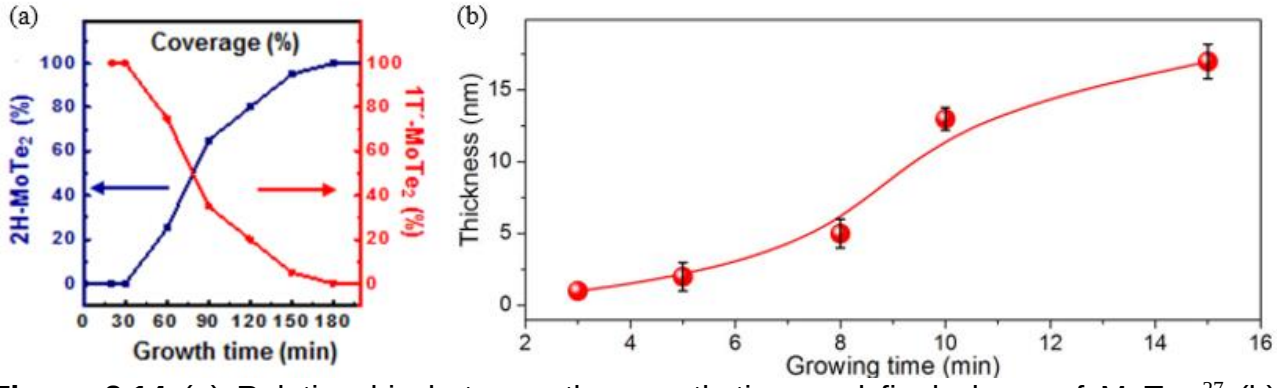

Figure 2.14 (a) Relationship between the growth time and final phase of $MoTe_2$.[27] (b) Relationship between the growth time and the thickness of WTe_2 thin flakes.[18]

2.3.2 The Chemical Vapor Transport (CVT)

CVT is another common vapour-phase grow method. Different from CVD, the basic mechanism of CVT is to use a halogen transport agent to form an intermediate product, halide, to realize gas reaction. Although transition-metal elements are of high melting points and inertness, it is easily to react with halogens at relatively high temperature and the halides have a tendency to decompose at relatively low temperature. The whole reaction takes place in a small sealed tube. Normally, the precursors and the transport agent are put at the higher-temperature area. Then the transport agent will react with the precursors to form the

halide of transition metal in gas phase. The gas-phase halide will be transported to the lower-temperature area by the temperature gradient. At lower-temperature area, the gas-phase halide will release the halogen transport agent and leave the solid-phase products. The halogen transport agent will then be transported to higher-temperature area by the concentration gradient (The concentration of halogen transport agent is low at higher-temperature area due to the continuous consumption). Therefore, a cyclic reaction process is formed (Figure 2.15).

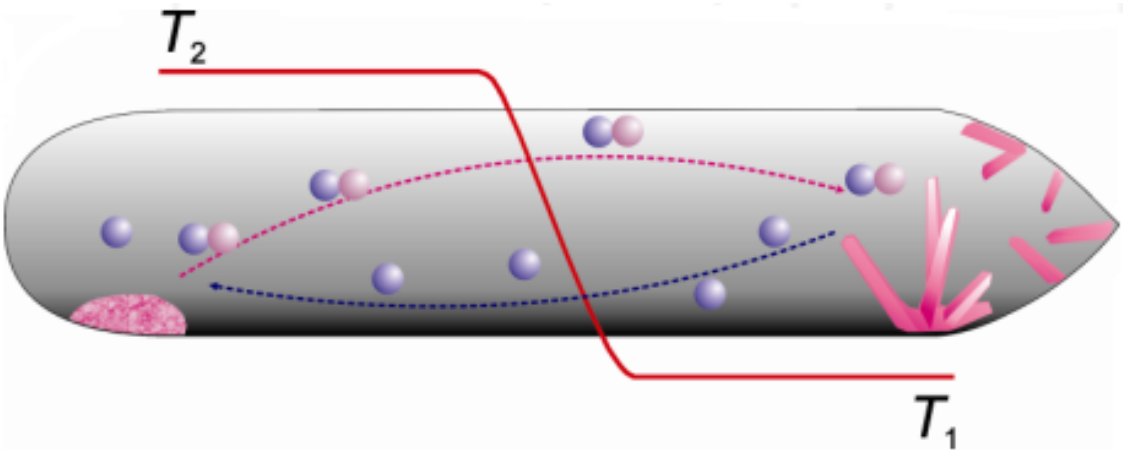

Figure 2.15 Schematic diagram of CVT process.[57]

- **Precursors**

Similar with CVD growth, CVT can also be classified into two-step CVT and one-step CVT based on different types of precurosrs. The one-step CVT is just using the single substance Mo/W and Te powders. As for two-step CVT, the single substance Mo/W and Te powders are put together to form polycrystalline $MoTe_2$/WTe_2 by solid-state reaction before the CVT growth. In fact, the mechanism is the same. Synthesizing a polycrystalline $MoTe_2$ prior to CVT is just like accelerating the one-step CVT progress.

- **Transport agent**

The transport agent in CVT growth is of significant impact in the reaction. The frequently-used transport agent are the $MoCl_5$/WCl_6, I_2/Br_2 and $TeCl_4$/$TeBr_4$. The basic reason to use

halide or halogen in this case is to utilize the high-reactivity between Mo/W and halogen to improve the problem caused by the inertness of Mo/W. Equation (1) is a general reaction of Mo, Te and $MoCl_5$.[58] The reaction mechanism of the other transport agent can be referred to equation (1).

$$\mathrm{Mo(s) + 2MoCl_5(s) + 6Te(s) \rightarrow 3MoTe_2(s) + 5Cl_2(g)} \quad (1)$$

- **Temperature**

The suitable temperature set in CVT should meet the basic requirement of the reaction equilibrium constant K_p=1 or ($\Delta_r G^0_T$=0).[57] The definition of the Gibbs free energy and the equilibrium constant are shown in equation (2) and (3), respectively. If the K_p=1 or ($\Delta_r G^0_T$=0), the suitable temperature, which is the average temperature T_a of high temperature and low temperature, can be simply calculated by the thermodynamic data of the entropy and enthalpy as shown in equation (4). The more specific data, the more specific results. However, people usually use the thermodynamic data at room temperature to roughly estimate the suitable temperature. Although the value may not be accurate, it is still said that a range of ±100 K of the calculated value is suitable for the transport.[57]

$$\Delta_r G_T^0 = -\Delta_r H_T^0 - T \cdot \Delta_r S_T^0 \quad (2)$$

$$\ln K = \frac{-\Delta_r H_T^0}{R \cdot T} + \frac{\Delta_r S_T^0}{R} \quad (3)$$

$$T_a = \frac{\Delta_r H_T^0}{\Delta_r S_T^0} \quad (4)$$

- **Cooling**

The cooling process is mainly decided on the phase desired. For $MoTe_2$, 2H phase is a room-temperature phase while 1T' is a high-temperature phase (Figure 2.1). Therefore, to obtain the 1T' phase, quenching from over 900 °C is required to maintain high-temperature structure. Instead, natural cooling can obtain 2H-$MoTe_2$. As there are no phase transition in WTe_2, natural cooling is chosen.

Table 2.5 Summarization of the parameters of each factor in CVT method.

Products	Morphology	Precursors	Transport agent	Temperature (High-Low) and time	Cooling	Ref
1T'-$MoTe_2$	Single crystal bulk (17*10*2 mm^3)	Polycrystalline $MoTe_2$	$TeBr_4$ (5 mg/cm^3)	1050 ^oC- 950 ^oC (7 days)	Not mentioned	28
1T'-$MoTe_2$	Needlelike crystal (10 mm*1 mm)	Mo, Te powders	$TeBr_4$ (3 mg/cm^3)	1000 ^oC- 900 ^oC (100 h)	Quenching	32
1T'-$MoTe_2$	Single crystal needle	Mo, Te powders	Br_2	Not mentioned	Quenching	35
1T'-$MoTe_2$	Rectangular bulk	Mo, Te powders	$TeCl_4$	980 ^oC- 900 ^oC (7 days)	Quenching	36
1T'-$MoTe_2$	Single crystal bulk	Polycrystalline $MoTe_2$	$TeCl_4$ (3 mg/mL)	1000 ^oC- 900 ^oC	Quenching	37
1T'-$MoTe_2$	Rectangular bulk	Polycrystalline $MoTe_2$ powders	$TeCl_4$	1000 ^oC- 900 ^oC (7 days)	Quenching	52
1T'-$MoTe_2$	Plate (4*4*0.5 mm^3)	Polycrystalline $MoTe_2$	I_2	1000 ^oC- 900 ^oC (7 days)	Quenching	59
1T'-$MoTe_2$	Plate (10*2*0.2 mm^3)	Mo, Te powders	I_2	1000 ^oC- 920 ^oC (7 days)	Natural cooling	60,61
1T'-$MoTe_2$	Single crystal bulk	Polycrystalline $MoTe_2$	$TeCl_4$ (<=2.7 mg/mL)	Not mentioned (3 days)	Quenching	34,62
1T'-$MoTe_2$	Single crystal bulk	Polycrystalline $MoTe_2$	I_2 (4 mg/cm^3)	1000 ^oC- 950 ^oC (168 h)	Quenching	63

2H- and 1T'-$MoTe_2$	Single crystal bulk	Not mentioned	I_2	Not mentioned	Not mentioned	64
2H-$MoTe_2$	Single crystal bulk (24*16*2 mm^3)	Polycrystalline $MoTe_2$	TeB_4 (5 mg/cm^3)	800 ^oC- 750 ^oC (7 days)	Not mentioned	28
2H-$MoTe_2$	Not mentioned	Not mentioned	Br_2	Not mentioned	Not mentioned	65
2H-$MoTe_2$	Single crystal bulk	Mo, Te powders	$MoCl_5$	(600-900 ^oC)-(530-800 ^oC) (2 days-7 days)	Natural cooling	58
T_d-WTe_2	Large single crystal bulk	W, Te powders	Br_2	750 ^oC- 650 ^oC (7 days)	Not mentioned	40
T_d-WTe_2	Rectangular bulk	Polycrystalline WTe_2 powders	$TeCl_4$	930 ^oC- 880 ^oC (7 days)	Not mentioned	41
T_d-WTe_2	Thin ribbons	W, Te powders	Br_2	750 ^oC- 650 ^oC (7 days)	Not mentioned	46
T_d-WTe_2	Large plates and flat needles	W, Te powders	$TeBr_4$ (2 mg/cm^3)	820 ^oC- 700 ^oC (8 days)	1 day	47
T_d-WTe_2	Bulk	W, Te powders	WCl_6	890 ^oC- 790 ^oC (4 days)	Not mentioned	55,66
T_d-WTe_2	Bulk	W, Te powders	WCl_6	890 ^oC- 790 ^oC (4 days)	Not mentioned	66
T_d-WTe_2	Bulk	WTe_2 molecular powder	I_2 (5 mg/cm^3)	900 ^oC- 800 ^oC (14 days)	Not mentioned	67

T_d-WTe_2	Single crystal Sheet	W, Te powders	I_2	900 °C- 800 °C (7 days)	Not mentioned	68
T_d-WTe_2	Single crystal sheet (millimeter size)	Polycrystalline WTe_2 powders	$TeBr_4$ (3 mg/cm^3)	850 °C- 750 °C (7 days)	Not mentioned	69
$Mo_xW_{1-x}Te_2$	Single crystal bulk	W, Mo, Te powders	$TeCl_4$	750 °C- 650 °C (7 days)	3 days	4
$Mo_xW_{1-x}Te_2$	Single crystal ribbon	W, Mo, Te powders	I_2	1070 °C- 950 °C (7 days)	Natural cooling	70
1T′-$Mo_xNb_{1-x}Te_2$	Single crystal bulk	Mo, Nb, Te powders	I_2 (5 mg/cm^3)	(1050-1000 °C)- (920-900 °C) (7 days – 14 days)	Quenching	71

2.3.3 The Solid-State Reaction

Solid-state reaction is the most simplest synthesis method. However, the quality of the products is not very good, which are polycrystalline. Therefore, solid-state reaction is usually used to synthesize the polycrystalline $MoTe_2$/WTe_2 for the CVT as mentioned above.[28,34,52,59,62,63] There is an improved solid-state reaction, which is called flux method, can synthesize single crystalline $MoTe_2$/WTe_2 in large size. The key of this improvement is that the addition of NaCl (Melting point is 801 °C and boiling point is 1413 °C) or excessive Te precursors (Melting point is 450 °C and boiling point is 988 °C). As the synthesis temperature is around 1100 °C when using NaCl as solvent,[26,72-74] the NaCl becomes liquid under this temperature. The Mo/W and Te precursors can dissolute into the liquid phase and make the reaction more complete and faster. What's more, the liquid reaction environment can prevent the Te deficiency effectively.[26] As for the excessive Te precursors, the temperature is lower around 1000 °C also providing the liquid reaction environment. In this case, the high-temperature centrifuge to remove the excessive Te precursors is necessary. Otherwise, it may not produce $MoTe_2$ in the end according to the phase diagram

(Figure 2.1). In order to control the phase transition of $MoTe_2$, quenching from high temperature will lead to 1T' phase while natural cooling will lead to 2H phase. For WTe_2, the cooling is not significant.

Table 2.6 Summarization of the parameters in solid-state reaction and flux method.

Products	Morphology	Precursors	Pressure	Temperature and time	Cooling	Ref
$MoTe_2$	Powder	Mo, Te powders (1:2)	Vacuum	750 ^oC (2 days)	Not mentioned	28
$MoTe_2$	Polycrystalline powder	Mo, Te powders	Vacuum	800 ^oC (7 days)	Not mentioned	52
$MoTe_2$	Polycrystalline powder	Mo, Te powders (1:2)	Vacuum	800 ^oC (7 days)	Quenching	59
$MoTe_2$	Polycrystalline powder	Mo foil, Te ingot (1:2)	Vacuum	800 ^oC (3 days)	Not mentioned	34,62
$MoTe_2$	Polycrystalline powder	Mo, Te powders (1:2)	Vacuum	750 ^oC (3 days)	Not mentioned	63
1T'-$MoTe_2$	Polycrystalline bulk	Mo, Te powders	Vacuum	700-800 ^oC (72h)	Quenching	75
1T'-$MoTe_2$	Single crystal flake (2*1*0.1 mm^3)	Mo, Te powders (1:2) and NaCl	Vacuum	1100 ^oC (12 h)	1. $1100\ ^oC \xrightarrow{0.5^oC/h} 900\ ^oC$ 2. Quenching	26,72-74
2H-$MoTe_2$	Single crystal flake	Mo, Te powders (1:2) and NaCl	Vacuum	1100 ^oC (12 h)	$1100\ ^oC \xrightarrow{0.5^oC/h} RT$	26,74

1T'-$MoTe_2$	Single crystal bulk	Mo, Te powders (1:25)	Vacuum	1050 °C (1 day)	1. $1050\ ^oC$ $\xrightarrow{Slowly}$ $900\ ^oC$ 2. Centrifuge	76-78
1T'-$MoTe_2$	Single crystal bulk	Mo, Te powders (1:9)	Vacuum	1000 °C (7 days)	Not mentioned	79
T_d-WTe_2	Single crystal	W, Te powders (excessive Te)	Vacuum	1000 °C (5 h)	1. $1000\ ^oC$ $\xrightarrow{1^oC/h}$ $800\ ^oC$ 2. $800\ ^oC$ $\xrightarrow{5^oC/h}$ $700\ ^oC$ 3. Centrifuge	53,80

Chapter 3
Methodology

3.1 Synthesis Method

This experiment mainly use CVD as the synthesis method. CVD is a vapour phase growth method that source material are first vaporizing at high temperature, transferred by carrier gas, depositing on the substrate at low-temperature area and reacting to form the products. To conduct the CVD experiments mentioned in this thesis, there are four steps:

1. First is to clean the substrates prior to the experiment. To clean the substrates, the SiO_2/Si or Si substrates are soaked in the ethanol and acetone successively and then use ultrasonic to vibrate the substrates achieving cleaning. In the end, use the compressed air gun to dry the surface of the substrate.
2. Weigh the precursors in a specific amount and put them into a specified ceramic boat. Different precursors are put at different locations in order to control the temperature specifically. Then put the ceramic boat with source materials (Table 6) into the CVD furnace and set experimental parameters. Close the furnace and use Ar/H_2 gas to flush the chamber to prevent the disturbance of the oxygen in the air. Turn on the furnace and heat to the setting temperature.
3. When the reaction is complete and the temperature is cooling down, the substrates are removed from the furnace. The substrates with samples are stored it in the sample bottles for further characterization and sealed in under vacuum to prevent the oxidization.
4. After the characterizations of the samples, more experiments are needed to be conduct to modify and enhance the quality of the as-synthesized samples via tunning the growth parameters, including the types, the composition and the location of the

source materials, the growth temperature, the growth time, the composition and the flow rate of the carrier gas and the location of the substrates.

Based on using the one-zone tube furnace in this experiment, a few parameters can be controlled during the growth process. First is the heating temperature, which decides the whole temperature range of each experiment. The upstream vaporization temperature and downstream growth temperature away from the heating zone can be roughly estimated by the distance from the heating zone. Second is the temperature holding time, which decides the reaction time. Third is the carrier gas and the flow rate. Generally, the carrier gas act as a carrier and provide a certain environment for the reaction. In specific situation, the carrier gas can also react with the source material to form some intermediate products, which should be carefully considered when choosing the carrier gas. Besides, the flow rate of the carrier gas could affect the reaction speed that should be tuned carefully.

In this work, all the chemicals using in this experiment have been listed in Table 3.1. During the synthesis process, all the equipment and instruments that have been used mainly including a horizontal single-zone tube furnace (GSL 1500x, China), ultrasonic (Thermoline sientific), electronic analytical balance (Sartorius CPA225D), flow meter (CS200, Sevenstar) and vacuum sealer (Russel Hobbs). $Mo_xW_{1-x}Te_2$ nanomaterials were synthesized by CVD in a horizontal single-zone tube furnace using MoO_3 powders (99.995 %, Sigma Aldrich) as the Mo sources, and WO_3 powders (99.97 %, Sigma Aldrich) and WCl_6 powders (99.9 %, Sigma Aldrich) as the W sources. The Te powders (99.999 %, Alfa Aesar) were used as the Te sources. ~30 mg mixed powders of WO_3, WCl_6 and Te were placed at the heating centre of the tube furnace. ~10 mg MoO_3 powders were placed at 3 cm upstream from the centre. ~250 mg Te powders were placed at 12 cm upstream from the centre. Noted that the Te powders in the mixed powders were to lower the melting point of the mixed powders, while the Te powders at the upstream was aimed to provide the Te atmosphere during the whole process.[18] A 300 nm SiO_2/Si substrate was placed vertically at 8 cm downstream from the centre. The furnace was then heated to 710 ^oC in 20 min, and maintained for 120 min with 100 sccm Ar and 15 sccm H_2. The furnace was cooling down naturally. As comparisons, two similar synthesis processes, without the addition of MoO_3 powders and the mixed powders (WO_3, WCl_6 and Te), were used to fabricate WTe_2 and $MoTe_2$ nanomaterials, respectively.

Table 3.1 Lists of chemicals used in CVD experiment.

Chemicals	Formula	Supplier	Particle size	Purity
Tellurium	Te	Alfa Aesar	60 mesh	99.999 %
Molybdenum(VI) Oxide	MoO_3	Sigma Aldrich	-	99.97 %
Tungsten(VI) Oxide	WO_3	Sigma Aldrich	-	99.995 %
Tungsten(VI) Chloride	WCl_6	Sigma Aldrich	-	99.9 %
Silicon substrate with 300 nm silica layer	SiO_2/Si	MTI	-	-
Hydrogen gas	H_2	Coregas	-	99.999 %
Argon gas	Ar	Coregas	-	99.9995 %

3.2 Characterization Method

3.2.1 X-Ray Diffraction (XRD)

X-Ray Diffraction (XRD) is a one of the basic research tools, which can let researchers have a general concept of what a material contains. X-Ray is a kind of electromagnetic wave. When the X-Ray irradiates a material, it will hit the electrons inside the material and emit many other X-Rays that are called the scattered X-Rays. These scattered rays can be coherent with each other, which will lead to strengthening in some directions while weakening in other directions. This is the basis of X-Ray Diffraction pattern. People analyse the diffraction spectrum of the material to obtain the component as well as the structure or the morphology of the atom or the molecule inside the materials. The diffraction pattern produced of each crystal is representing the rules of the atomic distribution inside the crystal, which means it is unique. Nowadays, the XRD has been an effective way to study the micro structure of the crystal and some amorphous substance. One of the most common application is the Phase Analysis. It is categorized into two parts: qualitative analysis and quantitative analysis. First, comparing the diffraction pattern obtained from testing the materials to the standard diffraction pattern (Peak position), the substance of the material can be known. Then for those that are not single phase or containing impurities, comparing the intensity of each peak, the content of each phase in the material can be obtained. What's

more, many XRD analysis software (Such as Jade, X'pert high score, etc) can be used to analyse the XRD data instead of searching for the Powder Diffraction File (PDF) cards by hand and comparing the d value, which effectively increase the speed of identifying the materials.

In this experiment, the Bruker D8 Advance MKII XRD made by America is used (Figure 3.1). No pretreatment needed to be done for the samples on the substrate. The source of the radiation is the Copper target Kα with λ= 0.15418 nm. The scanning range 2θ is from 10^{o} to 90^{o} with the steps of 0.02^{o}.

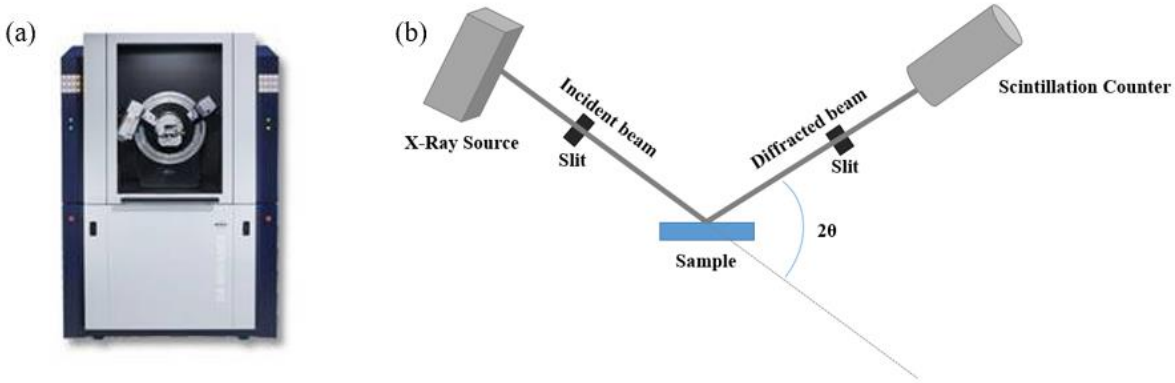

Figure 3.1 (a) Bruker D8 Advance powder XRD machine. (b) Schematic diagram of the working principle of powder XRD machine.[81]

3.2.2 Optical Microscopy (OM)

Optical microscope (OM) is the simplest microscope, which mainly uses the optical lens to produce image magnification. It usually can be classified into reflection type and transmission type. Relection-type OM is usually used to observe some thick samples, such as chemical materials. As for the transmission-type OM, it is used to observe thin or transparent samples so that the visible light can go through the samples to the eyepiece, which is mainly used in the observation of biological tissue.

In this experiment, the Olympus AX70 optical microscope (Made by Japan) is used to observe the as-grown sample after growth, in order to give a quick and direct understanding of the morphology and color of the as-grown sample.

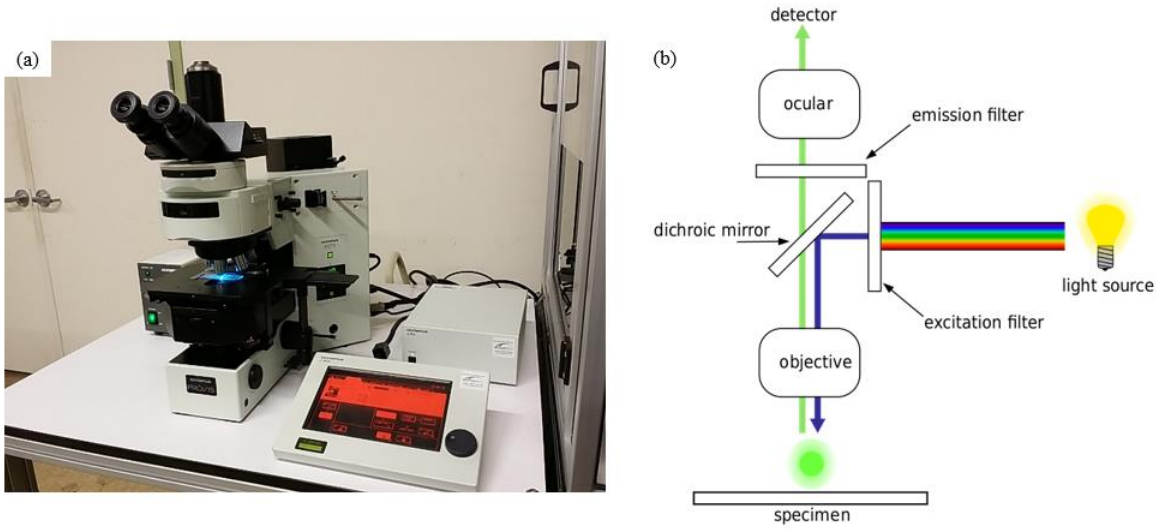

Figure 3.2 (a) Image of Olympus AX70. (b) The light path of a reflection-type optical microscope.[82,83]

3.2.3 Scanning Electron Microscopy (SEM)

Scanning Electron Microscopy (SEM) is a kind of observation techniques for micro morphology with high resolution between Optical Microscope and Transmission Electron Microscope. When the high-energy electron beam hits the surface of the specimen, many kinds of electrons or signals will be produced (Figure 3.3) such as secondary electrons, back-scattering electrons, absorption electrons, transmission electrons, etc. These electrons will receive by detector and form the corresponding image, which is good for our analysis. SEM image can directly give a microscopic imagery to the materials of the samples surface to analyse its surface morphology, microstructure and elements distribution. It has three main advantages. First, the magnification times of the SEM is relative high and it can achieves continuous adjustment from twenty to two hundred thousand times. Secondly, it has a huge depth of field, wide horizon and three-dimensional imagery, which can help us directly observe various micro structures with accidented surface. At last, it can achieve dynamic observation of the phase change and morphology change under various experimental conditions. What' more, the SEM also equips with an energy dispersal x-ray spectroscopy (EDS) nowadays. Researchers can observe the morphology of the microstructure and analyse the components of the micro area. The SEM-EDS is the simplest and most common compositional characterization. Therefore, SEM has played a more and more important role in our scientific research nowadays.

In this experiment, the JEOL JSM-7100F with energy-dispersive X-ray spectroscopy (EDS) made by Japan is used to determine the detailed morphology and the composition of the as-grown nanostructures. The working voltage is 15 kV.

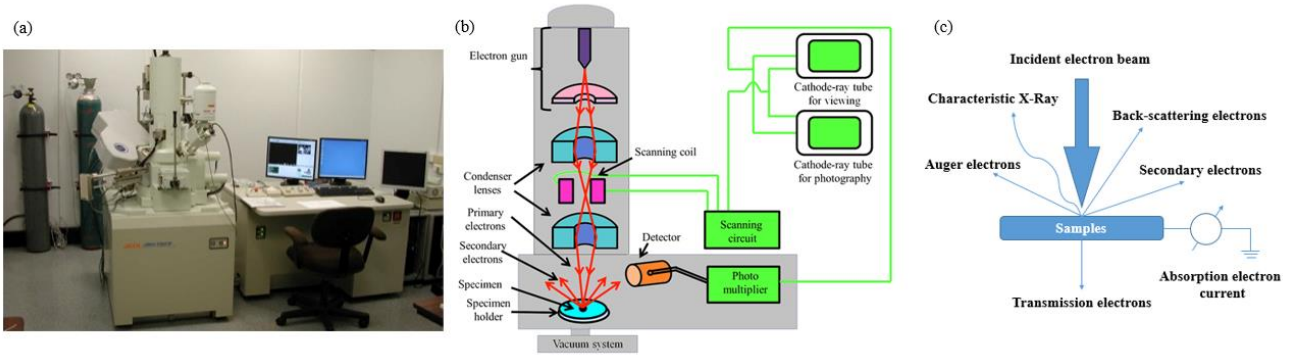

Figure 3.3 (a) Image of JEOL 7100F. (b) The schematic diagram of SEM mechanism. (c) The schematic diagram of different signals after the incident electron beam hit the samples.[84,85]

3.2.4 Transmission Electron Microscopy (TEM)

The Transmission Electron Microscopy (TEM) is a kind of high resolution and large magnification electronic optical instrument using the electron beam with very short wavelength to illuminate and electro-magnetic lens to focus imaging. Actually, its structure is very similar to the Optical Microscope. Except for the electron gun and the fluorescent screen, the main difference is that TEM uses electro-magnetic lens, such as condenser lens, objective lens, intermediate lens and projector lens, to focus imaging just the same as the function of convex lens (Figure 3.4). There are four main applications of TEM in materials characterizations. First is the bright-field TEM image (BFTEM). Under BFTEM image, the sample can be observed clearly to give a whole view of the morphology at low magnification. Second is the high-resolution TEM image (HRTEM). The resolution of TEM is so high that it can reach nano scale and the magnification is up to million, which make it easily to observe the microstructure even atom structure. Third is the EDS. TEM-EDS can provide more accurate and reliable composition information of the sample than SEM-EDS. Four is the selected area electron diffraction (SAED). SAED is a typical application of the Bragg equation in TEM. Through a transition from positive space to reciprocal space, the crystal plane is transform into a small spot. Each spot represents a crystal face. The distance between the spot to the diffraction spot is the d-spacing and the angle between two planes

can be measured directly. The pattern of the SAED image is also a useful information when analysing the SAED image. For single crystal, the diffraction pattern is made up by many regular spots, which is corresponding to its crystal structure. For polycrystal, a few sets of diffraction patterns or the polycrystalline diffraction rings can be observed. For non-crystal, amorphous diffraction rings can be observed. Analysing the diffraction pattern can determine the lattice type and the lattice parameters of the crystals and finally confirm the phase.

In this experiment, the Philips Tecnai F20 FEG-S/TEM equipped with EDS is used to do the further structure analysis and the more accurate composition analysis. The accelerating voltage is 200 kV.

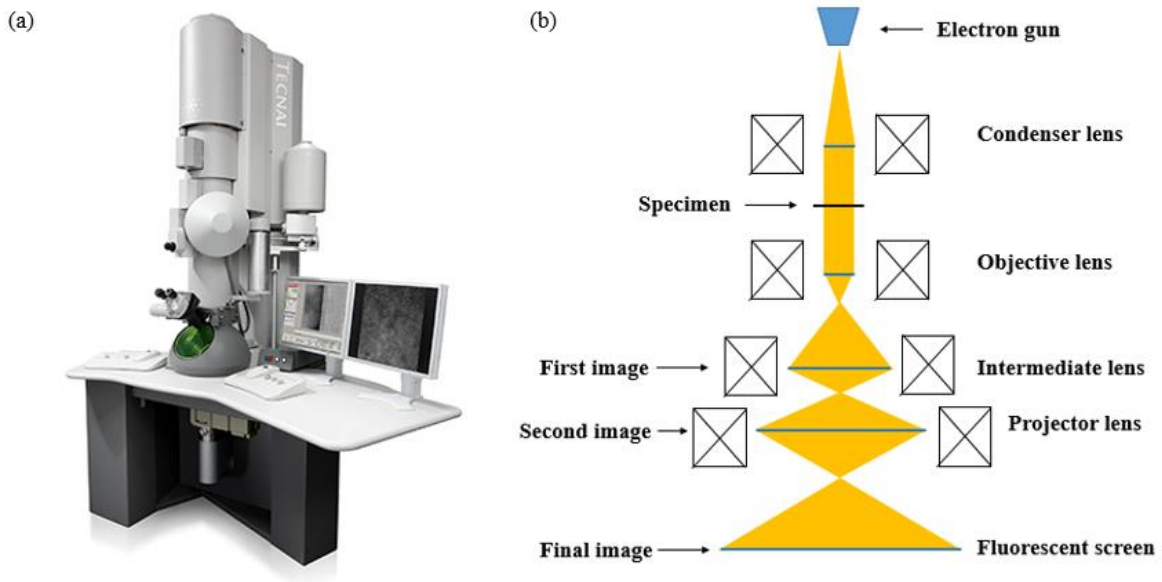

Figure 3.4 (a) Photography of Philips Tecnai F20 FEG-S/TEM. (b) General imaging system of TEM.

Chapter 4

Results and Discussions

4.1 Growth of binary $MoTe_2$

To study the growth and structure of $Mo_xW_{1-x}Te_2$, the corresponding binary structure of $MoTe_2$ and WTe_2 are provided for reference first. Figure 4.1 are the top-view and side-view crystal structures of 2H-$MoTe_2$ (Hexagonal, *P6₃/mmc*), 1T'-$MoTe_2$ (Monoclinic, *P2₁/m*), and T_d-WTe_2 (Orthorhombic, *Pnm2₁*), respectively.[4,48-50] As can be seen, they all have a layer structure with "…A-B-A-B…" stacking sequence, connected by Te-Te Van der Waal bond.[86] Each Mo (W) atom connects with six Te atoms, and each Te atom connects with three Mo (W) atoms. These atoms are in trigonal prismatic coordination for 2H polytype, while the atoms are in distorted octahedral coordination for 1T' and T_d polytype. Among these three structures, the 2H polytype can be easily distinguished from the other two as the lattice shows a hexagonal shape in *ab* plane, while the 1T' and T_d polytypes can be distinguished from each other in *ac* plane as the β of 1T' polytype is slightly larger than of T_d polytype. Different structures lead to different properties. As shown in Table 4.1, the 2H polytype is semiconducting with 1.0 eV indirect band gap in bulk and 1.1 eV direct band gap when the size decreases to monolayer.[87] The 1T' polytype is a conducting metal, while the T_d polytype is a semimetal with point contact between the conduction band and valence band.

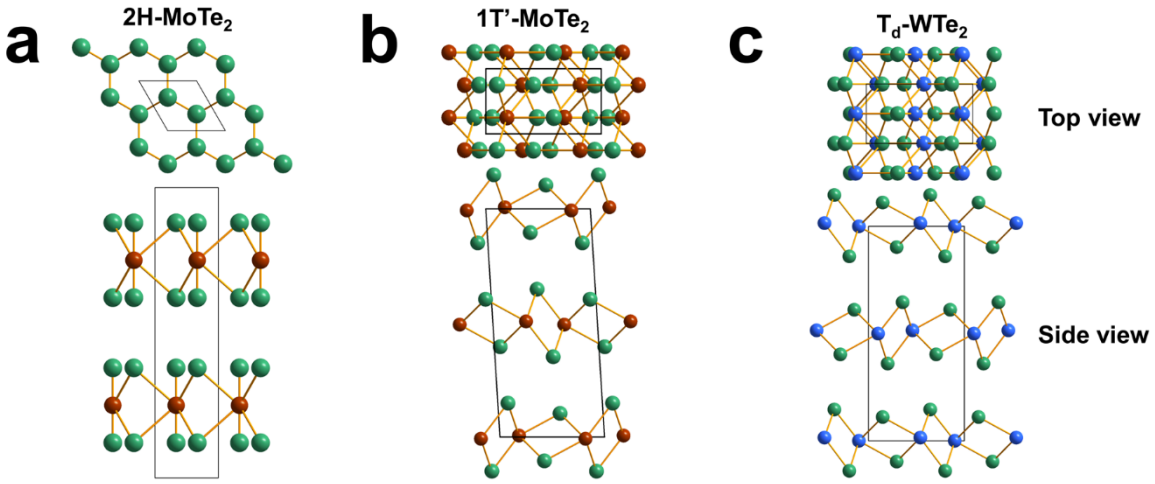

Figure 4.1. Top-view and side-view crystal structures of (a) 2H-$MoTe_2$, (b) 1T'-$MoTe_2$ and (c) T_d-WTe_2.

Table 4.1 Detailed crystal information of 2H-$MoTe_2$, 1T'-$MoTe_2$ and T_d-WTe_2.

Phase	Crystal structure	Lattice parameters	Electrical property
2H-$MoTe_2$	Hexagonal, *P6₃/mmc*	*a*=3.519 Å, b= 3.519 Å, *c*=13.964 Å	Semiconductor Band gap=0.9eV
1T'-$MoTe_2$	Monoclinic, *P21/m* (11)	*a*=6.330 Å, *b*=3.469 Å, *c*=13.86 Å, *β*=93º55'	Metal
T_d-WTe_2	Orthorhombic, *Pnm21* (31)	*a*=6.282 Å, *b*=3.496 Å, *c*=14.07 Å	Semimetal

In order to explore the CVD synthesis process of ternary $Mo_xW_{1-x}Te_2$ nanostructures, we started from the CVD synthesis of binary $MoTe_2$ nanostructures first. Figure 4.2 shows the simplified experimental setup with the precursors of MoO_3 and Te. Figure 4.3 (a) is the over-view SEM image of the as-grown $MoTe_2$ nanostructures, with two different areas labelled as 1 and 2. It is noted that the substrate was placed in a groove of a quartz substrate holder. Area 1 is mainly the pure Te particles while area 2 is the $MoTe_2$ nanobelts. The boundary between 1 and 2 areas is decided by the height of the groove.

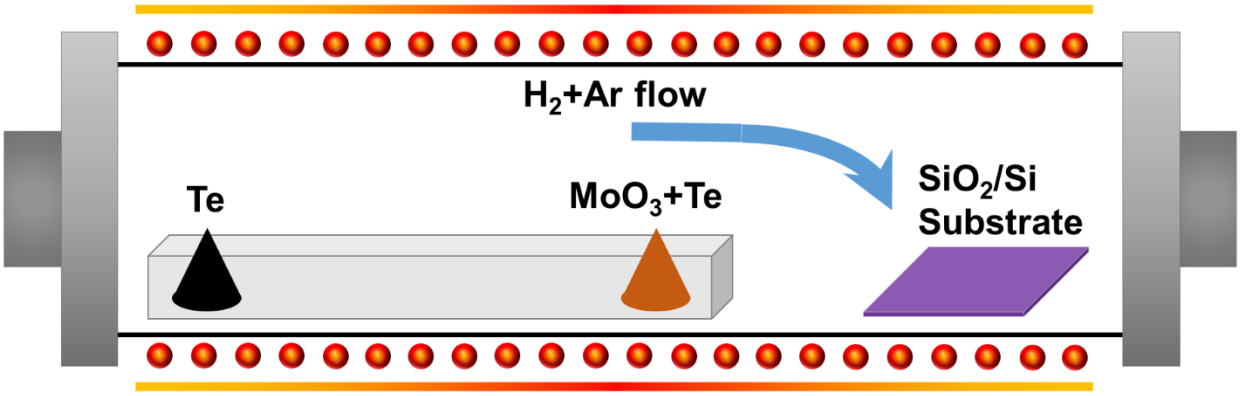

Figure 4.2 Schematic diagram of the CVD setup to grow binary $MoTe_2$.

This phenomenon can be observed in all the experiments, which is mainly because of the flow direction is changed in the groove and the concentration of precursors at area 2 is smaller than area 1 leading the formation of large-scale $MoTe_2$. Figure 4.3 (b) is a low-

magnification SEM image of $MoTe_2$ nanobelts, showing a high dispersibility. Figure 4.3 (c) is a middle-magnification SEM image, in which the $MoTe_2$ nanobelt with the width of ~1 μm and length up to tens of micrometers was clearly observed. Figure 4.3 (d) is the high-magnification SEM image with tilting angle of ~10°, in which the thickness of the nanobelt was measured to be ~100 nm. The synthesis of $MoTe_2$ nanobelts was found to be easy with MoO_3 and Te as the precursors.

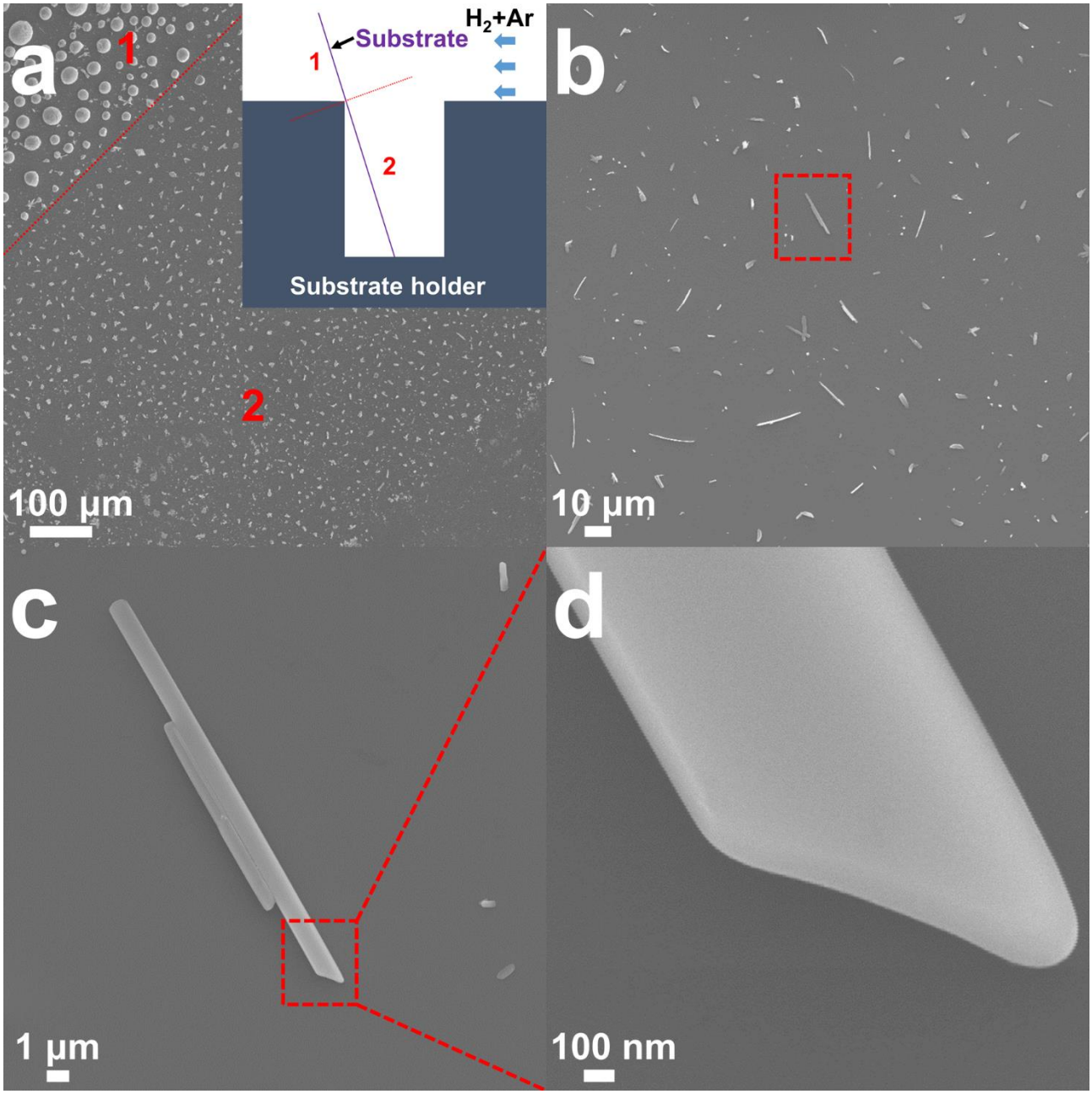

Figure 4.3 (a) Over-view SEM image, (b) low-magnification, (c) middle-magnification and (d) high-magnification SEM image of the as-grown $MoTe_2$ nanobelts. The inset in (a) shows that the substrate was placed in the groove of the substrate holder.

4.2 Growth of ternary $Mo_xW_{1-x}Te_2$

Based on the successful synthesis of binary $MoTe_2$, W precursors were added with Mo precursors to synthesize ternary $Mo_xW_{1-x}Te_2$. We have tried several types of W precursors, but only the mixed powders of WO_3+WCl_6+Te are feasible to synthesize ternary $Mo_xW_{1-x}Te_2$ as shown in Figure 4.4 (a). Figure 4.4 (b), (c) and (d) are the SEM image of the $Mo_xW_{1-x}Te_2$ nanobelts grown at 950 ^oC, 850 ^oC and 750 ^oC. It can be clearly observed that with decreasing temperature, the size and the density of the nanobelts are both decreasing. This is due to the reaction activity is lower with the decreasing temperature.

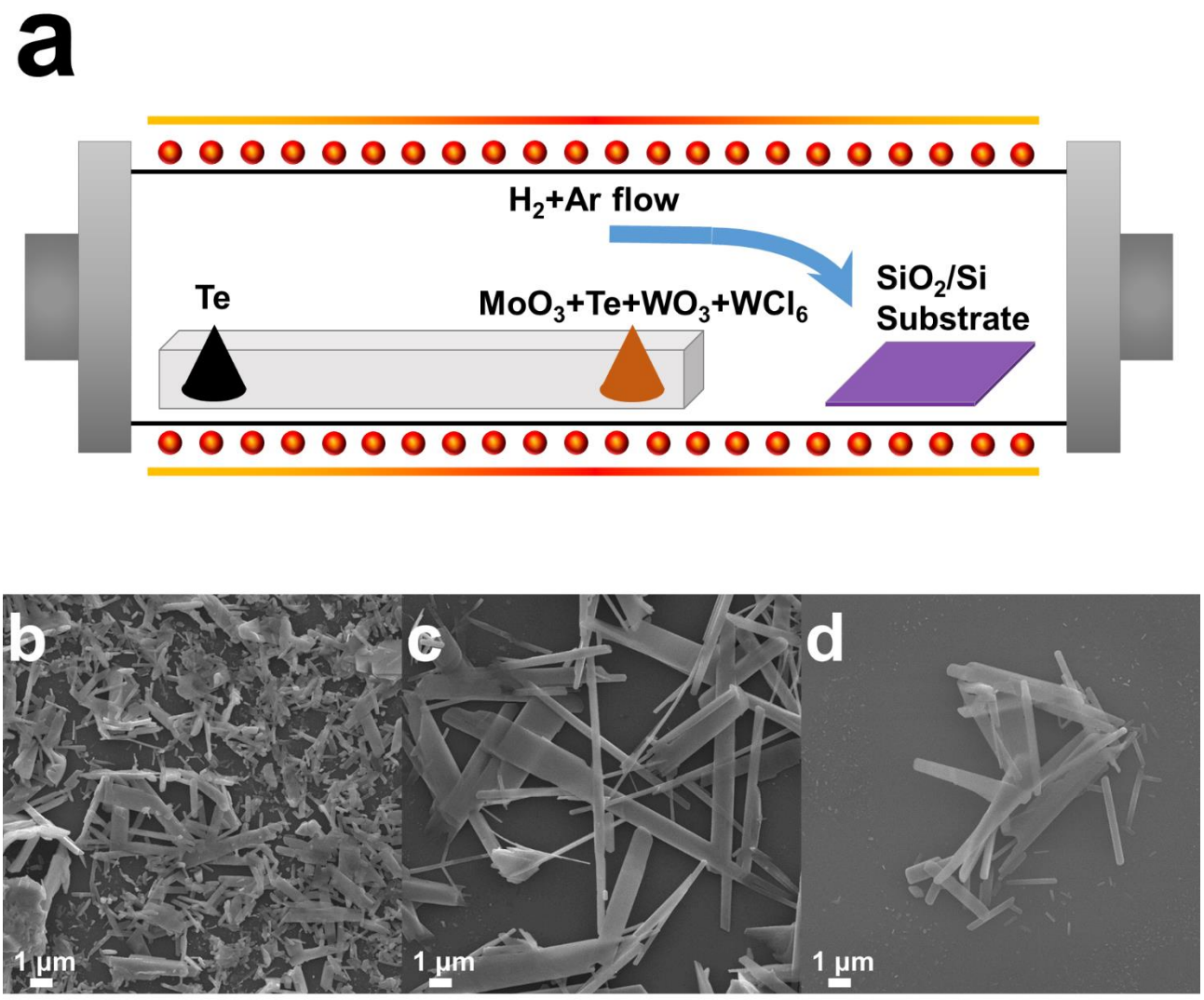

Figure 4.4 (a) Schematic diagram of the CVD setup to grow ternary $Mo_xW_{1-x}Te_2$. (b)-(d) SEM images of the $Mo_xW_{1-x}Te_2$ nanostructures grown at 950 ^oC, 850 ^oC and 750 ^oC.

Figure 4.5 is the schematic diagram of the experimental setup (tube furnace) for the $Mo_xW_{1-x}Te_2$ nanostructures growth. Both Mo precursors, W precursors and Te precursors were added into the reaction and 300 nm SiO_2/Si substrate were placed at about ~600 ^oC to collect the samples. Figure 4.6 (a) is the typical SEM image of the as-synthesized $Mo_xW_{1-x}Te_2$ nanostructures collected on the substrates and shows a “island” growth products with a high-density and large scale.[88] Figure 4.6 (b) is a high-magnification SEM image, in which rectangular nanobelts with width from 200 nm to 500 nm, and length up to tens of μm are clearly observed. To measure the thickness of the nanobelts, tilting SEM observation was carried out and the results are shown in Figure 4.6 (c) and 4.6 (d). As can be seen, the zoom-in SEM images shows a typical $Mo_xW_{1-x}Te_2$ nanobelt with a tilting angle of ~ 0^o and ~ 50^o. The thickness of the nanobelts can be estimated to be ~200 nm, and the side-facet shape is rectangle. The growth of the $Mo_xW_{1-x}Te_2$ nanostructures is reproducible and the fact of large-scale products reveals that the experimental condition is appropriate for the growth of $Mo_xW_{1-x}Te_2$ nanostructures. The $Mo_xW_{1-x}Te_2$ nanostructures grew in “island” shape corresponding to a unique growth mode called Volmer-Weber growth,[88] which is mainly decided by the wettability between the deposited atoms and the substrate as well as the diffusivity of the deposited atoms, which can be affected by the growth temperature and the growth time. However, it is also found that the Te in $Mo_xW_{1-x}Te_2$ would decompose after annealing at 350^{o}C, indicating the low thermal stability of $Mo_xW_{1-x}Te_2$.

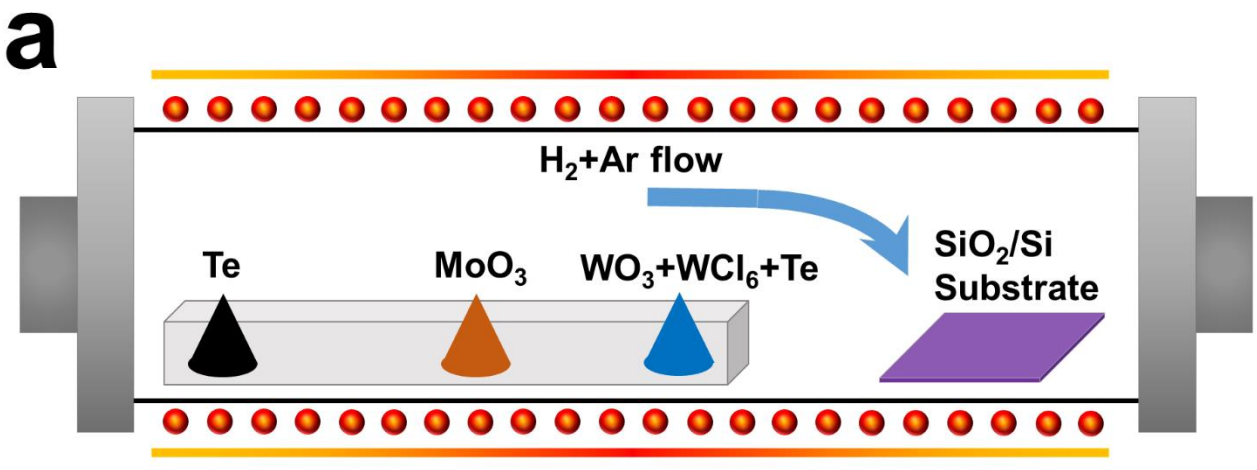

Figure 4.5 Schematic diagram of the CVD experimental setup to grow $Mo_xW_{1-x}Te_2$.

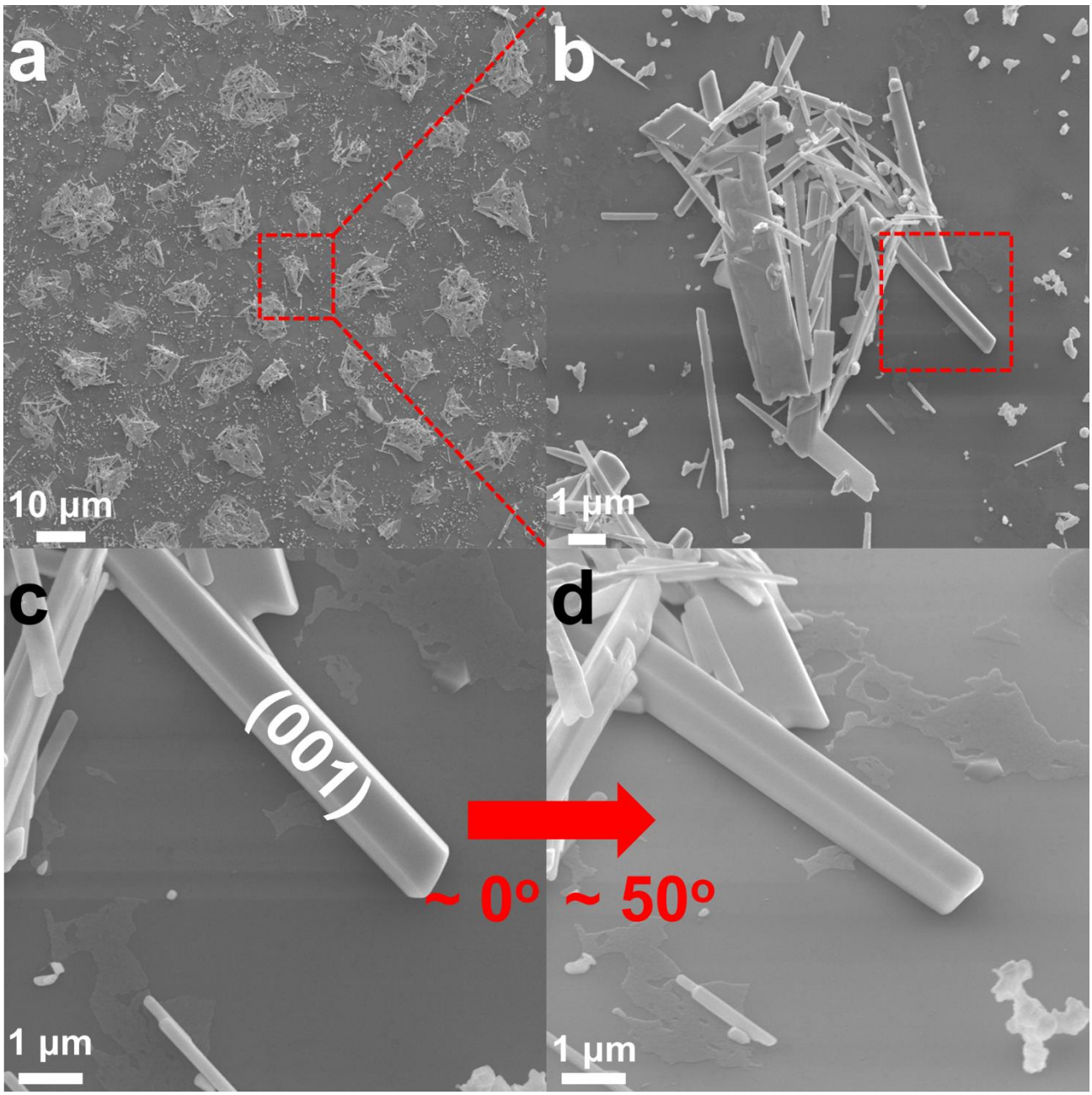

Figure 4.6 SEM images of as-grown $Mo_xW_{1-x}Te_2$ nanobelts. (a) Top-view low-magnification SEM image, (b) medium-magnification SEM image, (c) high-magnification SEM image with ~ 0° tilting and (d) high-magnification SEM image with ~ 50° tilting of the $Mo_xW_{1-x}Te_2$ nanobelts grown on the substrate.

Figure 4.7 (a) is a XRD pattern of the as-synthesised $Mo_xW_{1-x}Te_2$ nanobelts with all the peaks of (00*l*), revealing that the surface facet of the $Mo_xW_{1-x}Te_2$ nanobelts is {001}. Compared to the standard XRD peaks of (00*l*) of 2H-$MoTe_2$, 1T'-$MoTe_2$ and T_d-WTe_2 shown in Table 4.2, all the diffraction peaks of $Mo_xW_{1-x}Te_2$ nanobelts can be indexed to the standard structure of 1T'-$MoTe_2$ (Monoclinic phase, $P2_1/m$) with a = 6.330 Å, b = 3.649 Å, c = 13.86

Å, and β = 93°55'.[86,89] The strong peak near 70° can be indexed to the Si (400) from the substrate. Figure 4.7 (b) is a typical non-polarized Raman spectrum of the as-synthesised $Mo_xW_{1-x}Te_2$ nanobelts at room temperature. The standard Raman peaks of each phase are listed in Table 4.3. Several peaks can be clearly observed. The prominent peak at 258.2 cm^{-1} is a characteristic peak of 1T'-$MoTe_2$ relating to the vibration mode of Mo atoms, which can be assigned to the A_g mode of 1T'-$MoTe_2$.[26] Another three peaks at 109.6 cm^{-1} and 127.4 cm^{-1} and 161.6 cm^{-1} are relating to the vibration mode of Te atoms, which all agree to the A_g mode of 1T'-$MoTe_2$.[48,50] All the Raman peaks exhibit a slight red-shift, but the width and intensity are consistent with that of 1T'-$MoTe_2$.[4] It should be noted that a broad peak at ~210 cm^{-1} can be observed, which can be assigned to the A^2_1 mode of T_d-WTe_2 arisen from the vibrations of the W atoms, confirming the existence of W in the products.[43] Besides, the low intensity of the 210 cm^{-1} peak compared with the peak at 258.2 cm^{-1} shows that the vibrational intensity of W atoms is lower than Mo atoms, revealing that the content of W is relatively lower than the Mo. Moreover, the Raman characteristic peak of 1T'-$MoTe_2$ at 258.2 cm^{-1} is prominent, while the Raman characteristic peaks of 2H-$MoTe_2$ at 174 cm^{-1} (A_{1g} mode) and 234 cm^{-1} (E_{2g} mode) are absence and T_d-WTe_2 at 210 cm^{-1} (A^2_1 mode) is of low vibrational intensity, confirming the monoclinic structure of the as-synthesized products.[26]

Table 4.2 Standard XRD positions of (00*l*) peaks of 2H-$MoTe_2$, 1T'-$MoTe_2$ and T_d-WTe_2.

Phase	2θ (degree)				
	(002)	(004)	(006)	(008)	(0010)
2H-$MoTe_2$	12.668	25.494	38.656	52.375	66.958
1T'-$MoTe_2$	12.793	25.750	39.052	52.977	67.765
T_d-WTe_2	12.572	25.299	38.389	51.949	66.388

Table 4.3 Characteristic Raman peaks of 2H-$MoTe_2$, 1T'-$MoTe_2$ and T_d-WTe_2.

Phase	2H			1T'				T_d		
Mode	A^1_g	E^2_g	B^1_{2g}	A_g	B_g	A_g	A_g	A_1	A_1	A_1
Position (cm^{-1})	173	234	289	128	192	162	257	133	162	210

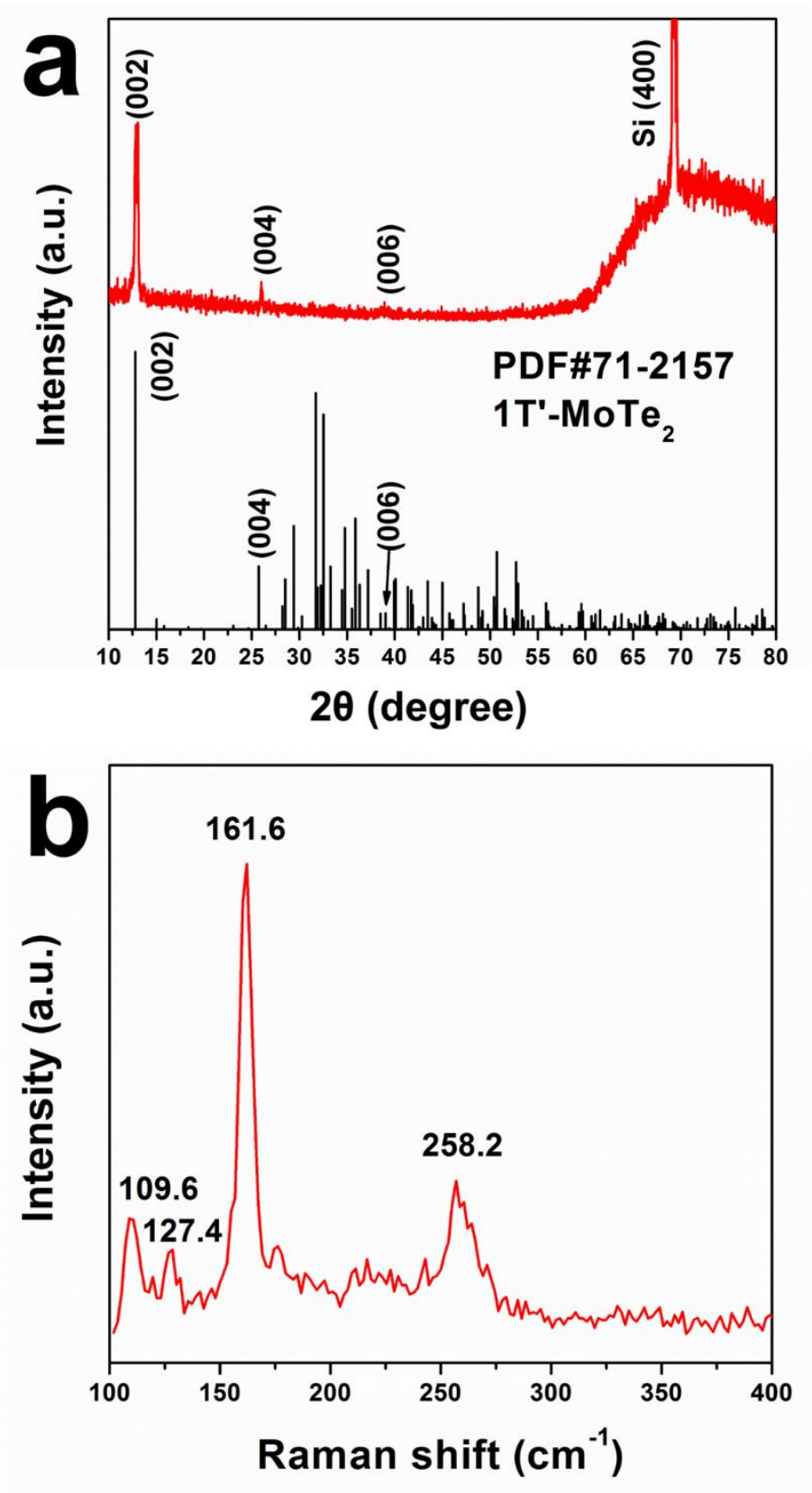

Figure 4.7 (a) XRD spectrum of the $Mo_xW_{1-x}Te_2$ nanobelts grown on the SiO_2/Si substrate. (b) Non-polarized Raman spectrum of the $Mo_xW_{1-x}Te_2$ nanobelts at room temperature.

In order to further understand the structural characteristics and chemical composition of such $Mo_xW_{1-x}Te_2$ nanobelts, detailed TEM characterizations were carried out. Figure 4.8 (a) is a bright-field (BF) TEM image of a typical $Mo_xW_{1-x}Te_2$ nanobelt, showing a uniform width of ~200 nm along the growth direction. Figure 4.8 (b) is the corresponding high-resolution (HR) TEM image, confirming that the product is high crystalline. The lattice spacing in HRTEM is measured as 0.381 nm, which is consistent with the *d*-spacing of monoclinic 1T'-$MoTe_2$ (200) plane, further confirming the monoclinic structure. The inset in Figure 4.8 (b) is the corresponding selected area electron diffraction (SAED) pattern, indicating that the surface normal is along [001], and the growth direction is along [100] by the comparison between the BFTEM image and SAED pattern. Figure 4.8 (c) is a EDS spectrum of the $Mo_xW_{1-x}Te_2$ nanobelt, showing that the nanobelt contains only Mo, W and Te, where the Cu signal was from the TEM grid. Besides, the ratio of Mo, W and Te is analysed to be 0.9: 0.1: 2. Therefore, the products can be called as $Mo_{0.9}W_{0.1}Te_2$ nanobelts.

In addition to the observations from *c*-axis, we also observed the lattice of $Mo_xW_{1-x}Te_2$ nanobelt along *b*-axis with TEM, in order to further verify the nature of monoclinic structure. As we mentioned above, the main difference between 1T' polytype and T_d polytype is the lattice shape in *ac* plane (the angle of β is different). However, to view from *b*-axis, the sample should tiled 90º, which is difficult to realize in TEM. Moreover, the thickness along *b*-axis is around 200 nm, which is quite large for TEM observation. Therefore, we used Focused Ion Beam (FIB) to cut the nanobelt to narrow the length along *b*-axis and rotated the nanobelt for 90º to make the (010) plane facing upward. Figure 4.9 (a) and (b) are the BFTEM image of the body and endpoint part of $Mo_xW_{1-x}Te_2$ single nanobelt, respectively. Figure 4.9 (c) is the SAED pattern of the $Mo_xW_{1-x}Te_2$ single nanobelt, showing a parallelogram shape. The ratio between two sides are around 2.11, which is similar with the ratio of *c*/*a*, revealing the long side is along [002] and the short side is along [200]. The angle of β here is measured to be around 103.85º, excluding the possibility of T_d polytype, which confirms the monoclinic structure of $Mo_xW_{1-x}Te_2$ nanobelt indirectly. The reason why the angle is not around the standard angle (93.55º) is that the electron beam is not adjusted to be parallel to *b*-axis strictly. The double image of the diffraction spot is mainly because of the surface of the nanobelt is asperous. Figure 4.9 (d) is the HRTEM image, showing a well crystalline structure. The d-spacing is measured to be around 0.691 nm, which is consistent with the d-spacing of (002).

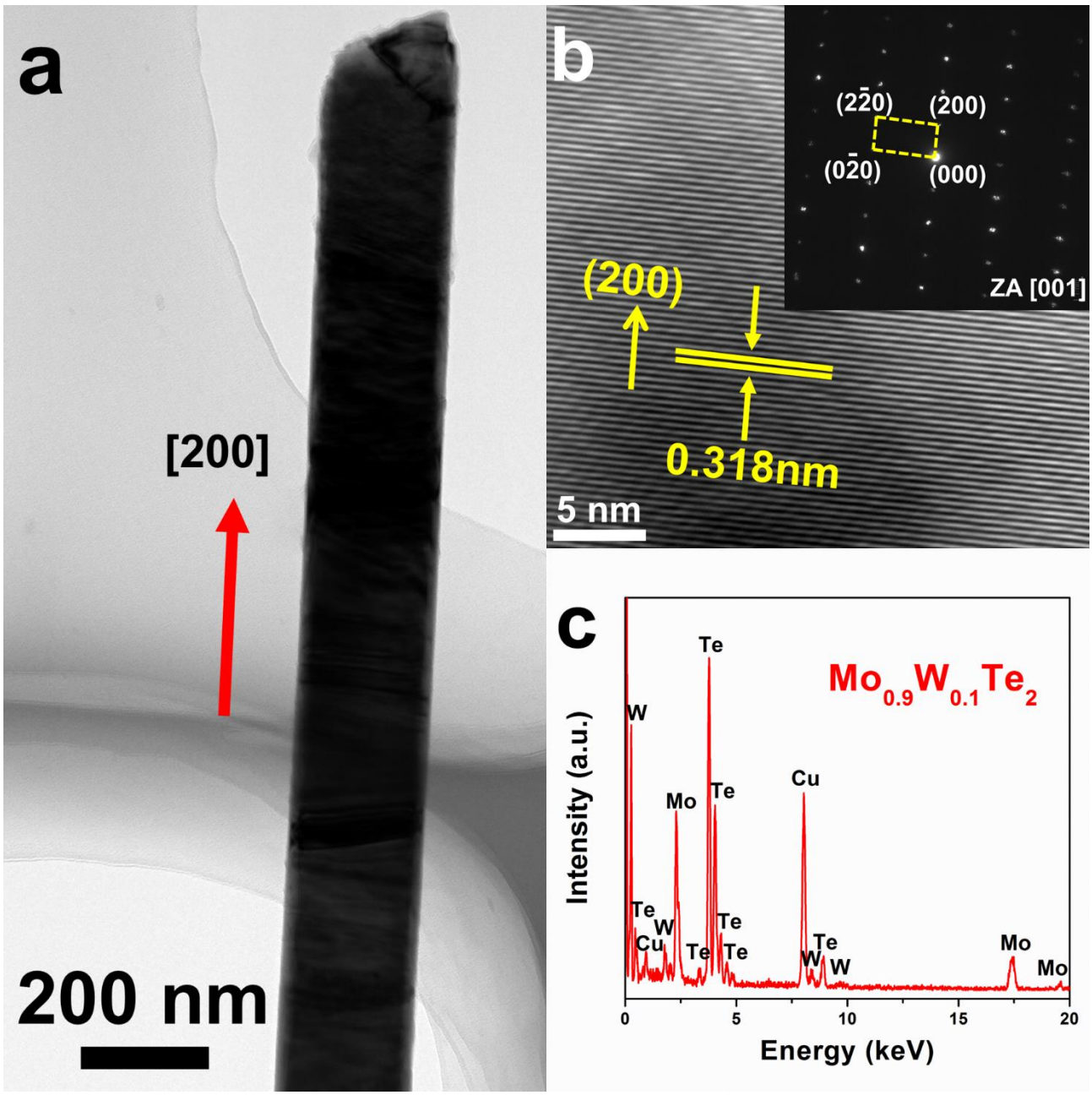

Figure 4.8 TEM images of the $Mo_xW_{1-x}Te_2$ nanobelt. (a) Low-magnification bright field TEM image of single nanobelt. (b) The corresponding HRTEM image. The inset is the SAED pattern. (c) EDS spectrum of the single nanobelt.

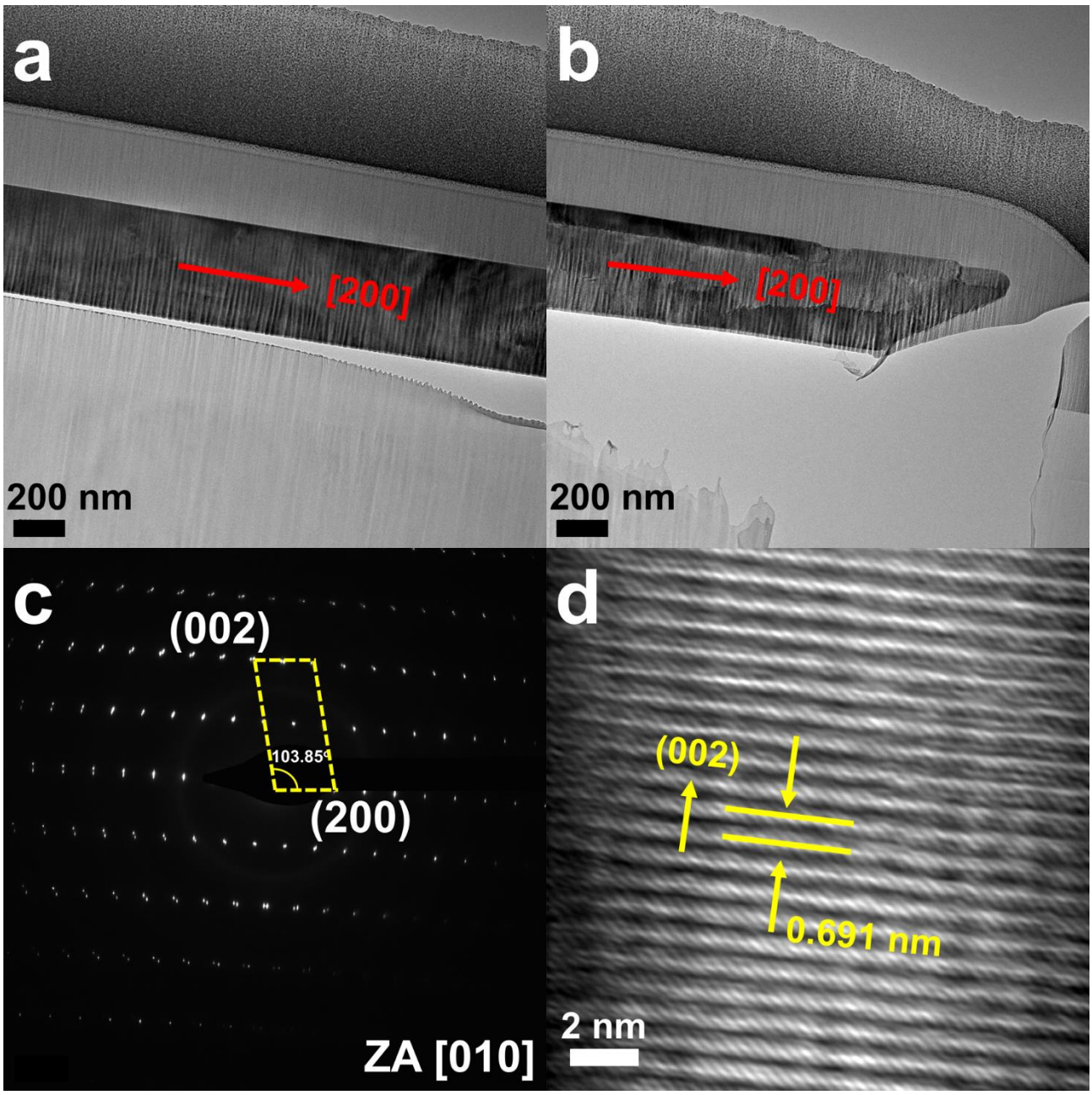

Figure 4.9 (a) and (b) are the BFTEM image of the body and the endpoint of the single $Mo_xW_{1-x}Te_2$ nanobelt. (c) SAED pattern of the $Mo_xW_{1-x}Te_2$ nanobelt. (d) HRTEM image of $Mo_xW_{1-x}Te_2$ nanobelt.

On the basis of the observations mentioned above, we propose a possible growth mechanism. In general, there are two proposed mechanisms for the growth of nanobelts, including the vapour-liquid-solid (VSL) and VS growth, respectively. As can be seen in our above characterizations, no catalysts were used in this work and no Te particles or other liquid-form particles can be observed at the two endpoints of the nanobelts, as the

surrounding nanoparticles of the $Mo_xW_{1-x}Te_2$ nanobelts were identified to be $Mo_xW_{1-x}Te_2$ by EDS, excluding the possibility of the self-catalyst VSL growth. Therefore, the VSL growth is not fitted for our work. Instead, the VS growth is likely to be the growth mechanism for our work. For a typical VS growth, the solid source were materials evaporated at high temperature, transported by the carrier gas, and deposited on the substrate at lower temperature. Based on the analysis above, we draw a schematic model to illustrate growth of $Mo_xW_{1-x}Te_2$ nanobelts as shown in Figure 4.10. In terms of VS growth, the W source, Mo source and Te source were evaporated during the temperature increasing to highest temperature. The alloyed $Mo_xW_{1-x}Te_2$ was formed under H_2 atmosphere during the transportation by carrier gas. The $Mo_xW_{1-x}Te_2$ vapour was then depostited on the substrate in the low-temperature area and formed the $Mo_xW_{1-x}Te_2$ clusters during the nucleation process. The $Mo_xW_{1-x}Te_2$ clusters then combined with each other based on crystallography arrangement and grew up to form such a nanobelt.

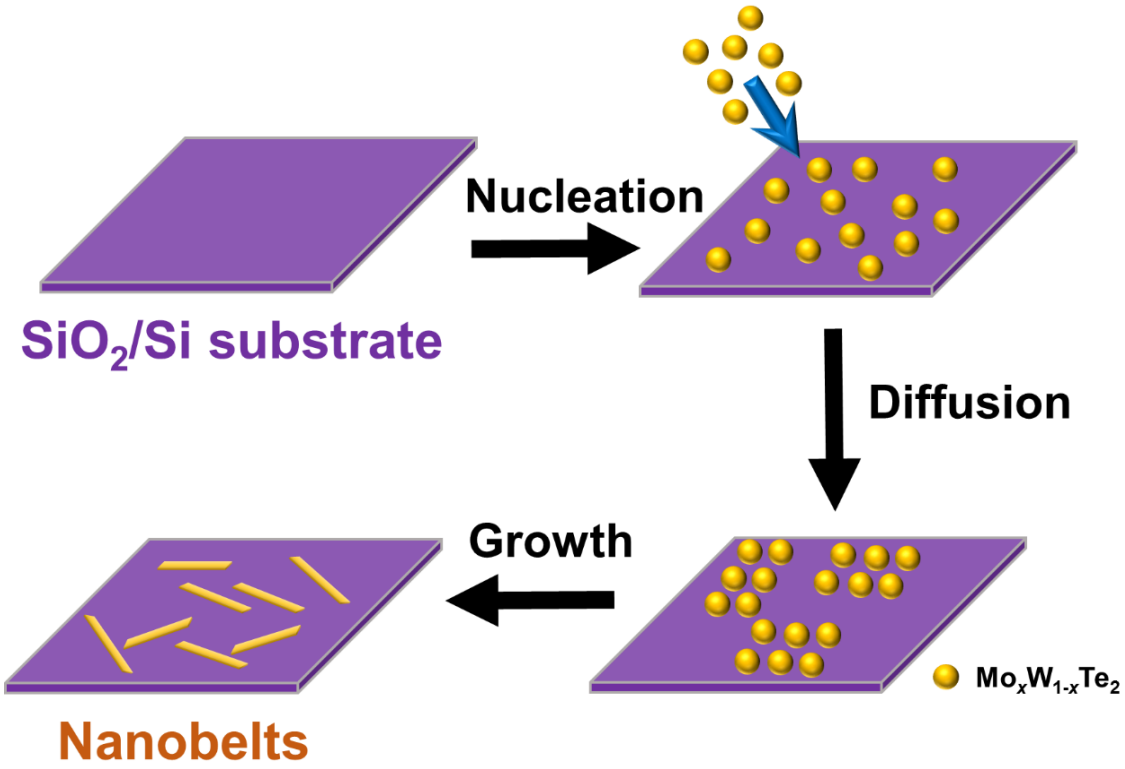

Figure 4.10 Schematic growth model of the $Mo_xW_{1-x}Te_2$ nanobelts.

To further understand formation of the ternary $Mo_xW_{1-x}Te_2$, whether it is W react with Te fisrt or Mo react with Mo first, we further study the synthesis of binary $MoTe_2$ and WTe_2 under

the same condition. Figure 4.11 (a) is the schematic diagram of the experimental setup for the WTe_2 nanostructures growth with the Te source at the upstream and W source at the centre. Figure 4.12 (a) is a SEM image of the as-synthesized WTe_2 nanostructures, showing a large scale of nanobelts in "island" shape, similar to the $Mo_xW_{1-x}Te_2$ nanobelts mentioned above. Figure 4.12 (b) is a medium-magnification SEM image, showing the WTe_2 nanobelts are of lower density compared with $Mo_xW_{1-x}Te_2$ nanobelts. The red dashed area, including stacking WTe_2 nanobelts and single WTe_2 nanobelt, was selected to do the EDS. Figure 4.12 (c) and (d) are the EDS spectrums of the stacking WTe_2 nanobelts and single WTe2 nanobelt, respectively, both showing the signals of W, Te, Si and O. The analysed atomic ratio between Si and O is around 1: 2, which is consistent with the composition of the SiO_2 substrate, the signals of Si and O are arisen from the substrate. As for the signals of W and Te, the analysed atomic ratio between W and Te is around 1: 2, revealing that the nanobelts have the composition of WTe_2. It has been noted that WTe_2 thin films could be synthesized by CVD using the mixed powders of WO_3, WCl_6 and Te under H_2 atmosphere at 820 ^oC:[18]

$$WO_3 + WCl_6 + Te + H_2 \rightarrow WTe_2 + H_2Te(g) + HCl(g) + H_2O(g) \quad (1)$$

Here, no WTe_2 thin films but WTe_2 nanobelts were obtained, which is probably due to the lower temperature. Figure 4.13 (a) is the BFTEM image of WTe_2 single nanobelt, showing a uniform width of ~200 nm. Figure 4.13 (b) is the corresponding SAED pattern, showing a rectangular shape, which is consistent with the reported results.[6,16] Furthermore, the growth direction is along [200], which is consistent with the ternary $Mo_xW_{1-x}Te_2$ nanobelts, revealing that this is a growth characteristic of both the WTe_2 and $Mo_xW_{1-x}Te_2$ nanobelts via CVD.

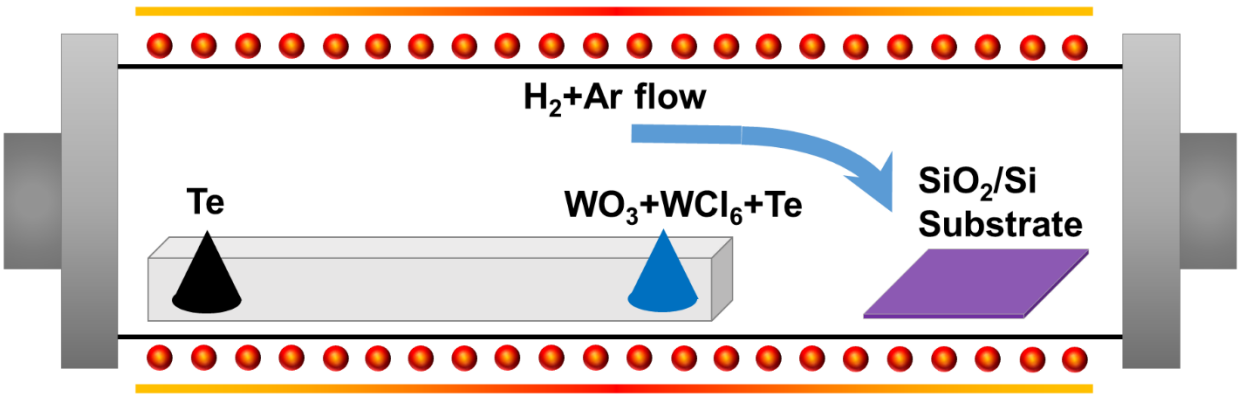

Figure 4.11 Schematic diagram of CVD experimental setup for the binary WTe_2 growth with W and Te precursors.

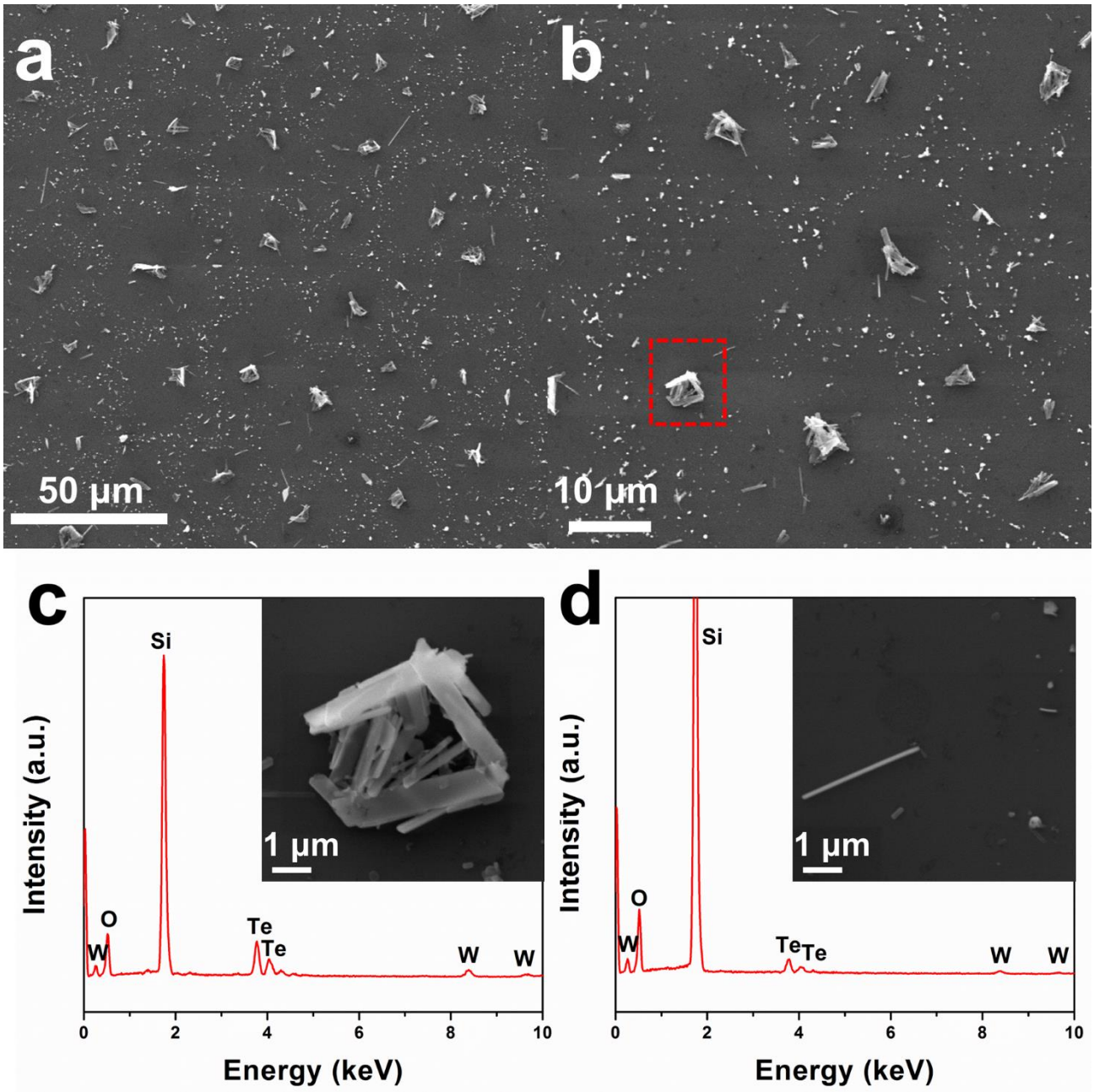

Figure 4.12 SEM images of the as-grown WTe_2 nanobelts. (a) Over-view SEM image and (b) low-magnification SEM image of WTe_2 nanobelts. The red dashed area in (b) is selected to do the EDS. (c) and (d) EDS spectrum of the stacking WTe_2 nanobelts and single nanobelt. The inset in (c) and (d) are the high-magnification SEM image of the EDS target.

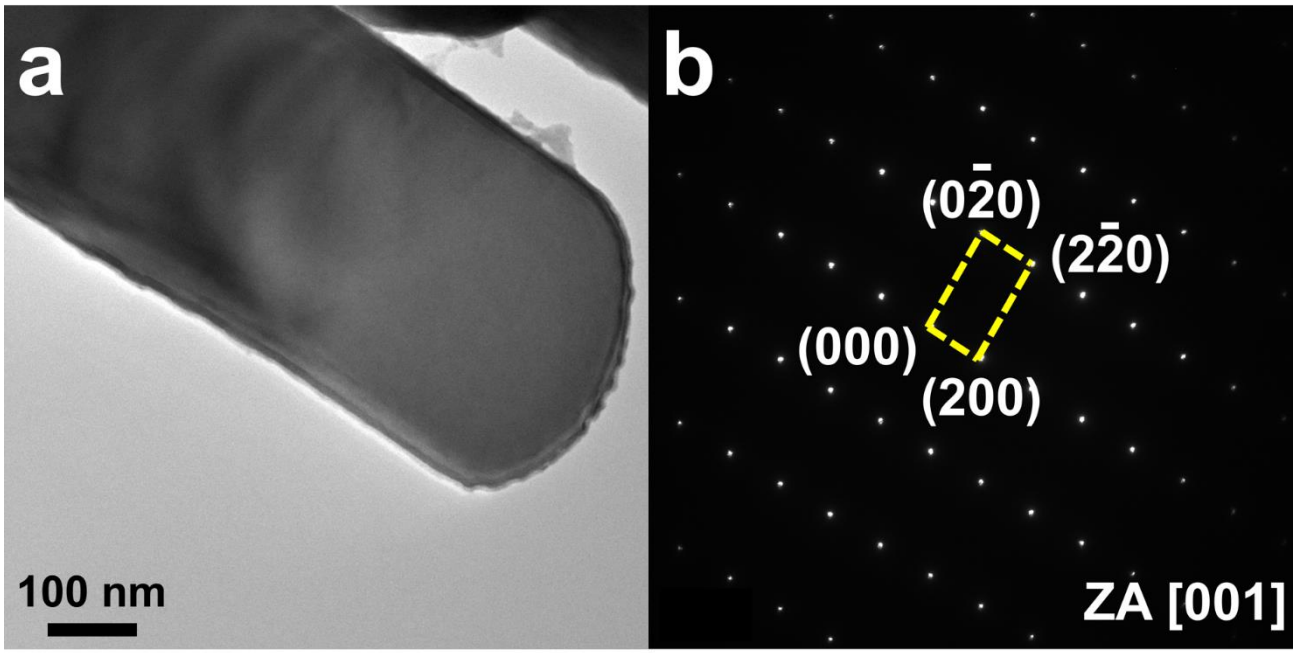

Figure 4.13 (a) Bright-field TEM image of the typical single $Mo_xW_{1-x}Te_2$ nanobelt. (b) SAED pattern of the single $Mo_xW_{1-x}Te_2$ nanobelt.

On the other hand, we kept the Mo source and Te source, while remove the W source to study the synthesis of binary $MoTe_2$ nanostructures as shown in Figure 4.14. Figure 4.15 (a) is a SEM image of the nanostructures grown with the addition of Mo source and Te source, showing a large-scale and high-density of nanobelts, which is quite different from the growth of WTe_2 and $Mo_xW_{1-x}Te_2$ nanobelts mentioned above. Firstly, no $MoTe_2$ was obtained. As can be seen in Figure 4.15 (b), the corresponding EDS spectrum shows only the signals of Mo, Si and O without Te. After analysis, the Si and O are arisen from the SiO_2 substrate, which is similar to Figure 4.15 (c) and (d), indicating that the nanobelts are pure Mo. However, when we further add Te powders into the Mo source, it is found that $MoTe_2$ nanobelts can be obtained, indicating the Te concentration is significant for the growth of $MoTe_2$, which is not only used to lower the melting point of MoO_3 but also used to increase the Te concentration in the tube. The final products are pure Mo instead of MoO_3 can be explained by the reaction that H_2 can reduce MoO_3 into pure Mo above 650 ^oC:[90]

$$MoO_3 + 3H_2 \rightarrow Mo + 3H_2O \quad (2)$$

Therefore, the comparison between Figure 4.6, Figure 4.12 and Figure 4.15 reveals that the sequence of $Mo_xW_{1-x}Te_2$ is that W reacted with Te first in this work, which is due to the extra addition of WCl_6 and Te powders to the WO_3, compared with MoO_3.

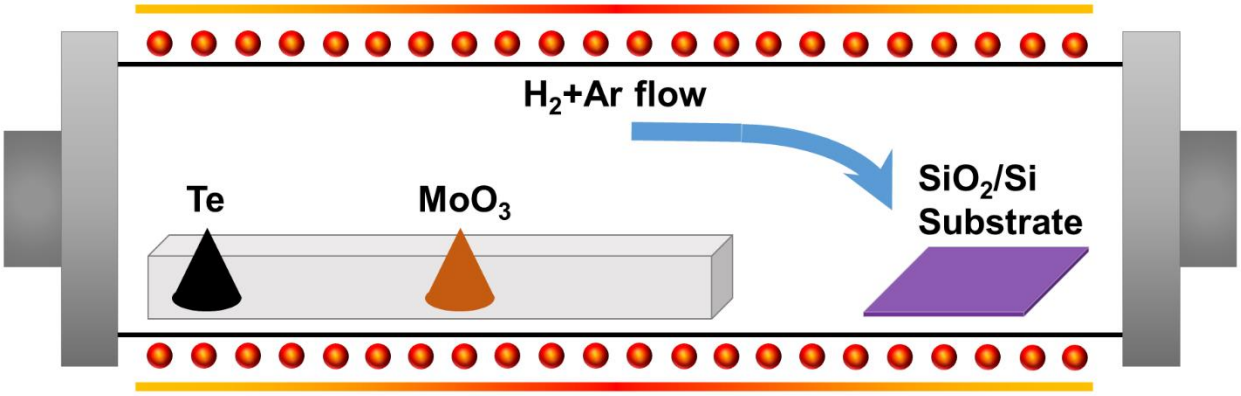

Figure 4.14 Schematic diagram of CVD experimental setup for the growth of $MoTe_2$ with Mo source and Te source.

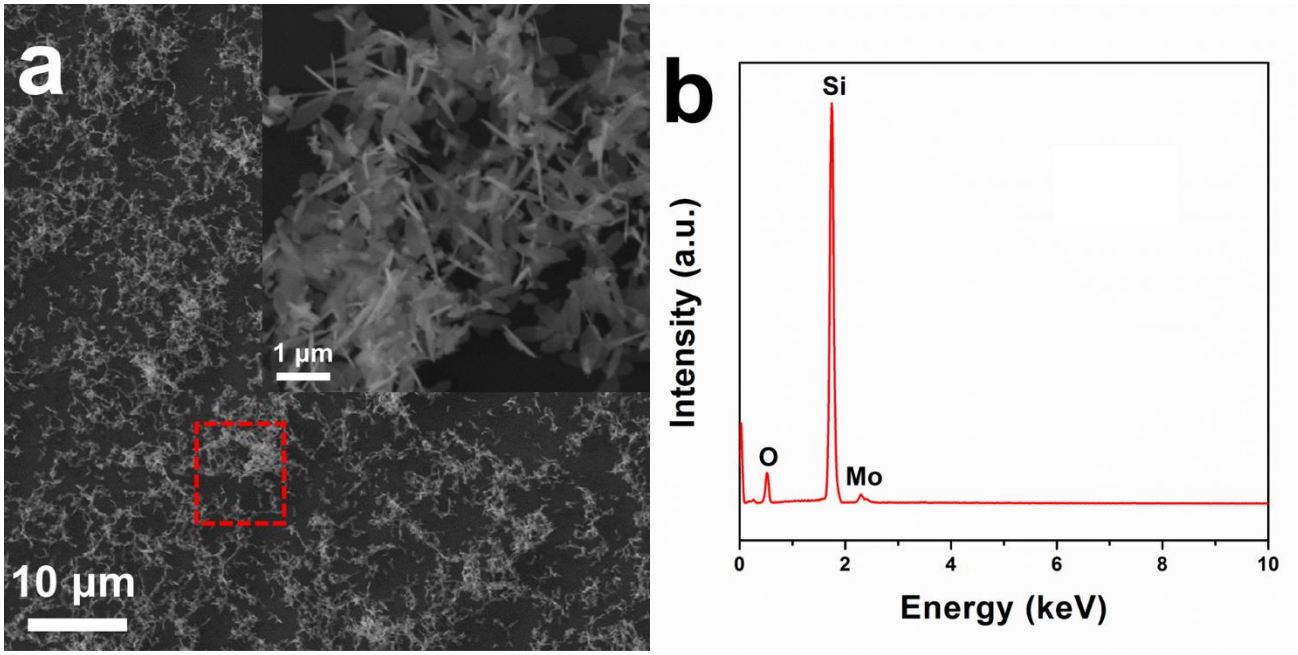

Figure 4.15 (a) The corresponding SEM image of the products in Figure 4.14. The inset in (a) is the high magnification SEM image of the typical nanostructure marked by red dashed box. (b) The corresponding EDS spectrum of (a).

Based on the analysis mentioned above that H_2 has play an important role in the growth of $Mo_xW_{1-x}Te_2$ nanobelts, we designed an experiment to study impact of the H_2 atmosphere in this work. Figure 4.16 is the schematic diagram of the experimental setup to study the impact of H_2, where the H_2 gas was removed and the other growth condition remains the same. Figure 4.17 (a) is a typical SEM image of the samples grown without H_2, showing a large-scale and high-density of round particles with a radius from 100 nm to 20 μm. Figure 4.17 (b) is the corresponding EDS spectrum of the particles, showing the peaks of Mo, W, Te, Si and O. It is noted that the signal of O is relatively higher than Si, which is different from the EDS spectrum mentioned above. After the compositional analysis, the atomic ratio of O is higher than Si, while the (Mo+W): Te is around 1:4, revealing that the composition is not $Mo_xW_{1-x}Te_2$ but with O in it. This observation indicates that the H_2 gas in the growth of $Mo_xW_{1-x}Te_2$ nanobelts not only acted as the carrier gas but also prevent the samples being oxidized, revealing the significance influence of H_2 to the growth of ternary $Mo_xW_{1-x}Te_2$ nanobelts.

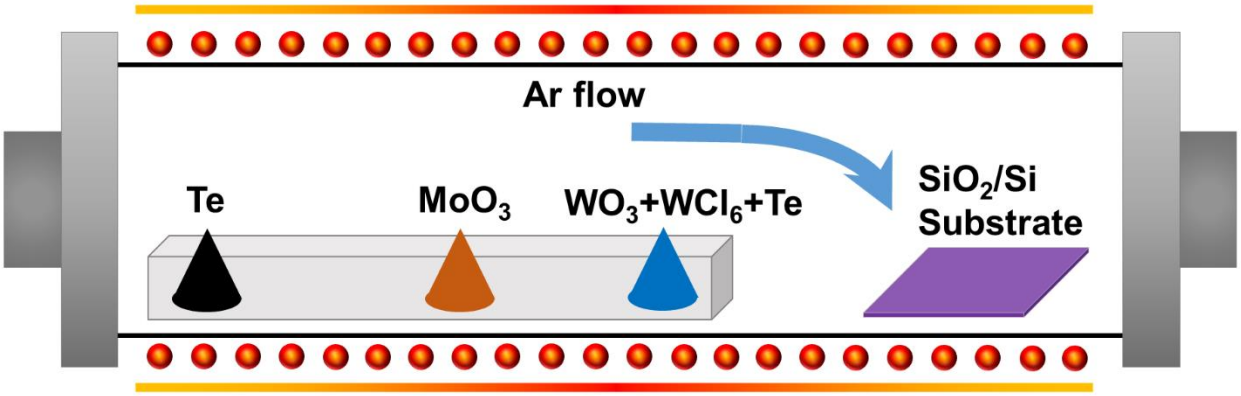

Figure 4.16 Schematic diagram of CVD experimental setup for the growth of $Mo_xW_{1-x}Te_2$ without the induction of H_2.

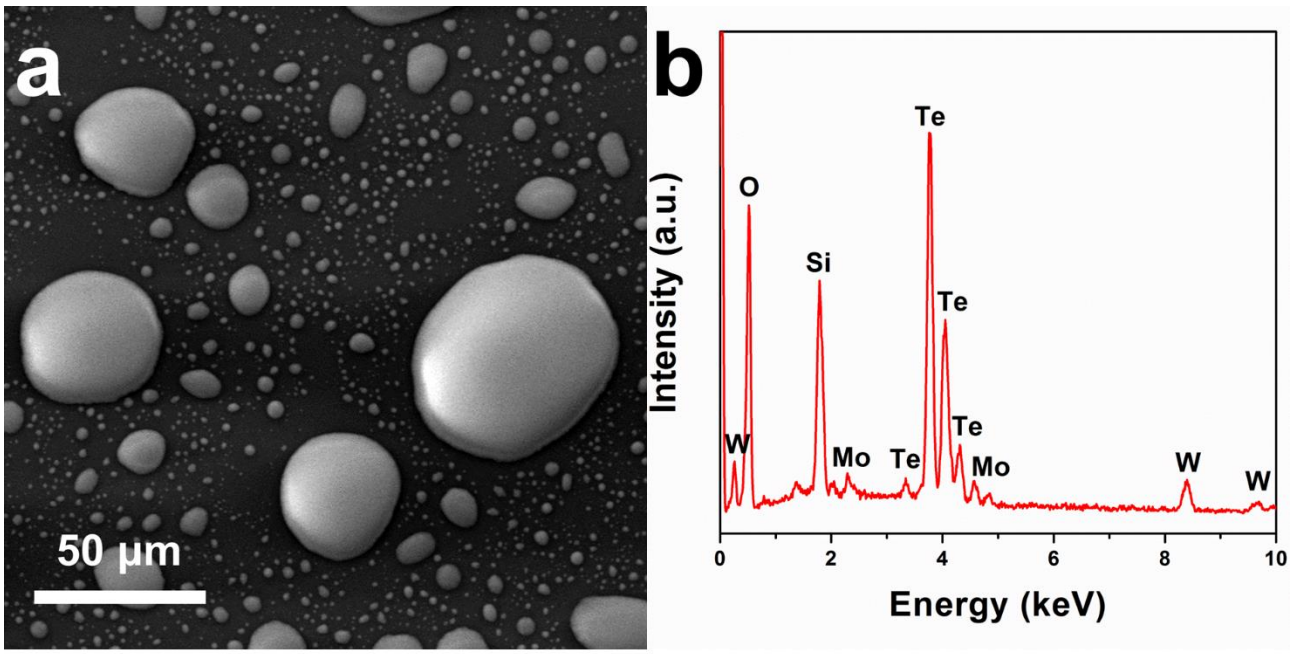

Figure 4.17 (a) The corresponding SEM image of the products in Figure 4.16. (b) The corresponding EDS spectrum of (a).

On the basis of the $Mo_xW_{1-x}Te_2$ nanobelts growth, we further study the impact of the growth time to the morphology of the nanobelts. Figure 4.18 (a) is an over-view SEM image of the $Mo_xW_{1-x}Te_2$ nanobelts grown in 60 min. It can be observed that the products are of lower density comparing with the 120 min's growth. Figure 4.18 (b) is a high-magnification SEM image of the $Mo_xW_{1-x}Te_2$ nanobelts grown in 60 min, showing that the nanobelt has a width down to 100 nm with a length up to tens of micrometres. Figure 4.19 (a) is an over-view SEM image of the $Mo_xW_{1-x}Te_2$ nanobelts grown in 10 min. $Mo_xW_{1-x}Te_2$ nanobelts with much lower density and no stacking nanobetls were observed. Figure 4.19 (b) is a high-magnification SEM image of the $Mo_xW_{1-x}Te_2$ nanobelts grown in 10 min, showing that the nanobelt has a width of ~500 nm and the length of ~8 μm. The comparison between Figure 4.6 (b), Figure 4.18 (a) and Figure 4.19 (a) indicates that the morphology of the products are similar, but the density of the products is lower and lower with the decreasing growth time. The comparison between Figure 4.6 (c), Figure 4.18 (b) and Figure 4.19 (b) indicates that the size of the nanobelts does not change significantly under different growth time.

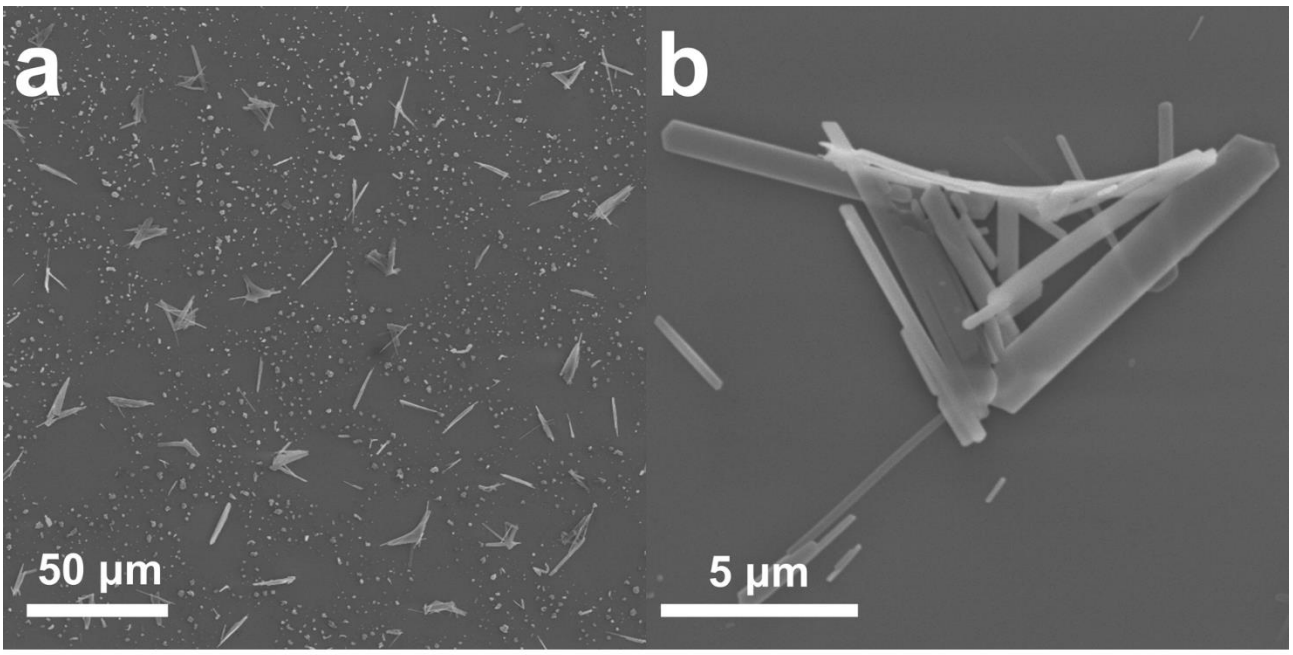

Figure 4.18 (a) and (b) are the over-view and high-magnification SEM image of the $Mo_xW_{1-x}Te_2$ nanobelts grown in 60 min.

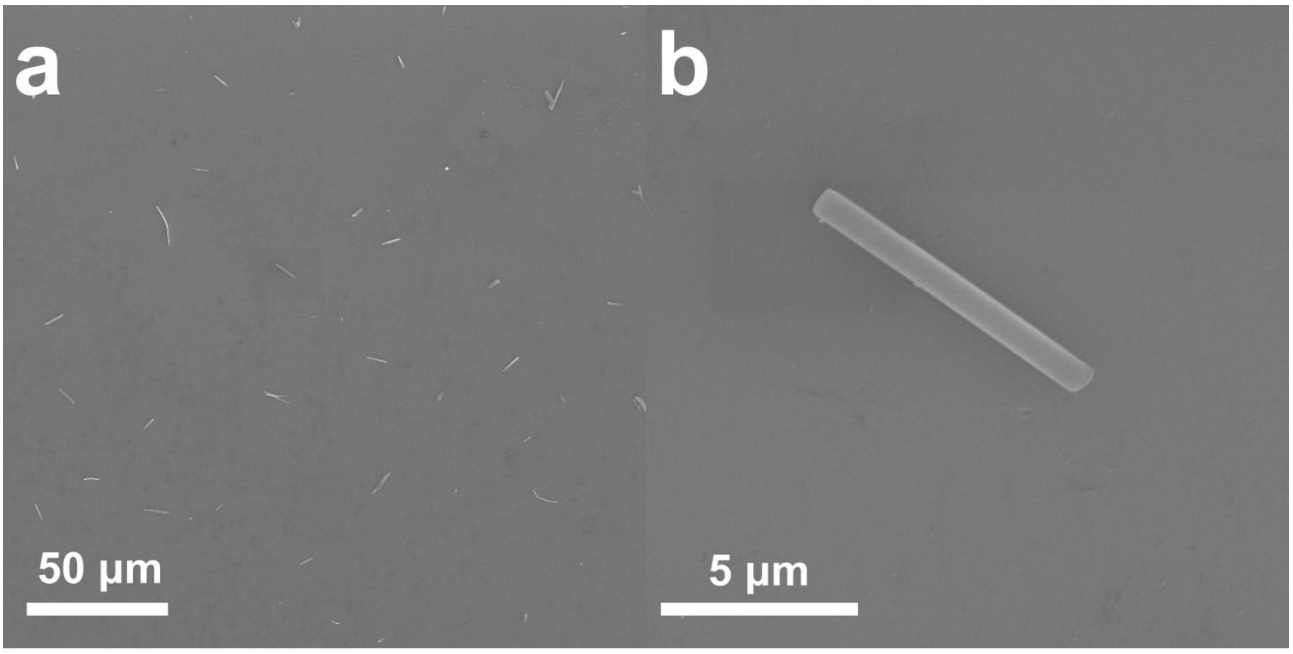

Figure 4.19 (a) and (b) are the over-view and high-magnification SEM image of the $Mo_xW_{1-x}Te_2$ nanobelts grown in 10 min.

This Chapter 4 has been prepared for a first-author manuscript, which is going to submit to the “Journal of the Crystal Growth”. In addition, another co-author manuscript has been submitted to “small journal”.

4.3 Conclusion

In this study, we first grew ternary $MoTe_2$ nanostructures with a facile and catalyst-free CVD process. The morphology of $MoTe_2$ was found to be both rectangular and hexagonal, which is consistent with its 1T' polytype and 2H polytype, respectively. The thermal stability of $MoTe_2$ was found to be low, as the concentration of Te was found to be lower than Mo after annealing at 350 ^oC. Based on the facile and catalyst-free CVD growth of $MoTe_2$ nanomaterials, the W precursors was added into the process and we successfully realized the alloying of Mo, W and Te into ternary $Mo_xW_{1-x}Te_2$ nanomaterials by CVD. The W was found to alloy with Mo and Te successfully under certain condition.. The morphology of $Mo_xW_{1-x}Te_2$ nanomaterials were in rectangular belt, similar with the morphology of 1T'-$MoTe_2$. The growth direction was found to be [100] and the surface facet was {002}. The chemical composition was determined to be $Mo_{0.9}W_{0.1}Te_2$. We also proposed VS mechanism to explain the growth of $Mo_xW_{1-x}Te_2$ nanobelts. Besides, the H_2 was found to have a significant impact in the growth of $Mo_xW_{1-x}Te_2$ nanobelts, which prevented the samples being oxidization. The density of the $Mo_xW_{1-x}Te_2$ nanobelts is decreasing with the decreasing growth temperature and growth time. This work opens a new window to synthesize the nano-size $Mo_xW_{1-x}Te_2$ and provides the opportunity to study the nanostructure engineering of $Mo_xW_{1-x}Te_2$. Furthermore, this work pave the way for future nanostructure study of other ternary system in TMDs.

Chapter 5
Conclusions and outlook

5.1 Conclusions

As an ideal candidate for applications in phase change memory and topological Weyl semimetals, transition metal dichalcogenides (TMDs) MTe_2 (M= Mo, W) has been the most popular material system in the condensed state physics and material science. Among them, $MoTe_2$ and WTe_2 have a unique line-shape Fermi surface and two separated Weyl nodes with opposite chirality in the momentum space, leading to novel physical properties, such as magnetoresistance effect and superconductivity. Furthermore, through alloying engineering, ternary material $Mo_xW_{1-x}Te_2$ can also realize the topological Weyl semimetalic state and tune the distance between two Weyl nodes by the content of Mo, which can increase the topological strength of the system and thus increase its practicability. Therefore, the realization of alloying $Mo_xW_{1-x}Te_2$, even at nano size, is very attracting.

A few studies have shown that the Mo content can tune the structure of bulk $Mo_xW_{1-x}Te_2$ between semiconductor, metal and semimetal via chemical vapour transport (CVT). In fact, it is well known that the TMDs show exotic properties when size is reduced from bulk to nanomaterial. However, the studies of the $Mo_xW_{1-x}Te_2$ nanomaterials are rare. Therefore, it is urgent to fast synthesize the $Mo_xW_{1-x}Te_2$ nanomaterials to expand the research on $Mo_xW_{1-x}Te_2$.

Chemical vapour deposition (CVD) is a commonly used method for the synthesis of semiconductor nanomaterial. Extensive studies have shown that the binary $MoTe_2$ and WTe_2 nanomaterials can be synthesized via CVD with a simple and fast synthesis process. In general, two kinds of CVD methods, including two-step CVD and one-step CVD, are used. For the two-step CVD, Mo (W) precursor is deposited onto the substrate prior to the growth. Te precursor further reacts with Mo (W) precursor on the substrate after evaporation, transportation, and deposition. For one-step CVD, Mo (W) and Te precursors are both evaporated during the heating, transported by carrier gas, deposited on the substrate, and reacting with each other finally. Both two-step and one-step CVD are of short growth time down to 5 min. Therefore, we proposed to use CVD to synthesize $Mo_xW_{1-x}Te_2$ nanomaterials with a fast and simple process.

In this thesis, large-scale $Mo_{0.9}W_{0.1}Te_2$ monoclinic nanobelts were successfully synthesized on SiO_2/Si substrate via a fast and simple CVD route for the first time. Based on the structural and chemical characteristics, the surface facet of the nanobelts is {002} and the growth direction is along [100] with thickness of 50-200 nm and length up to tens of μm. A VS model is proposed to describe the growth of $Mo_xW_{1-x}Te_2$ nanobelts. Besides, we also study the synthesis of the corresponding binary $MoTe_2$ and WTe_2 nanostructures and reveals the formation sequence of Mo and W with Te. Furthermore, the impact of the H_2 and growth time were demonstrated. This study demonstrates a fast and simple synthesis method for $Mo_xW_{1-x}Te_2$ nanomaterial, and provides a new perspective to develop the unique topological properties of $Mo_xW_{1-x}Te_2$ nanomaterials for future electronic and spintronic devices.

5.2 Outlook

In the future, the study of the CVD synthesis of the $Mo_xW_{1-x}Te_2$ nanostructure can be separated into three steps: Firstly, we need to understand the impact of each growth parameters to the $Mo_xW_{1-x}Te_2$ nanomaterials growth comprehensively. Secondly, we need to optimize the growth parameters of the $Mo_xW_{1-x}Te_2$ nanomaterials to grow a more homogeneous and separated products. Thirdly, we should be able to control the composition of $Mo_xW_{1-x}Te_2$ nanostructure, so that the further tunable structure and properties by Mo content could be studied.

Chapter 6

References

1 H.B. NIelsen & Ninomiya, M. Absence of neutrinos on a lattice Proof by homotopy theory. *Nuclear Physics* **1981**, B185, 20-40.

2 Sun, Y., Wu, S.-C., Ali, M. N., Felser, C. & Yan, B. Prediction of Weyl semimetal in orthorhombic $MoTe_2$. *Phys. Rev. B* **2015**, 92.

3 Soluyanov, A. A., Gresch, D. *et al.* Type-II Weyl semimetals. *Nature* **2015**, 527, 495-498.

4 Rhodes, D., Chenet, D. A. *et al.* Engineering the Structural and Electronic Phases of $MoTe_2$ through W Substitution. *Nano Lett.* **2017**, 17, 1616-1622.

5 Han, G. H., Keum, D. H. *et al.* Absorption dichroism of monolayer 1T′-$MoTe_2$ in visible range. *2D Materials* **2016**, 3, 031010.

6 Zhou, Y., Jang, H. *et al.* Direct Synthesis of Large-Scale WTe_2 Thin Films with Low Thermal Conductivity. *Adv. Funct. Mater.* **2017**, 27, 1605928.

7 Chen, S. Y., Naylor, C. H., Goldstein, T., Johnson, A. T. & Yan, J. Intrinsic Phonon Bands in High-Quality Monolayer T' Molybdenum Ditelluride. *ACS Nano* **2017**, 11, 814-820.

8 Cheng, S., Yang, L. *et al.* Large area, phase-controlled growth of few-layer, two-dimensional $MoTe_2$ and lateral 1T′–2H heterostructures by chemical vapor deposition. *CrystEngComm.* **2017**, 19, 1045-1051.

9 Naylor, C. H., Parkin, W. M. *et al.* Large-area synthesis of high-quality monolayer 1T'-WTe_2 flakes. *2D Mater.* **2017**, 4, 021008.

10 Zhou, L., Xu, K. *et al.* Large-Area Synthesis of High-Quality Uniform Few-Layer $MoTe_2$. *J. Am. Chem. Soc.* **2015**, 137, 11892-11895.

11 Naylor, C. H., Parkin, W. M. *et al.* Monolayer Single-Crystal 1T'-$MoTe_2$ Grown by Chemical Vapor Deposition Exhibits Weak Antilocalization Effect. *Nano Lett.* **2016**, 16, 4297-4304.

12 Kim, S., Kim, J. H. *et al.* Post-patterning of an electronic homojunction in atomically thin monoclinic $MoTe_2$. *2D Mater.* **2017**, 4, 024004.

13 Zhou, L., Xu, K. *et al.* Role of Molecular Sieves in the CVD Synthesis of Large-Area 2D $MoTe_2$. *Adv. Funct. Mater.* **2017**, 27, 1603491.

14 Zhou, L., Zubair, A. *et al.* Synthesis of High-Quality Large-Area Homogenous 1T' $MoTe_2$ from Chemical Vapor Deposition. *Adv. Mater.* **2016**, 28, 9526-9531.

15 Yang, L., Zhang, W. *et al.* Tellurization Velocity-Dependent Metallic-Semiconducting-Metallic Phase Evolution in Chemical Vapor Deposition Growth of Large-Area, Few-Layer $MoTe_2$. *ACS Nano* **2017**, 11, 1964-1972.

16 Zhang, E., Chen, R. *et al.* Tunable Positive to Negative Magnetoresistance in Atomically Thin WTe_2. *Nano Lett.* **2017**, 17, 878-885.

17 Empante, T. A., Zhou, Y. *et al.* Chemical Vapor Deposition Growth of Few-Layer $MoTe_2$ in the 2H, 1T', and 1T Phases: Tunable Properties of $MoTe_2$ Films. *ACS Nano* **2017**, 11, 900-905.

18 Zhou, J., Liu, F. *et al.* Large-Area and High-Quality 2D Transition Metal Telluride. *Adv. Mater.* **2017**, 29.

19 Liu, H. F., Wong, S. L. & Chi, D. Z. CVD Growth of MoS_2-based Two-dimensional Materials. *Chemical Vapor Deposition* **2015**, 21, 241-259.

20 Wypych, F., Weber, T. & Prins, R. Scanning Tunneling Microscopic Investigation of 1T-MoS_2. *Chem. Mater.* **1998**, 10, 723-727.

21 Mayorga-Martinez, C. C., Ambrosi, A., Eng, A. Y. S., Sofer, Z. & Pumera, M. Metallic 1T-WS_2 for Selective Impedimetric Vapor Sensing. *Adv. Funct. Mater.* **2015**, 25, 5611-5616.

22 Ambrosi, A., Sofer, Z. & Pumera, M. 2H → 1T phase transition and hydrogen evolution activity of MoS_2, $MoSe_2$, WS_2 and WSe_2 strongly depends on the MX_2 composition. *Chem Commun (Camb)* **2015**, 51, 8450-8453.

23 Brewer, L. L., R. H. . Mo–Te Phase Diagram. *ASM Alloy Phase Diagram Database (ASM International, 2006)*.

24 Puotine, D. & Nwenham, R. E. The crystal structure of $MoTe_2$. *Acta Cryst.* **1961**, 14, 691.

25 Dawson, W. G. & Bullett, D. W. Electronic structure and crystallography of $MoTe_2$ and WTe_2. *J. Phys. C: Solid State Phys.* **1987**, 20, 6159-6174.

26 Keum, D. H., Cho, S. *et al.* Bandgap opening in few-layered monoclinic $MoTe_2$. *Nature Phys.* **2015**, 11, 482-486.

27 Jin Cheol Park, Seok Joon Yun *et al.* Phase-Engineered Synthesis of Centimeter-Scale 1T′-and 2H-Molybdenum Ditelluride Thin Films. *ACS Nano* **2015**, 9, 6548-6554.

28 Sankar, R., Narsinga Rao, G. *et al.* Polymorphic Layered $MoTe_2$ from Semiconductor, Topological Insulator, to Weyl Semimetal. *Chemistry of Materials* **2017**, 29, 699-707.

29 Cheng, S., Yang, L. *et al.* Large area, phase-controlled growth of few-layer, two-dimensional $MoTe_2$ and lateral 1T′–2H heterostructures by chemical vapor deposition. *CrystEngComm* **2017**, 19, 1045-1051.

30 Ke Deng, Guoliang Wan *et al.* Experimental observation of topological Fermi arcs in $MoTe_2$. *Nature Phys.* **2016**.

31 Zhou, L., Zubair, A. *et al.* Synthesis of High-Quality Large-Area Homogenous 1T' $MoTe_2$ from Chemical Vapor Deposition. *Adv. Mater.* **2016**.

32 Chen, S. Y., Goldstein, T., Venkataraman, D., Ramasubramaniam, A. & Yan, J. Activation of New Raman Modes by Inversion Symmetry Breaking in Type II Weyl Semimetal Candidate T'-$MoTe_2$. *Nano Lett.* **2016**, 16, 5852-5860.

33 Clarke, R., Marseglia, E. & Hughes, H. P. A low-temperature structural phase transition in β-$MoTe_2$. *Philosophical Magazine Part B* **1978**, 38, 121-126.

34 Zhang, K., Bao, C. *et al.* Raman signatures of inversion symmetry breaking and structural phase transition in type-II Weyl semimetal $MoTe_2$. *Nat. Commun.* **2016**, 7, 13552.

35 Shao-Yu Chen, Thomas Goldstein, Ashwin Ramasubramaniam & Yan, J. Inversion-symmetry-breaking-activated shear Raman bands in T′-$MoTe_2$. **2016**.

36 A. Tamai, Q. S. Wu *et al.* Fermi arcs and their topological character in the candidate type-II Weyl semimetal $MoTe_2$. *Phys. Rev. X* **2016**, 6, 031021.

37 Jiang, J., Liu, Z. K. *et al.* Signature of type-II Weyl semimetal phase in $MoTe_2$. *Nat. Commun.* **2017**, 8, 13973.

38 Brown, B. E. The Crystal Struetures of WTe_2 and High-Temperature $MoTe_2$. *Acta Cryst.* **1965**, 20, 268.

39 Naylor, C. H., Parkin, W. M. *et al.* Large-area synthesis of high-quality monolayer 1T'-WTe_2 flakes. *2D Materials* **2017**, 4, 021008.

40 Lee, J., Ye, F. *et al.* Single- and few-layer WTe_2 and their suspended nanostructures: Raman signatures and nanomechanical resonances. *Nanoscale* **2016**, 8, 7854-7860.

41 Jana, M. K., Singh, A. *et al.* A combined experimental and theoretical study of the structural, electronic and vibrational properties of bulk and few-layer T_d-WTe_2. *J. Phys.: Condens. Matter.* **2015**, 27, 285401.
42 Zhou, Y., Chen, X. *et al.* Pressure-induced T_d to 1T′ structural phase transition in WTe_2. *AIP Advances* **2016**, 6, 075008.
43 Jiang, Y. C., Gao, J. & Wang, L. Raman fingerprint for semi-metal WTe_2 evolving from bulk to monolayer. *Sci. Rep.* **2016**, 6, 19624.
44 Kong, W. D., Wu, S. F. *et al.* Raman scattering investigation of large positive magnetoresistance material WTe_2. *Appl. Phys. Lett.* **2015**, 106, 081906.
45 H., O. W-Te phase diagram. *ASM Alloy Phase Diagram Database (ASM International, 2006)* **1990**.
46 Ali, M. N., Xiong, J. *et al.* Large, non-saturating magnetoresistance in WTe_2. *Nature* **2014**, 514, 205-208.
47 Mar, A., Jobic, S. p. & Ibers, J. A. Metal-metal vs tellurium-tellurium bonding in WTe_2 and its ternary variants $TaIrTe_4$ and $NbIrTe_4$. *J. Am. Chem. Soc.* **1992**, 114, 8963-8971.
48 Lv, Y. Y., Cao, L. *et al.* Composition and temperature-dependent phase transition in miscible $Mo_{1-x}W_xTe_2$ single crystals. *Sci. Rep.* **2017**, 7, 44587.
49 Yan, X.-J., Lv, Y.-Y. *et al.* Composition dependent phase transition and its induced hysteretic effect in the thermal conductivity of $W_xMo_{1-x}Te_2$. *Appl. Phys. Lett.* **2017**, 110, 211904.
50 Oliver, S. M., Beams, R. *et al.* The structural phases and vibrational properties of $Mo_{1-x}W_xTe_2$ alloys. *2D Materials* **2017**, 4, 045008.
51 Lv, Y. Y., Li, X. *et al.* Experimental Observation of Anisotropic Adler-Bell-Jackiw Anomaly in Type-II Weyl Semimetal $WTe_{1.98}$ Crystals at the Quasiclassical Regime. *Phys. Rev. Lett.* **2017**, 118, 096603.
52 Qi, Y., Naumov, P. G. *et al.* Superconductivity in Weyl semimetal candidate $MoTe_2$. *Nat. Commun.* **2016**, 7, 11038.
53 Kang, D., Zhou, Y. *et al.* Superconductivity emerging from a suppressed large magnetoresistant state in tungsten ditelluride. *Nat. Commun.* **2015**, 6, 7804.
54 Drouhin, H.-J., Wegrowe, J.-E., Razeghi, M., Lu, H.-Z. & Shen, S.-Q. Weak localization and weak anti-localization in topological insulators. *SPIE.* **2014**, 9167, 91672E.
55 Wang, L., Gutierrez-Lezama, I. *et al.* Tuning magnetotransport in a compensated semimetal at the atomic scale. *Nat. Commun.* **2015**, 6, 8892.
56 Gong, Y., Lin, J. *et al.* Vertical and in-plane heterostructures from WS_2/MoS_2 monolayers. *Nature Mater.* **2014**, 13, 1135-1142.
57 Schmidt, P., Binnewies, M., Glaum, R. & Schmidt, M. Chemical Vapor Transport Reactions–Methods, Materials, Modeling. **2013**.
58 Ubaldini, A., Jacimovic, J., Ubrig, N. & Giannini, E. Chloride-Driven Chemical Vapor Transport Method for Crystal Growth of Transition Metal Dichalcogenides. *Crystal Growth & Design* **2013**, 13, 4453-4459.
59 Chen, F. C., Luo, X., Xiao, R. C. & Lu, W. J. Superconductivity enhancement in the S-doped Weyl semimetal $MoTe_2$. *Appl. Phys. Lett.* **2016**, 108.
60 Zandt, T., Dwelk, H., Janowitz, C. & Manzke, R. Quadratic temperature dependence up to 50 K of the resistivity of metallic $MoTe_2$. *J. Alloys Compd.* **2007**, 442, 216-218.
61 Takahashi, H., Akiba, T. *et al.* Anticorrelation between polar lattice instability and superconductivity in the Weyl semimetal candidate $MoTe_2$. *Phys. Rev. B* **2017**, 95.
62 Deng, K., Wan, G. *et al.* Experimental observation of topological Fermi arcs in type-II Weyl semimetal $MoTe_2$. *Nature Phys.* **2016**, 12, 1105-1110.

63 Joshi, J., Stone, I. R. *et al.* Phonon anharmonicity in bulk T_d-$MoTe_2$. *Appl. Phys. Lett.* **2016**, 109, 031903.
64 S.W.Hla. STM, AFM investigations of β-$MoTe_2$, α-$MoTe_2$ and WTe_2. *Surface Science* **1996**, 352-354, 105-111.
65 Böker, T., Severin, R. *et al.* Band structure of MoS_2, $MoSe_2$, andα−$MoTe_2$: Angle-resolved photoelectron spectroscopy and ab initio calculations. *Phys. Rev. B* **2001**, 64.
66 F. Y. Bruno, A. Tamai *et al.* Observation of large topologically trivial Fermi arcs in the candidate type-II Weyl semimetal WTe_2. *Phys. Rev. B* **2016**, 94, 121112.
67 Mleczko, M. J., Xu, R. L. *et al.* High Current Density and Low Thermal Conductivity of Atomically Thin Semimetallic WTe_2. *ACS Nano* **2016**, 10, 7507-7514.
68 Chenlu Wang, Yan Zhang *et al.* Spectroscopic Evidence of Type II Weyl Semimetal State in WTe_2. *Phys. Rev. B* **2016**, 94, 241119.
69 Lv, Y. Y., Li, X. *et al.* Experimental Observation of Anisotropic Adler-Bell-Jackiw Anomaly in Type-II Weyl Semimetal $WTe_{1.98}$ Crystals at the Quasiclassical Regime. *Phys. Rev. Lett.* **2017**, 118, 096603.
70 Ilya Belopolski, Su-Yang Xu *et al.* Discovery of a new type of topological Weyl fermion semimetal state in $Mo_xW_{1-x}Te_2$. *Nat. Commun.* **2016**, 7, 13643.
71 Hideaki Sakai, Koji Ikeura & Bahramy, M. S. Critical enhancement of thermopower in a chemically tuned polar semimetal $MoTe_2$. *Sci. Adv.* **2016**, 2.
72 Luo, X., Chen, F. C. *et al.* T_d-$MoTe_2$: A possible topological superconductor. *Appl. Phys. Lett.* **2016**, 109, 102601.
73 F. C. Chen, H. Y. L., X. Luo, W. J. Lu, Q. L. Pei, G. T. Lin, Y. Y. Han, X. B. Zhu, W. H. Song, and Y. P. Sun. Extremely large magnetoresistance in the type-II Weyl semimetal $MoTe_2$. *Phys. Rev. B* **2016**, 94.
74 Suyeon Cho, Sera Kim *et al.* Phase patterning for ohmic homojunction contact in $MoTe_2$. *Science* **2015**, 349, 625-628.
75 Revolinsky, E. & Beerntsen, D. Electrical Properties of the $MoTe_2$−WTe_2 and $MoSe_2$−WSe_2 Systems. *J. Appl. Phys.* **1964**, 35, 2086-2089.
76 D. Rhodes, R. Schönemann *et al.* Disorder-dependent superconductivity, Berry-phase and bulk Fermi-surface of Type-II $MoTe_2$. *Phys. Rev. B* **2017**, 96, 165134.
77 Zhou, Q., Rhodes, D. *et al.* Hall effect within the colossal magnetoresistive semimetallic state of $MoTe_2$. *Phys. Rev. B* **2016**, 94.
78 D. Rhodes, Q. Z., R. Schoenemann, Q. R. Zhang, E. Kampert, Y.-c. Chiu, Y. Lai, Y. Shimura, G. T. McCandless, J. Y. Chan, D. W. Paley, J. Lee, J. P. C. Ruff, S. Das, E. Manousakis, M. D. Johannes, L. Balicas. Impurity dependent superconductivity, Berry phase and bulk Fermi surface of the Weyl type-II semi-metal candidate $MoTe_2$. *Phys. Rev. B* **2017**, 96, 1651334.
79 Huang, L., McCormick, T. M. *et al.* Spectroscopic evidence for a type II Weyl semimetallic state in $MoTe_2$. *Nature Mater.* **2016**, 15, 1155-1160.
80 Feng, B., Yang-Hao Chan *et al.* Spin Texture in Type-II Weyl Semimetal WTe_2. *Phys. Rev. B* **2016**, 94, 195134.
81 https://www.bruker.com.
82 https://commons.wikimedia.org/wiki/File:FluorescenceFilters_2008-09-28.svg.
83 http://bridgepathscientific.com/wordpress/.
84 https://cmm.centre.uq.edu.au/jeol-jsm-7001f.
85 http://nptel.ac.in/courses/102103044/module3/lec18/1.html.
86 Dawson., W. G. & Bullett., D. W. Electronic structure and crystallography of $MoTe_2$ and WTe_2. *J. Phys. C: solids state phys.* **1987**, 20, 6159-6174.
87 Ruppert, C., Aslan, O. B. & Heinz, T. F. Optical properties and band gap of single- and few-layer $MoTe_2$ crystals. *Nano Lett.* **2014**, 14, 6231-6236.

88 Puurunen, R. L. & Vandervorst, W. Island growth as a growth mode in atomic layer deposition: A phenomenological model. *J. Appl. Phys.* **2004**, 96, 7686-7695.
89 Clarke, R., Marseglia, E. & Hughes, H. P. A low-temperature structural phase transition in β-$MoTe_2$. *Philos. Mag. B* **1978**, 38, 121-126.
90 Morales-Estrella., R., Arvanitidies., I. & Seetharaman., S. Intrinsic Reduction Kinetics of MoO_3 by Hydrogen. *Z. Metallkd* **2000**, 91, 589-593.